White matter microstructure estimation and visualization in neuropathological brains via diffusion MRI

DELINTE Nicolas

Thesis submitted in partial fulfillment of the requirements for the degree of
'Docteur en sciences de l'ingénieur et technologie'

Ph.D. Jury

Promotors:	MACQ Benoit
	DRICOT Laurence
Supervisors:	DE TIMARY Philippe
	RENSONNET Gaëtan
Jury president:	LEFEVRE Philippe
External jury:	THIRAN Jean-Philippe
	MENEGAZ Gloria

ICTEAM - IoNS
UCLouvain
Belgium
2024

"*As for my own part, it is my opinion that the true method of dissection would be to trace the nervous filaments through the substance of the brain, to see which way they pass, and where they end; but this method is accompanied with so many difficulties, that I know not whether we may hope ever to see it executed without a particular manner of preparing.*"

-Niels Steensen, 1665

Abstract

The brain, with its intricate network of neural cells, their connections, and associated functions, forms a complex structure that has long fascinated researchers. Recent advances in MRI technology, particularly diffusion MRI, have enabled the in vivo investigation of connections between brain regions and the microstructure of the neural fibers linking those regions. However, these advancements and the methodologies they enabled could benefit from further improvements. On the macroscopic scale, identifying these connections relies on tractography algorithms that require either pre-defined atlases or extensive manual corrections and expertise to delineate accurately. On the microscopic scale, advancements in microstructural models have enabled more precise estimations of the direction and properties of each fiber bundle within a voxel. However, the increasing number and complexity of these models have delayed their adoption in medical research.

During this thesis, tools were developed to ease the generation and cleaning of tractography outputs and to facilitate the comparison and interpretation of models estimating multiple fiber populations per voxel. These tools included a modification to the tractography algorithm, a method for filtering spurious streamlines, and a framework attributing multi-fixel metrics to specific tracts. These methods were validated using synthetic phantoms, in vivo scans, and population studies. These studies examined differences in the language pathways of dyslexic children, the effects of abstinence in alcohol-dependent participants and the impact of intense motor training on participants with impaired motor control due to cerebral palsy and stroke.

The modified tractography algorithm produced fewer spurious streamlines compared to classic algorithms. The filtering process was efficient and preserved tract morphology, while its byproducts enabled along-tract analyses. The proposed framework provided comparative analyses with existing approaches, demonstrated high flexibility in its inputs, and introduced a new approach showing increased accuracy. Furthermore, the tools developed are independent of specific methodologies or algorithms, and all code has been made open-source to enhance usability. Overall, these tools could benefit researchers analyzing specific white matter tracts, especially in non-conventional brains.

Contents

List of Figures

Acronyms

AD	Axial diffusivity
AF	Arcuate fasciculus
AFD	Apparent fiber density
AUD	Alcohol use disorder
ang	angular weighting
CC	Corpus callosum
CFE	Connectivity-based fixel enhancement
cfo	closest-fixel-only
CP	Cerebral palsy
CSD	Constrained spherical deconvolution
CSF	Cerebrospinal fluid
CST	Corticospinal tract
DMD	DIAMOND
dMRI	Diffusion MRI
dODF	Diffusion orientation distribution function
DTI	Diffusion tensor imaging
FA	Fractional anisotropy
FAT	Frontal aslant tract
FBA	Fixel based analysis
fixel	Fiber population within a voxel
fMRI	Functional MRI
FOD, fODF	Fiber orientation distribution function
FVF	Fiber volume fraction
GM	Gray matter

MD	Mean diffusivity
MF	Microstructure fingerprinting
MRI	Magnetic resonance imaging
MSMT-CSD	Multi-shell multi-tissue CSD
MTM	Multi-tensor model
ODF	Orientation distribution function
pdf	probability density function
PGSE	Pulse gradient spin echo
pmf	probability mass function
RD	Radial diffusivity
RF	Radio frequency
ROI	Region of interest
roi	region of interest weighting
SD	Spherical deconvolution
SH	Spherical harmonics
SLF	Superior longitudinal fasciculus
SNR	Signal-to-noise ratio
TE	Echo time
TR	Repetition time
tsl	total segment length weighting
UF	Uncinate fasciculus
VBA	Voxel bases analysis
vol	relative volume weighting
WM	White matter
WMQL	White matter query language

List of symbols

Symbol	Definition	Units
B_0	main external magnetic field	T
B_1	RF coil magnetic field	T
b	b-value	s/mm^2
E	diffusion MRI signal attenuation	
D	diffusivity	mm^2/s
$\mathbf{d}$	direction	
Δ	separation between gradient pulses	s
δ	duration of gradient pulse	s
G	magnitude of a gradient pulse	T/m
γ	gyromagnetic ratio	$rad/s \cdot T$
K	number of fixels	
M	net magnetization	T
λ	eigenvalue	
f	volume fraction	
S	dMRI signal	
S_0	dMRI signal at b=0	
$T1$	spin-lattice relaxation time constant	s
$T2$	spin-spin relaxation time constant	s
$\mathcal{A}$	set	
$\mathbf{M}$	matrix	
$\overrightarrow{r}$	ray	
$\mathbf{v}$	vector	
$\hat{\mathbf{v}}$	$= \mathbf{v}/\lvert\mathbf{v}\rvert$, unit vector	

Introduction

The brain is a complex structure, from its role as the residence of our thoughts, to its structure and the organization of its interweaving neural cells. Each brain area fulfills a distinct role in our day to day lives, and each of these areas is interconnected through a network comprised of millions of intertwining neurons, often referred to as white matter. These neurons transmit information through electrical impulses along the axons, i.e., projections of the neurons conducting the action potentials away from the cell body. This perpetual transmission of concurring signals is supported by a network of blood vessels providing essential nutrients and oxygen, along with glial cells that maintain homeostasis and provide support for the neurons. The architecture of the brain, encompassing all these cohesive elements, has long been an area of interest. Recent advances in magnetic resonance imaging (MRI) technology have enabled the in vivo investigation of both the microscopic and macroscopic organization of the white matter and its complex network of neural fibers. This is achieved through diffusion MRI, a category of MRI leveraging the diffusion patterns of water molecules present in the brain to gain information about its internal structures.

Although the reconstruction of the macroscopic neural pathways, a process known as tractography, has enabled the visualization of connections between brain regions in vivo and is now a standard practice in guiding neurosurgery, the resulting streamlines are heavily influenced by the parameters employed in the algorithms. Fine-tuning these parameters requires expert knowledge in brain anatomy and often requires adjustments depending on the region of interest, making the automation of this process challenging. The commonly used solutions are to manually adjust the parameters and visually inspect the appearance of the tract, a process that can be quite time consuming, or to use atlas-based algorithms.

Furthermore, while the emergence of advanced diffusion models capable of discerning multiple fiber populations in a voxel, referred to as multi-fixel models, have increased the accuracy of the estimated direction and microstructure of the neural fibers, they are more difficult to interpret and are not commonly used in clinical practice. This increased precision is accompanied by longer computation times, a greater number of parameters to adjust, and more complex outputs. The variety of available models has also complicated the selection of a successor to DTI, one of the earliest diffusion models. Despite being introduced in 1994 and having known limitations, DTI remains the most commonly used model in both clinical and research settings.

The aforementioned limitations are further exacerbated in cases involving highly deformed brains. Since most of the state-of-the-art research is being

developed using long diffusion acquisitions with healthy controls, many automated processes do not function as intended when applied to brains deviating from the average brain structure due to lesions. This is primarily due to most algorithms not being validated on highly deformed brains. This challenge extends to many emerging AI tools, which are often not trained on highly irregular data. Furthermore, while longer dMRI sequences have the potential to acquire more information and reduce noise in the diffusion signal, patients with neuropathologies often struggle to stay for extended periods of time in a MRI scanner. There is thus a delicate balance between the time a patient can stay in the scanner, and the length of the diffusion MRI sequence.
Additionally, analyzing patient-specific regions of interest, commonly facilitated by automated atlases, can become arduous when the region of interest is not represented in the atlas, such as regions isolated via functional MRI. Overall, patient-specific analyses, especially with neuropathological brains, significantly increase the time required for many steps of the classical analysis pipelines.

The overarching objective of this thesis was to elaborate tools capable of facilitating the analysis of white matter tract in neuropathological brains. To achieve this goal, tools were developed to simplify tract extraction, ensuring the generation of clean tracts, and to provide flexible multi-fixel analyses tailored for patient-specific studies in brains exhibiting significant deformations.
Generating streamlines connecting regions across the brain and navigating through its different structures, such as the ventricles and the cortical folds, requires high angles of curvature. However, enabling these high angles in the streamline generation process creates a lot of biologically implausible neural pathways. To remedy this issue, we propose a simple modification of the classic tractography algorithm to enable a variable maximum angle between tractography steps to allow specific brain regions to benefit from a higher maximum angle.
Another way to mitigate the appearance of these spurious streamlines is to intervene after the creation of the tracts and to filter out spurious streamlines. To demonstrate this approach, we propose a filtering algorithm based on density estimates along the tract trajectory, which can be leveraged for along-tract analysis.
Once the tracts are obtained and cleaned either with classical means or the proposed approaches, they can be integrated with multi-fixel microstructural outputs to estimate the tract-specific microstructural properties of brain connections along their pathway. To achieve this task, we introduce a framework for attributing microstructural properties to neural tracts, thereby simplifying the analysis of these properties along tracts of interest.

A central theme throughout this thesis was the emphasis on visualizing the various steps within the pipeline. This approach ensures that results and analyses were visualized, facilitating the detection of edge cases where the behavior did not fit the intended results.

This thesis will begin with a brief overview of the fundamental concepts involved in diffusion MRI and the notions upon which the developments made in this thesis are built. Afterwards, the methodology developed will be described through three key contributions: a modification of tractography algorithms to account for the morphology of white matter adjacent to the cortex, an automated streamline algorithm for tract clean-up, and the combination of these tracts with multi-fixel models to characterize the microstructure of macroscopic brain pathways. These techniques will then be applied to cohorts of participants afflicted with neurological pathologies significantly impacting brain morphology, including stroke, cerebral palsy, and alcohol use disorder.

Background

"*There is no scientific study more vital to man than the study of his own brain. Our entire view of the universe depends on it.*"

-Francis Crick, 1979

A wide variety of approaches have been employed in the pursuit of exploring and understanding the inner workings of the brain, from the first autopsy practices to modern imaging technologies. Before delving into the topic of this thesis, let us remind ourselves of how we got here. This section covers the main background and foundational concepts on which the developments made in this thesis are based on, from the beginnings of magnetic resonance imaging (MRI) to the more recent models and techniques.

The development of MRI as we know it today started about a century ago and relied on the works of many individuals. In the 1930s, I.I. Rabi, which is credited for the discovery of nuclear magnetic resonance (NMR), developed a new way to measure the magnetic properties of nuclei. In his experiments, he noted that "*If a small oscillating magnetic field is applied at right angles to a much larger constant field, a re-orientation of the nuclear spin and magnetic moment with respect to the constant field will occur when the frequency of the oscillating field is close to the Larmor frequency of precession of the particular angular momentum vector in question.*" [1]. This observation will be at the core of the further developments that led to MRI. These experiments employed the concept of the Larmor frequency

$$\omega_0 = \gamma B_0, \tag{1}$$

where γ is the gyromagnetic ratio of a nuclei and B_0 the external magnetic field. The speed at which the net magnetization returns to its initial maximum value M_0 is linked to the spin-lattice relaxation time constant $T1$.

During the 1940s, F. Bloch and E. Purcell independently conducted experiments to further describe the NMR phenomenon in solids and liquids. Bloch derived formulas, known as the Bloch equations, describing the effects the precession and relaxation after an RF pulse on the net magnetization [2]. These equations are explained in more detail in Appendix A.1. Despite being targeted towards physical applications (not physiology, medicine, or biology) their research laid the groundwork for the development of MRI scanners capable of using the intrinsic water content within the body to create magnetic resonance images. It is not until the 1950s, with G. Lindström and E. Odeblad, that NMR was considered to study biological tissues. In an article where they studied different biological samples, they theorized that the differences in water and biological tissue response were due to distinct tissues absorbing and organizing water molecules differently. [3]
In the same years, E. Hahn discovered an echo after two 90° radio frequency (RF) pulses (see Appendix A.2 for more information about RF pulses). The amplitude of this signal decreased with the echo time (TE), i.e., the time between

the excitation pulse and the peak of the signal

$$S_0 \propto M_0 e^{-TE/T2}, \tag{2}$$

where T2 is the time constant for spin–spin relaxation, specific to each tissue type. This development will be known as the spin echo sequence.

In the 1970s, R. Damadian proposed that NMR could be leveraged to provide a non-invasive way of detecting cancers [4]. He then built the first full-body machine and produced the first full magnetic resonance imaging (MRI) scan.

Since its inception, MRI has garnered significant attention across various scientific and medical domains due to its capabilities in diagnostic medicine and biomedical research. Initially employed for anatomical imaging, MRI has evolved to encompass a spectrum of sub-modalities aimed at exploring diverse aspects of cerebral function. These include functional MRI (fMRI) and diffusion MRI (dMRI), which can respectively capture cerebral blood flow patterns and neuronal pathways within the nervous system.

Diffusion MRI

In a cube filled with water, the water molecules are free to move in every direction, a process known as *free diffusion* or Brownian motion (Fig. 1A). The presence of obstacles or structure, such as cellular membranes, inside the cube will hinder the movement of the water molecules, which will then be categorized as *restricted diffusion* (Fig. 1B). The main challenge of diffusion MRI is to decipher the information contained in the movement of those water molecules to characterize the brain's structure. By orienting magnetic fields along different directions, the diffusivity of water molecules along those directions can be quantified. This diffusivity is directly impacted by the structure inside each volume of the image reconstructed from the diffusion data, i.e., *voxel*.

In 1965, E.O. Stejskal and J.E. Tanner derived the equation that will be the basis for dMRI and introduced pulsed gradients into the spin echo sequence [5]. The addition of pulsed gradients in the spin echo sequence, schematically represented in Fig.2, gave the name pulse gradient spin echo (PGSE) sequence. Stejskal and Tanner also proposed the idea of measuring restricted diffusion of water molecules by varying the delay Δ between the gradient pulses. The Stejskal-Tanner formula, describing the attenuation of the signal

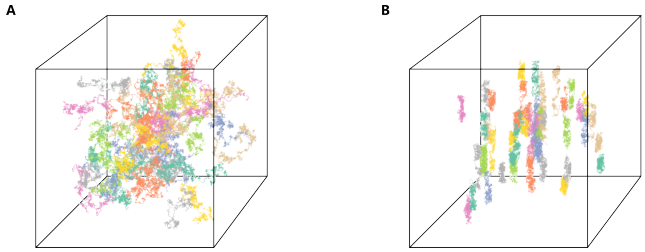

Figure 1: Representation of the movement of water molecules in a voxel with **A** free diffusion and **B** restricted diffusion. Each color represents the trajectory of a single molecule.

response of the echo S_0 presented in Eq. (2), is written as

$$S = S_0 e^{-(\gamma G \delta)^2 (\Delta - \delta/3) D}, \tag{3}$$

where the parameter D represents the *apparent diffusion coefficient* along a direction. The other parameters are the magnitude G and duration δ of the gradient pulses, separated by a time interval Δ, and γ the gyromagnetic ratio of the proton H^+, introduced in Eq. (1). Protons are used due to their magnetic moment and abundance in the human body, primarily in the form of water molecules.

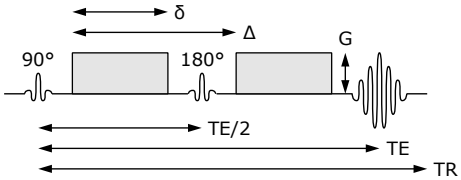

Figure 2: Simplified representation of the main parameters of a Pulse Gradient Spin Echo (PGSE) sequence. The two RF pulses generate a flip of 90° and 180°. TR is the duration between repeated RF pulse sequences. Pulse gradients are represented in grey.

Several parameters characterizing the magnetic field intensity are commonly grouped into a single value, called the *b-value*, expressed in s/mm^2.

$$b = (\gamma G \delta)^2 (\Delta - \delta/3), \tag{4}$$

The diffusivity specific to a direction can be obtained by employing encoding gradients along said direction. Water molecules diffusing in a certain direction between the application of the two gradients, will not be correctly rephased by the second gradient and the intensity of the echo obtained will

be reduced. By taking multiple orientations into account and incorporating Eq. (4), Eq. (3) can be rewritten as

$$S = S_o e^{-b\hat{\mathbf{g}}^T \mathbf{D}\hat{\mathbf{g}}}, \tag{5}$$

with S_0 the signal response of the echo without pulsed gradients and S the response signal along the direction $\hat{\mathbf{g}}$. The direction of the pulsed gradient is referred to as *b-vector*

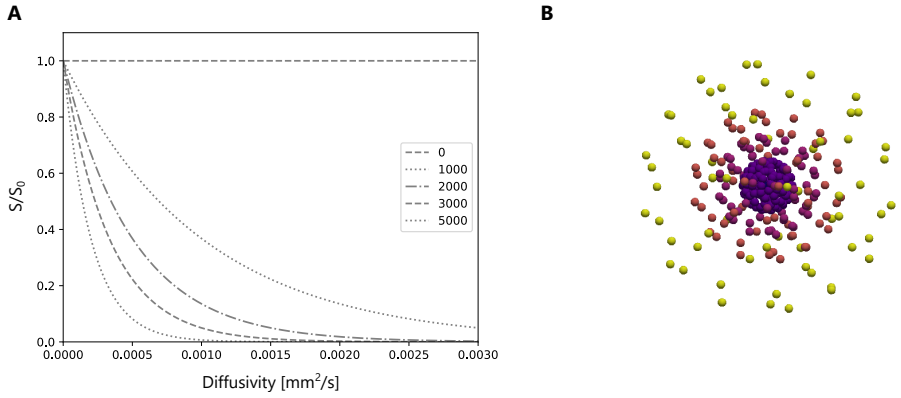

Figure 3: Representation of **A** the attenuation of diffusion signal depending on the tissue diffusivity at different b-values (b=0,1000,2000,3000,5000). **B** Representation of the directions (b-vectors) in a multi-shell sequence with the same b-values. Each b-value is represented with a different color and radius.

The representation of Eq. (5) for different b-values in Fig. 3A demonstrates that the two factors leading to a decreased echo signal are an increased diffusivity along a specific direction and a higher b-value. By varying the magnetic field intensity, differences in diffusivity between tissues can be highlighted. As seen in Fig. 4, averaging the signal over multiple directions highlight different tissue types depending on the gradient intensity: high b-values can help differentiate regions of low diffusivity, such as areas with densely packed neural fibers and low b-values help differentiate regions of high diffusivity such as the cerebrospinal fluid (CSF). The ideal b-value to observe a specific tissue is often considered to be

$$b_{opt} = 1/D_{tissue},$$

which corresponds to the b-value with the highest slope for a specific diffusivity. For more information on this topic, see Appendix A.3.

Figure 4: 2D slice of the third quartile values of different shells with **A** b=0, **B** b=1000, **C** b=2000, **D** b=3000 and **E** b=5000. The intensity was normalized between 0 and 1 for each shell to mitigate the effect of decreasing signal strength at high b-values.

To leverage the sensitivity of b-values to different tissue diffusivities, multiple gradient values can be acquired within a single sequence, known as a multi-shell sequence (see Fig. 3B). Due to their higher angular resolution, shells with a high b-value require a higher number of directions to be investigated. The main acquisition strategy to resolve multiple fiber orientations in areas of crossing fibers is High angular resolution diffusion imaging (HARDI), which samples the orientation space as densely and uniformly as is practical to separate out the contributions of each fiber populations [6].

Microscopic orientation & structure

To decode the signal received from the scanner and translate it into useful information about the structural properties of a voxel, two main approaches have been developed: model-free techniques reconstructing the diffusion ODF (dODF) [6] and model-based techniques reconstructing the fiber ODF (fODF).

Techniques reconstructing the dODF are often grouped under the name Q-space imaging (QSI), an umbrella term for methods measuring the microscopic diffusion function without any assumptions on the form of the underlying diffusion function [7]. QSI uses the Fourier relation between the diffusion signal and the spin propagator to measure the diffusion function by sampling the diffusion signal on a three-dimensional Cartesian lattice. The peaks in the dODF can be interpreted as the main fiber orientations of a voxel, since these correspond to the directions of highest spin displacement. The drawbacks of these methods are the long scan time requirements and the pulsed field gradients required to fully characterize the spin propagator. In the early 2000s, D.S. Tuch introduced diffusion spectrum imaging (DSI, a variant form of QSI) and q-ball imaging (QBI) [8]. QBI is a model-free approach using the HARDI protocol and the Funk–Radon transform, capable of resolving in-

travoxel white matter fiber architecture. Other techniques have since been built upon this approach such as constant solid angle (CSA), which, by considering the solid angle factor, results in a sharper and normalized dODF expression [9].
More recently, methods decomposing the diffusion signal into a series expansion of basis functions have emerged, such as 3D-SHORE and MAP-MRI [10].

On the other hand are model-based approaches. Since its introduction in 1994 by P.J. Basser, diffusion tensor imaging (DTI) [11] has remained the most common fODF algorithm to inspect the main orientation of voxels in vivo. DTI makes the assumption that the diffusion of water molecules in each voxel can be approximated by a Gaussian distribution and consequently models the diffusion coefficient **D** as a diffusion tensor, defined by its three eigenvectors. The anisotropy of the diffusion in white matter voxels is represented by an ellipsoid aligned with the main orientation of diffusion. The amplitude of the eigenvectors gives information about the diffusion properties associated to a direction. See Appendix A.4 for more information about the formulation of the diffusion tensor and its metrics.
The method is however based on hypotheses, and the more we deviate from these hypotheses, the less DTI can adequately inform us on the structure inside the voxels, as the parameters estimated can only accurately represent the microstructure if the hypothesis of the model are respected.
The first hypothesis is that the diffusion signal can be represented by a Gaussian process. DTI is thus no longer correct when we deviate from the Gaussian fit of the response signal, which renders high b-values unusable for the DTI fit. To account for the non-Gaussian behavior of biological tissue, diffusion tensor imaging (DTI) was extended in a model called diffusion kurtosis imaging (DKI) [12]. This model provides, in addition to the diffusion coefficient, an estimate of the excess kurtosis of the diffusion displacement probability distribution, representing the departure from the Gaussian process.
The second hypothesis is that a single diffusion tensor can approximate the diffusion signal. This hypothesis renders DTI unable to discern multiple fiber orientations inside a single voxel, as the signal arising from multiple fixels will be merged together. DTI is thus limited in regions of crossing fibers, which represent 70% to 90% of all voxels in the brain [13]. Theoretically, by increasing the resolution, the number of voxels with crossing fibers can be reduced, but this increases scan time.
This limitation is extended to the partial volume effects caused by the presence of other tissue types, such as CSF, within a voxel. To address these partial volume effects, models started including multiple compartments.

Multi-compartment models

Multi-compartment models consider that the response signal is the sum of the signals of different compartments, each with its own response type. To include multiple compartments into the response signal, the equation for the received signal can be rewritten as

$$S = \sum_{i}^{C} f_i S_i, \quad \text{with} \quad \sum_{i}^{C} f_i = 1. \tag{6}$$

with C the number of compartments, f_i the volume fraction of the signal attributed to each compartment and S_i the signal of each compartment approximated with a model, as in Eq. (5).

To improve the fit of DTI in regions in areas with partial volumes effects, such as the fornix or other areas along the ventricles, DTI can be modified to account for a second isotropic tensor with a fixed diffusivity, set to the diffusivity of free water [14]. Equation (6) becomes

$$S = (1 - f_{iso}) S_0 e^{-b\hat{\mathbf{g}}^T \mathbf{D}\hat{\mathbf{g}}} + f_{iso} S_0 e^{-b D_{iso}},$$

where f_{iso} the volume fraction of the isotropic compartment, with a constant diffusivity D_{iso} across all directions.

Another notable example is NODDI [15], which considers three compartments, each with its own volume fraction: an intra-cellular compartment representing neural fibers as a Watson distribution of sticks, an extra-cellular compartment which is depicted as an anisotropic Gaussian diffusion tensor and an isotropic compartment, with an isotropic Gaussian diffusion tensor.

Multi-fixel models

While models such as NODDI can represent the dispersion of the orientation of the neural fibers, these models are still limited to a single main orientation. Other multi-compartments approaches have been developed to account for multiple orientations in a voxel. These approaches will be referred to as multi-fixel, short for multiple fiber populations in a voxel. By allowing multiple fiber population per voxel to contribute to the signal, each with its own main diffusion orientation, they overcome the limitation observed with DTI in regions of crossing fibers.
The simplest types of multi-fixel models are dual- or multi-tensor models (MTM) [16]. These models extend the tensor model by allowing multiple diffusion tensors within each voxel. For these models, Equation (6) can be rewritten as

$$S = S_0 \sum_k^K f_k e^{-b\hat{\mathbf{g}}^T \mathbf{D}_k \hat{\mathbf{g}}},$$

with K the number of compartments and f_k their corresponding volume fraction. Similarly to the single-fixel models, additional compartments can be added to the multi-fixel models, to account for other partial volume effects, such as an isotropic compartment

$$S = S_0 \left(\sum_k^K f_k e^{-b\hat{\mathbf{g}}^T D_k \hat{\mathbf{g}}} + f_{iso} e^{-b D_{iso}} + ... \right).$$

with the number of compartments being equal to or greater than the number of fixels ($K \leq C$).

A multitude of multi-fixel models have been developed over the years, each designed for specific use cases, with distinct hypotheses and limitations. The ball-and-sticks model can be viewed as a special case of MTM, where the fixels, i.e., *sticks*, are represented as Gaussian tensors with no radial diffusivity and the *ball* is an isotropic Gaussian [17]. It mainly aims at resolving crossing fibers and estimating their relative volume fractions.
The CHARMED model can use any combination of restricted or hindered compartments, respectively estimated with the diffusivity in thin cylinders, with a fixed distribution of axon diameters, and anisotropic Gaussian diffusion tensors [18]. The main orientation and volume fractions of each compartment are also estimated. The AxCaliber model extends the CHARMED model to account for the heterogeneity of axon diameters [19].
DIAMOND [20] expands on MTM models by including heterogeneity into each compartment. The compartments are modeled by a finite sum of unimodal continuous distributions of diffusion tensors. The matrix $\mathbf{D}$ is thus replaced by a matrix-variate Gamma distribution over matrices $\mathbf{D}$ with a mean $\mathbf{D_0}$. By combining elements of the continuous and discrete representations, i.e., modeling the fODF as a discrete set of fiber populations each with its own amount of dispersion, models such as DIAMOND are approaching the characteristics of a continuous fODF.

The previous models can be described as analytical models since changes in diffusivity can only be expressed as a mathematical function with certain assumptions. Another angle of approach is to simulate the diffusion of water molecules in various environments and then match these simulations to the diffusion signal received. An example is Microstructure Fingerprinting (MF) [21], which uses dictionary matching of pre-computed Monte Carlo simulations with different configurations to identify the parameters that best de-

scribe the underlying microstructure in each voxel. In the dictionary, the structure within the voxels is represented by cylinders aligned with the main diffusion direction. The selected diffusion fingerprints provide an estimation of the microstructural parameters for each fascicle of axons present in a voxel.

While multi-fixel models can more accurately describe the organization of white matter fibers, particularly in areas of crossing fibers, they also introduce increased complexity when interpreting the results. Since each fixel has its own microstructure, correspondence issues between voxels and the increased number of outputs can make the process of producing maps for clinical applications more complex. One possibility is to produce mean maps of fiber properties per voxel. Or, if used in combination with tractography, to follow these metrics along the tract of interest, which will be investigated in Chapter 3.

Spherical deconvolution

Most of the previous models provide a "discrete" amount of fiber populations, typically two or three for most MTM models, as increasing the number of fixels above this number tends to decrease their performance. However, other models can provide a "continuous" representation of the fiber orientation information, without restricting the number of fixel per voxel. The primary type of approach is based on the deconvolution of the diffusion signal into spherical harmonics (see Appendix A.5 for more information), a method known as spherical convolution (SD). The initial SD implementation for dMRI was proposed by Tournier & al. in 2004, the algorithm expresses the signal measured as the convolution over spherical coordinates of the *response function* with the fODF [22]. The response function is an essential part of this algorithm and describes the signal intensity that would be measured as a function of orientation for a single fiber population. In the algorithm proposed by Tournier et al., the response function is determined using a subset of voxel presenting a high FA, hopefully representing white matter areas where there are no crossings. Other approaches have employed spherical deconvolution with alternative response functions, such as the FORECAST model, which utilizes diffusion tensors, similar to those in DTI, as response functions [23]. Additionally, blind methods have been developed to estimate the peaks of the fODF without any explicit response function [24]. More information on the response functions can be found in Appendix A.6. In 2007, the authors of the original SD paper introduced constrained SD (CSD). As the name implies, they added a non-negativity constraint to reduce the impact of noise and increase the angular resolution [25]. Further improvements were made to CSD to make full use of multi-shell information, such as multi-shell multi-tissue

CSD (MSMT-CSD) [26], which uses three types of response function, one for the CSF, one for the grey matter and one for the white matter. While the WM response function is still modelled with series of SH coefficients, the GW and CSF are modelled using an SH series of order 0. MSMT-CSD thus entails the estimation of multiple response functions as response functions are required both as a function of b-value and per-tissue type. Originally, the per-tissue response functions were determined using a four-tissue segmentation of a structural image and applying volume fraction and FA thresholds to select reference voxels, but can now also be determined using the segmented dMRI data.
Other attempts have been made to generalize the multi-tissue spherical deconvolution into an unsupervised blind source separation problem, which does not enforce the response function to be known a priori [27].

The SD-based approaches mentioned focus more on discerning the orientation of fibers within a voxel and less on the microstructural properties of these fibers. However, beyond orientation, the amplitude of the signal response obtained from the peaks estimated can offer an indirect measure of the microstructural characteristics associated with those peaks. The hindrance modulated orientational anisotropy (HMOA) [28] and the apparent fiber density (AFD) use the amplitude of each fODF lobe, found by methods such as CSD, as a quantitative measure of neural density [29]. This definition of AFD is susceptible to minor changes in the spread of the fODF, as even minor increases in dispersion can dramatically reduce the amplitude of the peak. To increase the robustness of the estimated fiber density, the AFD can also be computed by integrating the fODF over the solid angle corresponding to each fODF lobe. A recurring theme in dMRI metrics is that they are sensitive, but not specific. AFD acknowledges this limitation by encompassing various biological changes under a single umbrella term. AFD is thus sensitive to the intra-axonal volume fraction of the underlying fiber populations, which can be due to partial volume effects, fiber packing or overall density.

Other approaches have leveraged spherical deconvolution, such as [30], which used it speed up multi-diffusion-tensor fitting.

Macroscopic orientation

The aforementioned algorithms retrieving the fODF can be used to visualize the potential pathways of neural fibers and their connections between various brain regions, a technique known as *tractography*.

Conceptually, tractography algorithms piece together the microstructural orientational information collected in each voxel to generate streamlines representing the course of a bundle of axons across multiple white matter voxels (Fig. 5). A whole-brain tractogram is displayed in Fig. 5. Starting points, i.e., *seeds*, are placed at specified locations or throughout the white matter. For each seed, a pathway called *streamline* is then constructed by taking a *step* of fixed size in the main direction of the voxel. This pathway can be constrained by the placement of anatomical regions, known as exclusion or inclusion regions, which respectively remove streamlines that do or do not pass through them. In addition to the seeded region and inclusion or exclusion zones, the main parameters influencing the overall appearance of the tractogram are the step size, the maximum angle between two steps and the termination condition.
These parameters are usually fixed values requiring extensive fine-tuning. A modified version of the tracking algorithms, investigating the impact of position-dependent parameters, will be described in Chapter 1.

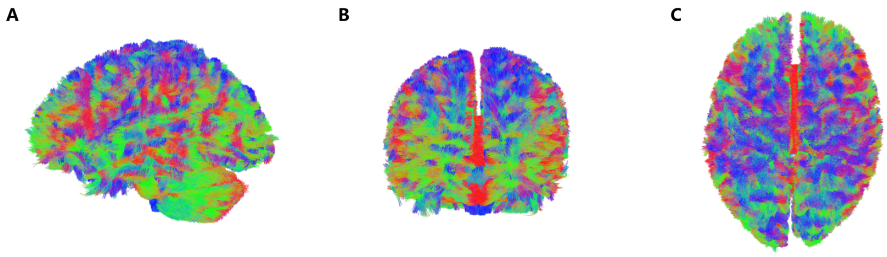

Figure 5: Whole brain tractogram obtained with a probabilistic tractography algorithm in **A** sagittal, **B** coronal and **C** axial view. The color are assigned based on the segment direction: left-right (red), anterior-posterior (green) or inferior-superior (blue).

Similarly to the microscopic orientations, tractography can account for either the main voxel direction or multiple possible directions for each step, it is then called deterministic or probabilistic tractography, respectively.

Deterministic tractography is a set of methods where the local tract direction is defined only by the main diffusion direction in each voxel. The first implementations appeared shortly after the DTI model and could infer macroscopic connectivity between regions by following the principal eigendirection of the estimated diffusion tensor in each voxel [31]. The streamlines are often smoothed using B-spline functions to approximate the noisy trajec-

tory. The termination conditions often include: reaching the boundary of the imaging volume, reaching a region with low diffusion anisotropy, the angle between two steps being higher than the specified angular threshold, and the most collinear eigenvector not being associated with the largest eigenvalue. Not all deterministic methods are limited to a single orientation per voxel. The SD-STREAM algorithm takes as input the fODF image obtained with CSD and, at each step, locates the orientation of the nearest fODF amplitude peak, enabling it to sample multiple orientations while remaining deterministic. Nonetheless, most deterministic tractography algorithms suffer from the same limitations: the inability to follow less-dominant tracts in crossing and fanning fibers regions, early termination of streamline in regions of low FA if the cutoff is set to a FA threshold and no tracking in regions of low anisotropy, such as the interface between white and grey matter.

Probabilistic tractography bypasses these limitations by locally estimating a probability density function (*pdf*), or probability mass function (*pmf*) when the tracking directions are restricted to a discrete number of points on a sphere, in each voxel, corresponding to the main fiber orientations and the respective uncertainty associated to each peak. At each tractography step, a random sample is selected from the *pdf* with the probability of selecting a particular direction being proportional to the amplitude of the fODF along that direction, and a new point is generated. This process continues until the stopping criterion is met [17]. Thereby incorporating the uncertainty in local fiber direction into the streamline generation process. The random sampling in the *pdf* results in varying output between repeated tractographies. While probabilistic tractography overcomes many of the limitations inherent to deterministic tractography, it has the downside of generating a higher number of false positive streamlines due to the increased number of possible directions.
Over the years, numerous variations of the classic probabilistic algorithm have been introduced. A notable example is the iFOD2 algorithm [32], which is based on 2nd order integration over fiber orientation distributions. Rather than sampling from the local fODF only, the probability of each path is computed as the product of the probabilities of each step making up that path. This reduces the overshoot in tracts of high curvature and increases the continuity in crossing fascicles.

Post-tractography algorithms

Once a set of streamlines is obtained, further post processing can be applied on those streamlines depending on their intended research purpose.

Quantitative filtering

If the quantity of connections between regions is of interest, then quantitative filtering is recommended. Tractography is first and foremost a visual representation of the likely pathways between brain regions. This representation has several biases based on the type of tractography used and the parameters selected. Algorithms can help mitigate those biases to allow for the number of streamlines between two regions to be a more accurate measure of the quantity of neural fibers connecting those regions.
Notable examples are SIFT [33] and SIFT2 [34]. SIFT filters out streamlines from the tractogram to improve the fit of the fiber density between the streamline reconstruction and the spherical deconvolution of the diffusion signal, thereby improving the biological accuracy of structural connectivity estimates. SIFT2 further improves this process by replacing the removal of streamlines with the attribution of weights to each streamline. Both of these methods need to be applied on whole brain tractograms.
Other algorithms providing quantitative filtering include COMMIT [35] and COMMIT2 [36]. Both procedures consist of a whole-brain optimization process combining tractography with microstructural features to enhance the robustness of connectivity estimates. COMMIT2 adds anatomical priors to this process to reduce the number of erroneous streamlines.

Tract isolation

If the connections and properties of specific tracts are the focus of the study, then the individual connections can be isolated from a whole brain tractogram either by manually adding inclusion or exclusion regions, or by using tools such as the white matter query language WMQL [37]. WMQL uses a labeled atlas to define tracts of interest in a more human-readable manner using regions of inclusion and exclusion defined by their anatomical names, but also using spatial keywords such as posterior, anterior, left, right, inferior, and superior.

Tract clean up

When the streamlines of interest have been extracted, stray streamlines can often appear, requiring the use of additional exclusion or inclusion zone in

the extraction process. This iterative process can be time-consuming and requires expert knowledge to ensure accuracy. Fortunately, there are methods available to eliminate stray streamlines without necessitating the definition of additional inclusion or exclusion zones. The existing processes allowing for an automated clean up, as well as a new algorithm, will be further explained in Chapter 2.

An overview of this thesis' context

Overall, the models presented in the previous sections, whether mathematical or biophysical, are all based on fixed hypotheses and were developed to describe the orientation or microstructure of specific tissue types. The selection of a model must take into account the microstructural properties to be observed, the acquisition protocol, and the limitations of each model [38, 39, 40].

This thesis builds upon this environment and aims to address some of the limitations in the applicability of the aforementioned micro- and macrostructural models (Part I). The main focus will be on white matter models with multiple orientations to account for crossing fibers. And the combinations of these microstructural models with macrostructural information, to study populations with neuropathological brains (Part II). An overview of the fields adjacent to this thesis is schematically represented in Fig. 6.

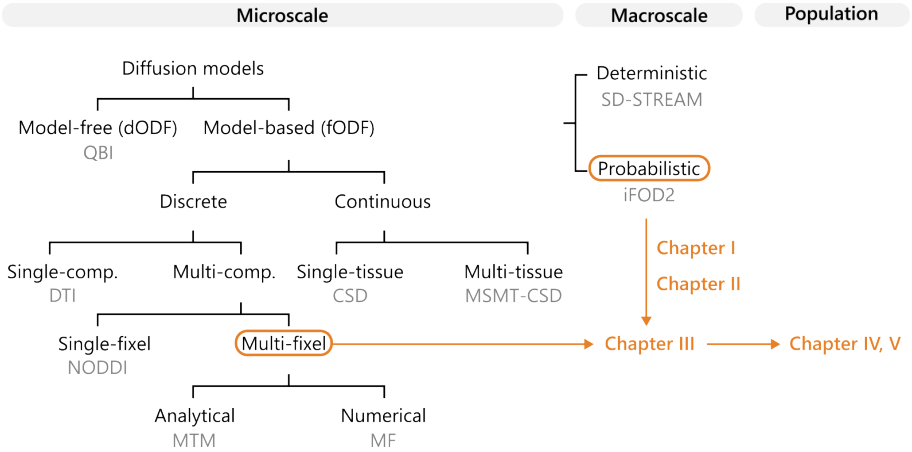

Figure 6: Schematic representation of the topics of interest in this thesis with examples of the models and algorithms (in grey) and the corresponding chapters (in orange).

Part I

Methodology

"*Made up of a dozen billion microscopic nerve-cell units interconnected by millions upon millions of conducting nerve-threads weaving incredibly intricate patterns, the brain, as an object of research, presents a defiant challenge to its own ingenuity.*"

-William Feindel, 1975

To unravel the complex network of neural fibers and their microstructural properties, and thereby inching closer to a deeper understanding of the brain and the intricate patterns of its neural pathways, several algorithms, approaches and framework were developed.

First, in Chapter 1, the tractography algorithms themselves and the possible improvements in terms of obtaining specific neural fiber bundles were investigated. To illustrate the potential applications of a modified tractography algorithm, the focus was placed on short association fibers in the subcortical white matter, also known as U-fibers, depicting the connections between neighboring gyri. The tractography of U-fibers is challenging due to the geometry of the cortical folds and the sharp turns along the cortical surface. Increasing the maximum angle between tractography steps to generate these streamlines also increases the occurrence of biologically implausible streamlines. To mitigate this issue, we propose to replace the fixed maximum angle value in tractography algorithms by an *angular map*, allowing higher angles at the interface between grey and white matter. This enables a more accurate tracking of U-fibers, while keeping a low number of false positive streamlines. Although the angular map was designed to increase the probability of obtaining U-fibers, the proposed algorithm can also be applied to other purposes, such as allowing different angles in other brain areas depending on the intended application.

Another approach to remove those spurious streamlines is to apply post-tractography filtering algorithms. Such a method is described in Chapter 2, where a filtering algorithm based on streamline orientation and density along an average trajectory was developed. Tract extraction from whole-brain tractograms requires either an extensive knowledge of inclusion and exclusion zones or manual efforts to obtain clean tracts. The automated filtering of spurious streamlines can accelerate this extraction process. The proposed algorithm is applicable to a wide variety of tracts with a high and low density. It offers efficient filtering and provides a conservative filtering preserving tract morphology. Additionally, the computed average trajectory enables the analysis of metrics in multi-fixel models along the tract pathway.

The tracts obtained with the methods developed in Chapter 1,2 benefit from the advances in MRI technology, which have enabled richer multi-shell sequences to be implemented in diffusion MRI, allowing the investigation of both the microscopic and macroscopic organization of the brain white matter. Furthermore, the emergence of advanced diffusion models has enabled a more detailed analysis of brain microstructure by estimating the signal received from a voxel as the combination of responses from multiple fiber pop-

ulations. However, disentangling the individual microstructural properties of different macroscopic white matter tracts where those pathways intersect remains a challenge. In Chapter 3, we introduce a framework combining the microscopic and macroscopic scales to unravel multi-fixel microstructure by utilizing tractography. The framework includes a new algorithm, estimating the microstructure of a specific white matter tract with angular weighting. Our framework grants considerable freedom as the inputs required, a set of streamlines defining a tract, such as the ones in Chapter 1,2, and a multi-fixel diffusion model estimated in each voxel, can be defined by the user. The framework also provides estimations of the microstructure at the streamline level, volumetric maps for visualization and mean microstructural values for the whole tract. The angular weighting algorithm shows increased accuracy, robustness to uncertainties in its inputs and maintains similar or better reproducibility compared to commonly used analysis approaches. UNRAVEL will provide researchers with a flexible and open-source tool enabling them to study the microstructure of specific white matter pathways with their diffusion model of choice.

Chapter I

Tractography of the subcortical U-fibers using a position-dependent maximum angle

Extended version of an abstract accepted as:
Delinte N, Dessain Q, Dausort M, Vanden Bulcke C, Macq B (2023) Tractography of the subcortical U-fibers using a position-dependent maximum angle. Proc. Intl. Soc. Mag. Reson. Med. 31 [41]

1.1 Introduction

Subcortical U-fibers are short association fibers within the cortex or in the outer parts of the subcortical white matter, representing connections between neighboring cortical areas [42]. These U-fibers are thought to be involved in multiple neurological and psychiatric diseases, such as in multiple sclerosis [43] and Alzheimer's disease [44]. Through a process known as tractography, diffusion MRI enables the visualization of potential neural connections between brain regions. While this has been extensively investigated for long-range association connections within deep white matter [45, 46, 37, 47, 48], where tracts predominantly consist of mostly straight fibers occupying large volumes, tracking U-fibers is accompanied by additional difficulties. In contrast to the relatively straightforward geometry of major white matter tracts, tracking U-fibers presents a more intricate challenge due to the geometry of the cortical folds, requiring sharp turns to cover the cortical surface [49]. Obtaining U-fibers in a whole-brain tractogram requires a higher maximum angle between tractography steps to follow subcortical fibers along the cortical folds. However, a higher maximum angle increases the probability of generating spurious streamlines, increasing the post-processing steps required to refine the obtained tracts.

Recently, there has been a renewed interest in the tracking and classification of short association fibers, with the creation of U-fiber specific atlases [50] and the development of methods aimed at filtering out spurious streamlines from U-fiber bundles [51]. These methods often use atlas-based approaches to delineate the localization of U-fiber bundles, then compute the distance for each streamline within the bundle to an average centroid streamline to remove streamline with distant shape, end points or trajectory.
Other approaches combine post-tractography algorithms with anatomical priors on the cortical parcellations, end points and streamline lengths characterizing short association fibers. For example, in [52], the authors used, amongst other criteria, surface seeding and streamline length to obtain whole-brain U-fiber tractograms. However, these methods often require either a long computation time, or involve multiple steps or programs.
Another approach to address the issue of varying optimal tractography parameter values across different white matter regions is to generate multiple tractograms, each using its own set of parameters, and then combine the outputs before filtering redundant streamlines, a process known as Ensemble Tractography [53].

In contrast, less effort has been directed towards directly adapting tractography algorithms to increase the probability of generating U-fibers within

whole-brain tractograms. We propose to replace the fixed maximum angle value in tractography algorithms with an *angular map*, thereby allowing different values of maximum angle between tractography steps depending on the position in the brain. Allowing a higher angle at the interface between grey and white matter while keeping lower values in deep white matter enables a more accurate tracking of subcortical U-fibers in whole-brain tractograms, while keeping a low number of false positive streamlines. This conceptually simple modification does not rely on predefined atlases or require any other additional programs or imaging modalities.

1.2 Theory

The proposed modification relies on two core concepts, the modified tractography algorithms and the creation of the variable angle maps used as inputs.

1.2.1 Modified tractography algorithm

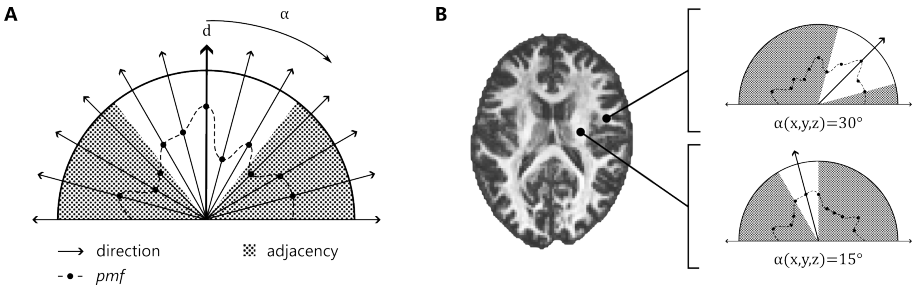

Figure 1.1: Schematic representation of **A** the available new directions from a direction $\hat{\mathbf{d}}$, the probability mass function (*pmf*) and the maximum angle α in **B** different points of the brain.

The proposed modification is compatible with most tractography algorithms, as the maximum angle is a widely used concept in tractography. In this case, we adapted the probabilistic tractography algorithm from DIPY [54] to allow arrays in addition to single scalar values as input parameter for the maximum angle variable α_{max}. The maximum angle variable becomes an *angular map* dependent on the position (x, y, z) of the tractography step

$$\alpha_{max} \rightarrow \alpha_{max}(x, y, z),$$

which impacts the adjacency matrix $\mathbf{M}_{adj} \in \{0, 1\}^{d \times d}$ used to compute the allowed directions from the current direction $\hat{\mathbf{d}}$ (Fig. 1.1A). In the original

algorithm, a single adjacency matrix associated with the α_{max} value was defined, where each pair of directions (d, d) was assigned a value of 0 if the angular distance between them exceeded α_{max}, and 1 otherwise. To avoid computing an adjacency matrix for each voxel, a dictionary of adjacency matrices is precomputed for each integer angle present in the angular map. The probability mass function *pmf*, representing the probability of each discrete direction to be selected, bounded by α_{max} is obtained by

$$pmf_{lim} = pmf(x, y, z) * \mathbf{M}_{adj}(\alpha_{max}(x, y, z), \hat{\mathbf{d}}).$$

The new direction is then selected amongst the directions which have a $pmf_{lim} > 0$ in a classic probabilistic tractography approach. Since the maximum angle $\alpha_{max}(x, y, z)$ is dependent on the position, different points in the brain now possess different *pmf* profiles, as displayed in Fig. 1.1B.

1.2.2 Creation of the angular map

Several methods can be employed to create an angular map, including utilizing white matter masks, whole-brain segmentation, or personalized approaches tailored to specific use cases where the angle is required to change in specific areas. Two approaches using only the diffusion data are described below, although other approaches are possible depending on the intended end result. In both cases, the intended purpose was to increase the maximum angle along the cortical folds enabling streamlines to follow the sharp cortical turns, characteristic of short association fibers.

Based on a white matter mask Binary white matter masks can be used as a basis for the creation of the angular map. In this case, the estimated white matter fODF was utilized to create a binary mask.
The fODF estimated by CSD, on which most tractography algorithms rely, can be represented in its spherical harmonics form. In this representation of the white matter fODF, areas with a higher intensity in the order 0 correspond to areas of white matter. By applying a threshold to these maps, an approximate white matter mask can be obtained. A threshold near the default value of 0.1 is recommended for white matter segmentation. Increasing this threshold will extend the cortical depth with a higher maximum angle, whereas lowering it will decrease the cortical depth. An angular map can then be derived from the white matter mask by applying the steps described in Algorithm 1.

An example of an angular map obtained from a binary mask generated from the white matter fODF obtained with MSMT-CSD with an intensity threshold set to 0.1 is shown in the top row of Fig. 1.2. Using this approach,

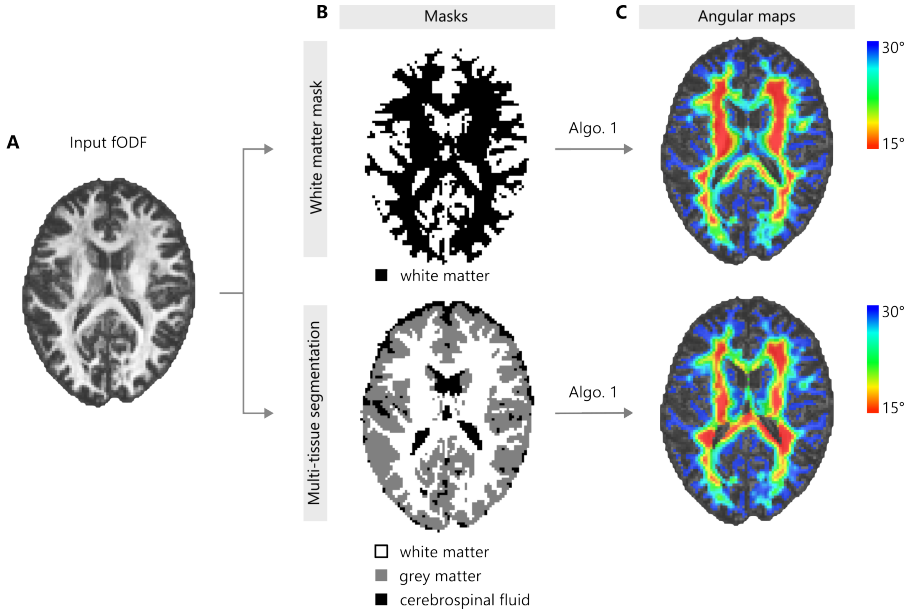

Figure 1.2: Creation of angular maps with a higher maximum angle near the cortical surface from the fODF (**A**) with a binary white matter mask and a multi-tissue segmentation. The masks created from the fODF (**B**) are transformed through a series of operations, described in Algorithm 1, to obtain maps with a variable maximum angle (**C**).

white matter near the CSF and in the corpus callosum is considered to be superficial, i.e., near the white matter interface, and is affected by the increased maximum angle.

Based on brain multi-tissue segmentation Beyond binary masks, multi-tissue brain segmentation can also be employed. The separation of the three tissues into separate response functions in MSMT-CSD can be utilized to give an approximation of white matter, grey matter and CSF segmentation by using the order 0 of the white matter fODF and the estimated partial volumes of GM and CSF, respectively. The steps to obtain the angular map are described in Algorithm 1.
The resulting angular map is similar to the angular map obtained with the binary mask, with a higher angle near the cortical surface. The difference lies in the areas near the ventricles, which are no longer considered to be near the cortical surface and thus no longer have the higher maximum angle (bottom row of Fig. 1.2), and in the cerebellum, which now benefits from an improved white matter, grey matter segmentation.

Algorithm 1 Angular map creation

Require: ODF_{WM}, AND (ODF_{GM}, ODF_{CSF} OR `threshold`)
  if ODF_{GM}, $\text{ODF}_{CSF} \nexists$ **then**
    `grey_matter` = ODF_{WM}[0] < `threshold`
    `white_matter` = ODF_{WM}[0] >= `threshold`
  else
    `seg` = argmax(ODF_{WM}[0], ODF_{GM}, ODF_{CSF})
    `grey_matter` = `seg` == 1
    `white_matter` = `seg` == 0
  end if
  dilate(`grey_matter`, 4mm)
  `map`[`white_matter`] = `min_angle`
  `map`[`grey_matter`] = `max_angle`
  `angular_map` = gaussian_smoothing(`map`)
  return `angular_map`

1.3 Materials & Methods

1.3.1 Datasets

The methodology described in the previous section was applied to two datasets to visualize the results on in vivo and synthetic diffusion data.

Experiment I: In vivo

In the first experiment, an in vivo dMRI scan of a healthy adult participant was performed on a 3T GE SIGNA Premier scanner with the following parameters: TR = 4842 ms, TE = 77 ms, 2 mm isotropic voxels (in-plane FOV: 220x220 mm^2), Δ = 35.7 ms, δ = 22.9 ms, 64 gradients at b = 1000, 32 at b = 2000, 3000, 5000 s/mm^2, and 7 interspersed b0 images. Preprocessing included thermal denoising [55], Gibbs ringing correction [56], eddy-current distortion and movement correction [57]. A 3D T1 image (TE = 2.96ms, TR = 2188.16ms, TI = 900ms, 156 slices, 1mm isotropic, in-plane FOV: 256x256mm^2) was also acquired.

To study the impact of the proposed algorithm on short association fibers, three regions of interest (ROIs) were placed in the hand motor cortex, somatosensory cortex and in the middle frontal gyrus to isolate U-fibers between adjacent gyri. The right middle frontal gyrus was chosen for its role in numeracy [58], which is linked to hand motor function [59].
To analyze the impact on long association fibers, the frontoparietal part of the arcuate fasciculus (AF) tract was extracted from the whole-brain tractography

using White Matter Query Language (WMQL) [37]. The regions defining the AF were derived from the FreeSurfer parcellation of the Desikan-Killiany atlas [60].

The angular map (Fig. 1.3B), obtained with the binary white matter mask approach, was utilized in the modified probabilistic tractography algorithm.

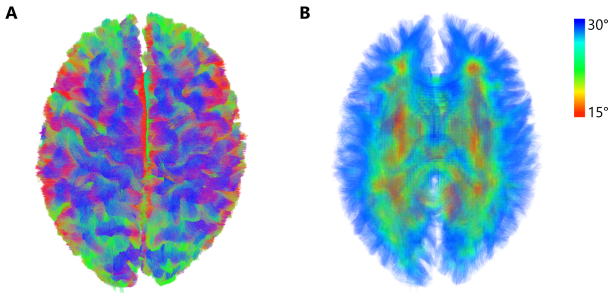

Figure 1.3: Whole-brain tractogram of a healthy participant with **A** directional colors and **B** the varying maximum angle with low values (in red) in the deep white matter and higher values (in blue) near the cortical folds.

Experiment II: Synthetic phantom

Secondly, a synthetic phantom from the Diffusion-Simulated Connectivity (DiSCo) dataset [61] (Fig. 1.4A) was used to compare the connectivity measures of 16 regions to a known ground truth. The dMRI protocol was composed of 360 gradients, equally spread over 4 b-value shells at b=1000, 1925, 3094, 13191 s/mm^2. The DiSCo1 phantom was selected in the 2x2x2mm resolution to match the resolution of the in vivo dataset. The tractography was performed with and without the addition of Rician noise on the diffusion data, with a signal-to-noise ratio (SNR) of 10.

The resulting angular map, also obtained from a binary white matter mask, and tractogram are displayed in Fig. 1.4.

1.3.2 Local modeling & tractography

In both the in vivo and synthetic data, the multi-shell multi-tissue constrained spherical deconvolution (MSMT-CSD) [26] algorithm was utilized for the estimation of the white matter fODF. The modified probabilistic tractography described in the previous section was tested with angular maps based on a binary white matter mask derived from the white matter fODF obtained with

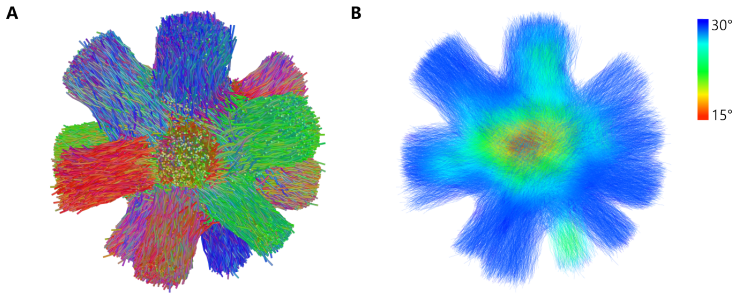

Figure 1.4: Tractogram of the DiSCo1 dataset using the varying angle with **A** directional colors and **B** the varying angle values of the angular map. Low and high maximum angle values are represented in red and blue, respectively.

MSMT-CSD with a threshold of 0.08. The python implementation used for the creation for the angular map is open-source and available[1]. The maximum angle was set to be within 15°< α_{max} <30°. The results were compared to the default probabilistic algorithm with α_{max} =15°, 22° and 30°. In all cases, seeds were placed inside the white matter mask based on the white matter fODF with a density of 8 seeds per voxel.

The tractograms obtained from the synthetic dataset were filtered with SIFT [33] and the connectivity matrix of the 16 regions of interest was computed.

1.4 Results

1.4.1 In vivo: Short association fibers

The streamlines linking the motor cortex to the adjacent gyri isolated from the tractogram in Fig. 1.3 are displayed in Fig. 1.5. The maximum angle of 15° (Fig. 1.5B) was too low to track the subcortical connections between the hand motor cortex and somatosensory cortex due to geometry of the cortical fold. A maximum angle of 30° (Fig. 1.5D) found a large number of connections between both regions but also produced several biologically implausible streamlines passing through deep white matter regions. The varying angle of the angular map ranging from 15° to 30° (Fig. 1.5A) produced no such streamlines while connecting both gyri to the motor cortex. The angular map also produced more streamlines than the intermediary value of 22° (Fig. 1.5C), which presented less streamline density.

[1] `https://github.com/DelinteNicolas/UTracto`

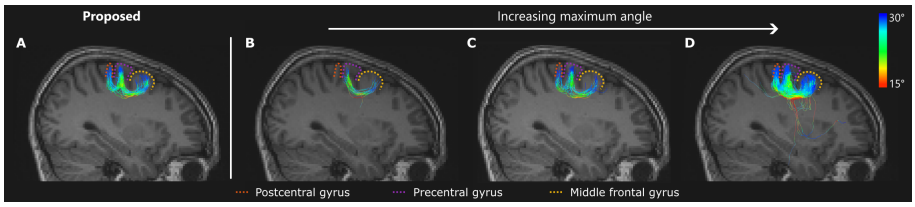

Figure 1.5: Streamlines connecting the hand motor cortex to the somatosensory cortex and the frontal middle gyrus of a single subject obtained with **A** the varying angle of the angular map ranging from 15° to 30° based on the angular map, **B** a maximum angle of 15°, **C** a maximum angle of 22° and **D** a maximum angle of 30°. All streamlines are colored using the angular map used for **A** to show how the streamline would have been affected by the varying angle.

1.4.2 In vivo: Long association fibers

In the main white matter tracts, such as the frontoparietal part of the AF (Fig. 1.6), increasing the maximum angle produced more stray and biologically implausible streamlines (Fig. 1.6C,F). The angular map (Fig. 1.6A,D) produced more spurious streamlines than the 15° maximum angle, but less than the 30° maximum angle. The angular map also provided a greater angle near the cortex.

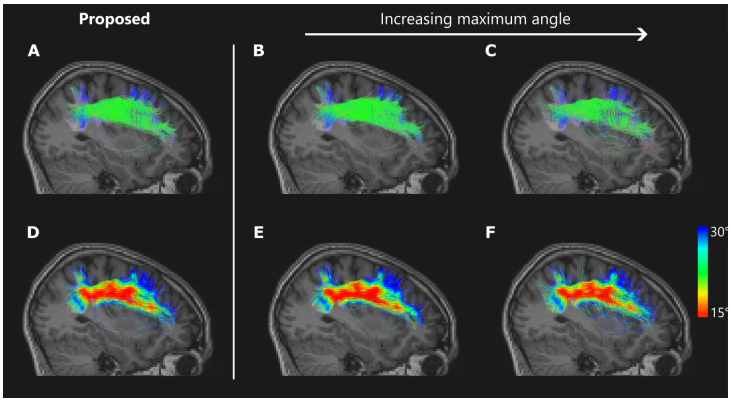

Figure 1.6: Tract of the frontoparietal part of the arcuate fasciculus of a single subject obtained with **A**,**D** the varying angle ranging from 15° to 30° based on the angular map, **B**,**E** a maximum angle of 15°, and **C**,**F** a maximum angle of 30°. All streamlines in **D**,**E**,**F** are colored using the angular map used for **A** to show how the streamline would have been affected by the varying angle.

1.4.3 DiSCo Phantom

The connectivity matrices obtained in the DiSCo1 dataset in Fig. 1.7 showed the lowest correlation to the ground truth with a maximum angle of 15°. This angle also produced two false negatives between ROI 7 and ROI 2 & 4, which are both adjacent to ROI 7 and require a high angle to connect. Using the angular map or the 30° angle produced similar scores, except for a higher number of false positive streamlines in the 30° angle. Furthermore, the angular map had a higher correlation, and less false positives and negatives compared to the maximum angle of 22°.

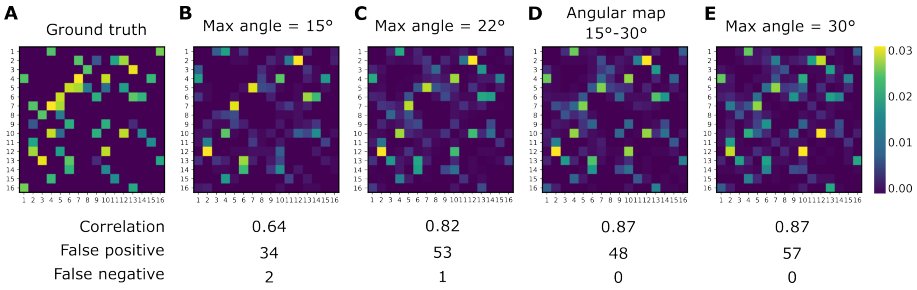

Figure 1.7: Connectivity matrices of the DiSCo1 dataset with **A** the ground truth values, **B** a maximum angle of 15°, **C** a maximum angle of 22°, **D** the varying angle ranging from 15° to 30° based on the angular map and **E** a maximum angle of 30°. All matrices are symmetric, and are normalized to sum to one.

Fig. 1.8A illustrates the evolution of the interpolated number of false negative and false positive streamlines as the maximum angle was increased. The number of false positives increased and the number of false negatives decreased. At a maximum angle of 26°, all the streamline connections were found and further increasing the maximum angle only increased the number of false positives connections. The connectivity obtained with the angular map also found all connections but with a lower number of false positives, with 48 false positives compared to the 57 found at 26°.

The addition of Rician noise to the synthetic diffusion data displayed in Fig. 1.8B increases the number of false positives connections, whereas the number of false negatives decreases to zero for every angle between 15° and 30°. The number of false positives obtained with the angular map is similar to the value obtained for a maximum angle of 22°. The correlation increases from 0.62 to 0.91 as the maximum angle increases from 15° to 30°. The connectivity matrix obtained with the angular map presents a score of 0.89.

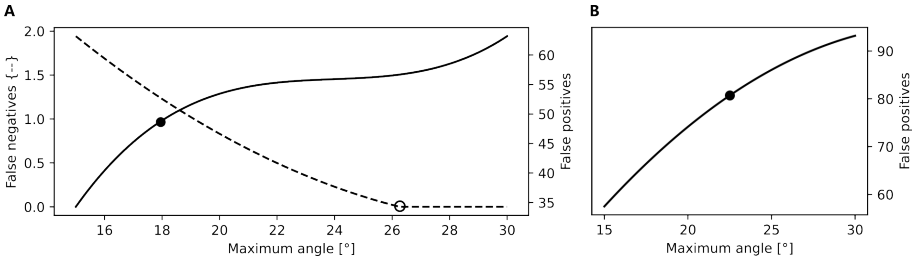

Figure 1.8: Plot of the average number of false negative (dashed line) and positive (solid line) streamlines in the connectivity matrix of the DiSCo phantom estimated with a maximum angle ranging from 15° to 30° for **A** noiseless data and **B** SNR=10. The values are interpolated from the values obtained at 15°, 18°, 22°, 26° and 30°. The number of false positives (•) and false negatives (◦) of the angular map are represented with dots.

1.5 Discussion

1.5.1 Increased accuracy for U-fibers

The adjustment made to the tractography algorithm demonstrated the ability to decrease the number of biologically implausible streamlines in whole-brain tractograms, while allowing a higher maximum angle near the cortical surface necessary for tracking U-fibers. Thereby limiting the need for exclusion zones or additional post-processing steps. Its performance in capturing short association fibers was above the results of tractograms generated using a single maximum value. While the modified algorithm had a minimal impact on long association fibers, it did lead to a slight increase in the number of spurious streamlines.

In the synthetic phantom experiment, the angular map combined the desired properties of low and high maximum angles, resulting in a low number of false positives and false negatives streamlines. Without using the angular map, exceeding a maximum angle of 26° only resulted in more false positives without improving accuracy. Therefore, the optimal single value for the maximum angle falls within the lower range, depending on whether the goal is to minimize false positives or false negatives. The angular map bypasses this trade-off and allows users to get the benefits of both outcomes.

Furthermore, the configuration of adjacent ROIs in the phantom was similar to the geometry presented by U-fibers, indicating that higher angles are required to avoid false negative streamlines.

1.5.2 Flexibility of usage

While the experiments were designed around an increased probability of obtaining U-fibers with probabilistic tractography algorithms, the core concepts in the methodology presented in this study offer considerable flexibility for various applications. The angular maps generated can be used for other purposes, such as enabling different angles in specific brain regions based on the intended tractography goals. Whole-brain angular maps could be developed based on anatomical knowledge of white matter tract properties and expert consensus, providing a more tailored approach to tractography. Additionally, the ability to create patient-specific angular maps could be useful for applications involving deformed brains.
To obtain a similar outcome without modifying the maximum angle, a variable step size could be used instead. This method could prove beneficial for tractography algorithms that would not rely on a maximum angle or would not allow its modification.
Furthermore, the position dependency of the maximum angle can be applied to most tractography algorithms, whether deterministic or probabilistic.

1.5.3 Low increase of computational cost

This flexibility and increased accuracy come with minimal additional computational cost compared to other alternatives. Since the method is a direct modification of the tractography algorithm, it does not require additional software, libraries, or a significant increase in computational resources. In contrast, other methods such as Ensemble Tractography, which involve additional steps or global optimization processes, often result in increased complexity, memory usage, and processing time. The increased runtime and memory usage of the proposed method are negligible.

1.5.4 Limitations & future perspectives

As previously mentioned, the modification of the tractography algorithm was exclusively applied to a traditional probabilistic algorithm. Investigating the application of the same modification to more advanced algorithms, such as iFOD2 [32] or PTT [62], would be of interest to determine whether similar improvements are achieved or if the enhancements are more marginal.
Once the modification is applied to the iFOD2 algorithm, the results could be compared to other U-fiber tractography tools, such as 'U-fiber analysis' [63], which combines multiple programs and algorithms to generate U-fibers. Although this tool is limited to 16 U-fiber bundles, it could serve as a benchmark

to compare the outputs between the proposed method and more complex approaches in these tracts.
The output tracts could also be compared to U-fiber bundle atlases [50] using measures such as the cluster confidence index [64] for the resulting streamlines or by computing the average bundle of the minimum average direct-flip distance [65] to a reference centroid streamline. These comparisons, along with the methodology described in [51], or frameworks such as Tractometer [66] could provide tools able to assess the impact of the proposed methodology compared to other approaches.

Regarding the specific application of this algorithm to short association fibers, additional challenges persist, particularly in the context of group-wise analysis of U-fibers as inter-subject variation in cortical folding introduces further complexity to inter-participant analyses.

More generally, the angular maps created could benefit from more information, such as T1- or T2-weighted brain segmentation. The two methods described to create the location-dependent parameter map in section 1.2.2 are only two possibilities and were only based on diffusion data to show the impact of the proposed addition to tractography without the need for external tools or algorithms.

The addition of noise to the diffusion data reduced the number of false negative connections and increased the number of false positives. Investigating lower ranges of maximum angle values might be beneficial when dealing with noisy data.

1.6 Conclusion

This proof of concept demonstrated that simple modifications to tractography algorithms could enhance accuracy and reduce the occurrence of spurious streamlines. The introduction of a position-dependent maximum angle allows for a more precise streamline generation, making tractography better suited for specific purposes. Specifically, in the case of short associations fibers, allocating a higher maximum angle near the cortex enabled the generation of subcortical U-fibers along the cortical folds, while maintaining a low number of false positive streamlines and with minimal impact on the tracking of long-range association fibers. Integrating this modification into other tractography algorithms, alongside purpose-specific angular maps, has the potential to improve the overall accuracy of the tractograms produced and allow researchers to inspect the white matter tracts with greater ease.

Chapter II

Filtering of spurious streamlines via streamline orientation and pathway density

---

Extended version of an abstract accepted as:
Delinte N, Macq B (2024) Tractography of the subcortical U-fibers using a position-dependent maximum angle. Proc. Intl. Soc. Mag. Reson. Med. 32 [67]

2.1 Introduction

Probabilistic tractography has uncovered more neural pathways compared to deterministic algorithms by allowing orientations associated with a lower diffusivity to contribute to the propagation of streamlines. While this has enabled a more complete overview of the existing pathways, it has also brought with it a higher number of false positive streamlines [68, 69]. In bundles extracted by targeting specific regions of interest (see Fig. 2.1A), these false positives often appear as spurious streamlines (Fig. 2.1B).

Previously, removing these unwanted streamlines from the obtained tract required the addition of exclusion and inclusion zone to restrict the possible pathway of the streamlines or the manual removal of each spurious streamline. Both of these methods are time intensive, require expert knowledge and must be repeated for each tract or group of tracts.

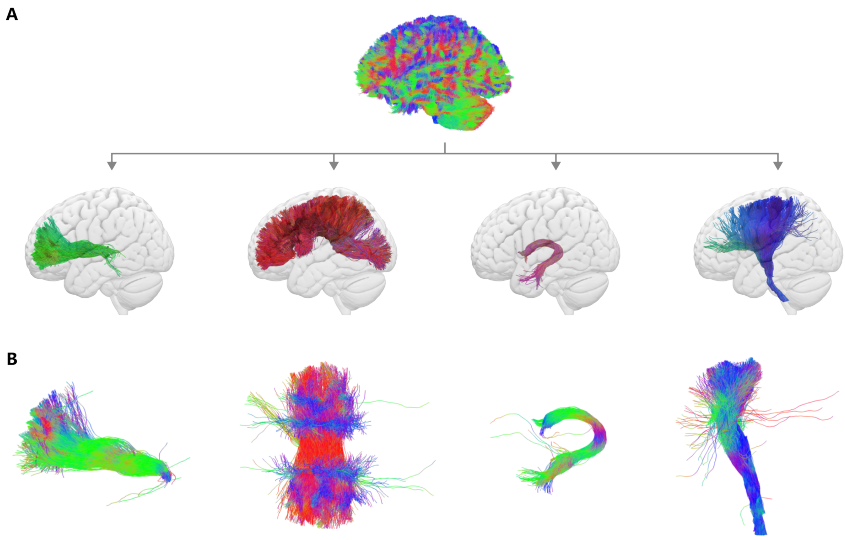

Figure 2.1: A Extraction of specific white matter tracts from a whole-brain tractogram. **B** Examples of tractography bundles with spurious streamlines. From left to right: anterior thalamic radiation, corpus callosum, fornix and corticospinal tract.

More recently, automated filtering methods have been developed around different strategies. Several approaches have investigated whole brain filtering such as SIFT [33], COMMIT [35], and LiFE [70]. These methods aim to improve the fit between streamline density and the spherical deconvolution of the diffusion signal in each voxel. The increased biological accuracy can

be increased either by selectively filtering out streamlines or reducing their weights or radii. This ensures that areas with simpler microstructure are not over-populated compared to regions of complex architecture, such as areas presenting fiber crossings.

Another approach to obtain clean tracts is to extract streamlines based on atlases. Several methods have been developed and most of these approaches also provide the ability to perform along tract metric analyses. The TRActs Constrained by UnderLying Anatomy algorithm (TRACULA) [45] was developed to automatically reconstruct a predefined set of 18 major white matter pathways using dMRI data. Streamlines are generated through an atlas-based segmentation approach of the brain. Additionally, the evolution of DTI metrics along these tracts is accessible in their framework.
Similarly, Automating Fiber-Tract Quantification (AFQ) [46] uses an atlas-based segmentation to isolate and clean the streamlines of 18 predefined white matter tracts. AFQ provides along-tract analyses of the tract profile to compare populations. The latest version of AFQ is now compatible with the white matter tracts obtained from RecoBundles [71] and the tract profiles can be obtained for tracts not predefined in atlases. RecoBundles is an algorithm leveraging streamline-based registration and clustering to recognize and extract bundles using prior bundle models. The bundle shape priors are used to detect similar streamlines and bundles in whole-brain tractograms. Another method reliant on RecoBundles is Bundle analytics (BUAN) [47]. BUAN does group comparisons of bundle profiles at specific locations obtained with RecoBundles and can return p-values of the difference between two populations in each of the bundle segments. This algorithm uses atlas and is limited to 80 (originally, 30) predefined bundles but can be extended to work with tracts outside of the predefined set. Another example of bundle extraction algorithm is BundleSeg [48], which uses the minimum average direct-flip (MDF) and fast streamline search (FSS) to automatically segment pre-defined bundles, while keeping a low computation time.
A drawback of these atlas-based tract segmentation methods is their lack of flexibility when the tract of interest is absent from the atlas, or when the tract has been obtained from patient-specific regions of interest.

The last type of approach is neither dependent on a whole brain tractography, supplementary biological information, or on predefined tracts to filter out stray streamline from specific tracts. There are several ways to achieve this result, the base heuristic is to apply a density threshold on the streamline density and to remove streamlines passing through voxels with a low density. Other methods use more advanced tools and algorithms, such as the MDF [65], which computes a distance between streamlines among the same

bundle to detect outlier streamlines. Quickbundles [65] and the cluster confidence index (CCI) [64] are both based on the MDF. QuickBundles performs streamline clustering within a tract by representing the tract using one or multiple centroid streamlines. To utilize the MDF which requires streamlines to have the same number of steps, QuickBundles uses an internal resampling process. The fiber to bundle coherence (FBC) algorithm uses kernel density estimation in the non-flat 5D domain [72]. Outlier streamlines can then be removed by applying a threshold on the relative FBC (RFBC), representing the minimum of the moving average LFBC along a streamline. Another example is BundleCleaner, which utilizes an unsupervised multi-step framework to filter, denoise, and subsample bundles using both point cloud and streamline-based methods [73].

Similarly to the authors of the previously mentioned articles, we believe that the majority of spurious streamlines can be removed using algorithmic criteria, simplifying the process of exclusion zone selection and reducing the need for exhaustive trial-and-error testing for each tract. To achieve this, we have developed tools to efficiently compute the mean tract trajectory, which can be used to clean up tracts and study the microstructure of linear fascicles along their pathways. Our method works independently of the orientation of the tract and does not require biological priors or bundle templates. The input streamlines can be either obtained with a limited number of inclusion regions or with automated tract extraction means, such as WMQL [37]. Our method was compared to four other filtering implementations. The resulting filtered tracts no longer display spurious streamlines while preserving the tract's original shape.

2.2 Theory

Defining general rules will facilitate the generation of cleaner tracts, eliminating the need for an extensive search of exclusion zones or reliance on biological priors, which requires expert knowledge. The proposed methodology contains two main concepts: the filtering process and the use of its byproducts to conduct along-tract analysis.

2.2.1 Filtering of spurious streamlines

We considered two types of spurious streamlines in a tract $\mathcal{T}$: *oversteps* and *missteps* (Fig. 2.2). The number of spurious streamlines for each type can be reduced by removing streamlines that do not respect either of the following criteria.

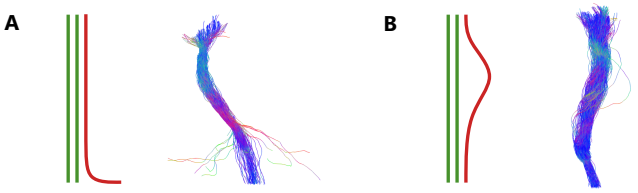

Figure 2.2: Schematic representation (left) and tractography example (right) of the two types of spurious streamlines on a corticospinal tract. **A** Oversteps, which present a coherent pathway but an incorrect end point and **B** Missteps, which have the correct destination but deviate along their pathway.

Oversteps depicted in Fig. 2.2A, refer to inaccuracies in streamline endpoints. This is often caused by streamlines reaching the intended end ROI then branching off and going past the ROI. Another cause would be short streamlines with scattered orientation but within the inclusion zones. These inaccuracies can be detected based on the overall streamline orientation. To achieve this, the endpoints of each streamline i are first extracted and categorized as start ($\mathbf{x}_{start}$) and end points ($\mathbf{x}_{end}$) based on their average streamline direction (Fig. 2.3A,B).

$$\mathbf{u}_i = \mathbf{x}_{i,end} - \mathbf{x}_{i,start}.$$

The orientations of the streamlines, denoted as $\mathbf{u}_i$, are then transformed into polar coordinates $\mathbf{u}_i = (x, y, z) \rightarrow \mathbf{u}_i = (\theta, \phi)$ centered on the average orientation of the tract (Fig. 2.3C-D). Subsequently, the kernel density $\hat{d}_h(\mathbf{u})$ is estimated for all streamline orientations.

$$\hat{d}_h(\mathbf{u}) = \frac{1}{l} \sum_{i=1}^{l} K_h\left(\mathbf{u} - \mathbf{u}_i\right),$$

where l is the number of streamlines in the tract and h the user-defined bandwidth of the symmetric bivariate Gaussian kernel $K_h(\mathbf{x})$

$$K_h(\mathbf{x}) = \frac{1}{2\pi h^2} e^{-\frac{1}{2h^2}\mathbf{x}^T\mathbf{x}}. \tag{2.1}$$

Streamlines $\mathcal{L}$ with an insufficient number of neighbors (i.e., whose density is below the threshold of an isolated point) are then removed from the set $\mathcal{T}$ (Fig. 2.3D).

$$\textbf{Criterion: } \mathcal{L}_i \notin \mathcal{T} \text{ if } \hat{d}_h(\mathbf{u}_i) \leq \frac{n}{2\pi h^2}, \tag{2.2}$$

where n is the approximate number of neighboring streamlines necessary to be classified as non-isolated and $1/2\pi h^2$ the maximum amplitude of a single peak.

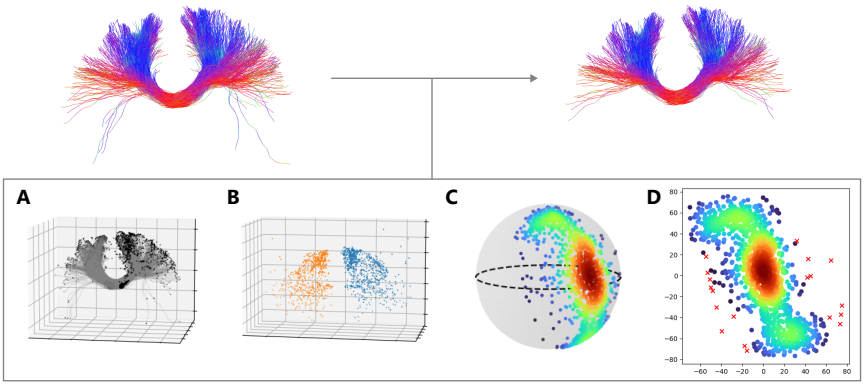

Figure 2.3: Filtering process to remove streamlines with isolated endpoints. **A** Extraction of streamline endpoints. **B** Classification of starts and ends based on mean streamline orientation. **C** Representation of the orientation density of the streamlines. **D** Kernel density estimate and removal of streamline with low orientation density (red crosses).

Missteps illustrated in Fig. 2.2B, represent deviations from the average streamline pathway. These can often be rectified through manual intervention, by adding more inclusion zones along the intended trajectory, at the expense of more time to select these inclusion zones. To address these stray streamlines, an average bundle trajectory is calculated. The computation of the average trajectory proceeds iteratively: planes $\mathcal{P}$ are positioned at the midpoint $\mathbf{m}$ between two nodes, with the normal $\hat{\mathbf{n}}$ of the plane aligned with the direction of these points. A new node is then added to the average trajectory at the centroid c of the points where the streamlines and plane intersect (Fig. 2.4A).

$$\begin{aligned}
\hat{\mathbf{n}}_p &= \mathbf{c}_{p+1} - \mathbf{c}_{p-1} \\
\mathbf{m}_p &= (\mathbf{c}_{p+1} + \mathbf{c}_{p-1})/2 \\
\mathbf{c}_p &= \frac{1}{N}\sum_{i}^{N} \mathbf{x}_{p,i} \qquad\qquad \forall\, \mathbf{x}_{p,i} \in \mathcal{P}(\mathbf{m}_p, \hat{\mathbf{n}}_p) \cap \mathcal{L}_i,
\end{aligned} \tag{2.3}$$

where $\mathbf{x}_{p,i}$ is the position of streamline $\mathcal{L}_i$ where it intersects $\mathcal{P}_p$.
The outlier streamlines are then identified and removed based on their positional density $\hat{d}_h(\mathbf{x}_{p,i})$ at each plane $\mathcal{P}_p$ (Fig. 2.4B).

$$\hat{d}_h(\mathbf{x}_p) = \frac{1}{l} \sum_{i=1}^{l} K_h \left(\mathbf{x}_p - \mathbf{x}_{p,i} \right),$$

with $\mathbf{x}_{p,i}$ the coordinate vector of streamline i at plane p, l the number of streamlines and K_h the symmetric bivariate Gaussian kernel defined in Eq. (2.1). Similarly to the previous criterion defined in Eq. (2.2), isolated streamlines are then removed from the set $\mathcal{T}$.

$$\textbf{Criterion: } \mathcal{L}_i \notin \mathcal{T} \text{ if } \hat{d}_h(\mathbf{x}_{p,i}) \leq \frac{n}{2\pi h^2},$$

where n is the approximate number of neighboring streamlines necessary to be classified as non-isolated and $1/2\pi h^2$ the maximum amplitude of a single point.

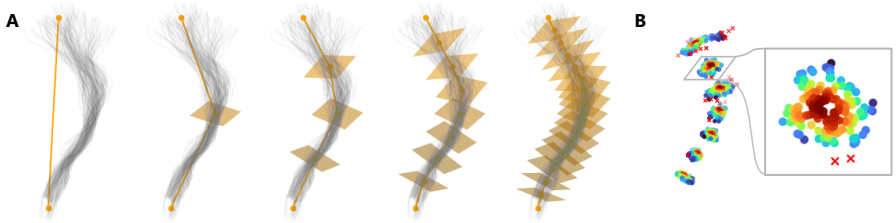

Figure 2.4: Visualization of the filtering process for pathway deviations. **A** An average bundle trajectory is iteratively computed. **B** At each step, outlier streamlines (red crosses) are identified based on their position density on the plane perpendicular to the trajectory.

In both of these criteria, kernel density estimators are used instead of a single Gaussian fit to allow for non-linear tract geometries with multiple pathways or end points. Streamlines away from the average trajectory are thus kept in the tract if they have a sufficient number of neighboring streamlines.

2.2.2 Along-tract analysis

The mean pathway and perpendicular planes previously computed for the streamline filtering can be leveraged to segment the tract into subsections (Fig. 2.7A) to provide along-tract analyses of microstructural metrics (Fig. 2.7B).

To subdivide the volume of the tract into segments, a voxel mask $\mathcal{M}$ is defined using either a binary mask of the voxels crossed by streamlines (*roi*) or a weighted mask of the streamline density per voxel (*tsl*).
Volume segments $\mathcal{R}_p$ of the average streamline pathway are delimited by two

consecutive planes p. For each segment, all the voxels $\mathbf{v}$ in the mask $\mathcal{M}$ that are on the same side S as the midpoint between two adjacent planes $\mathbf{m}$ are considered to belong to that section. For each plane p in a segment,

$$S(\mathbf{v}, p) = \frac{\hat{\mathbf{n}}_p \cdot (\mathbf{c}_p - \mathbf{v})}{|\hat{\mathbf{n}}_p \cdot (\mathbf{c}_p - \mathbf{v})|}, \text{ with } S(\mathbf{v}, p) : \mathbb{R} \rightarrow \{+1, -1\}$$

where $\mathbf{c}_p$ is the centroid defined in Eq. (2.3), i.e., the intersection of the plane p and the average pathway. Next,

$$\forall\, \mathbf{v} \in \mathcal{M}, \text{ if } \begin{cases} S(\mathbf{v}, p) = S(\mathbf{m}, p) \\ S(\mathbf{v}, p+1) = S(\mathbf{m}, p+1) \end{cases} \text{ then } \mathbf{v} \in \mathcal{R}_p.$$

This creates a new set of masks $\mathcal{R}_p$ from a single mask (see Fig. 2.5). The means and deviations over the new subregions can then be appended and plotted to provide the evolution of a microstructural metric along a tract.

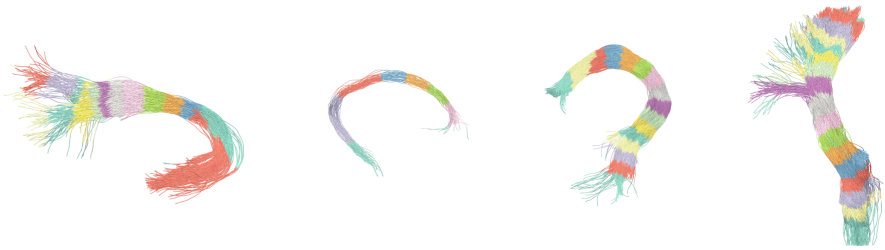

Figure 2.5: Examples of tracts segmented into subsections along their pathway. From left to right: uncinate fasciculus, cingulum, fornix and corticospinal tract.

The implemented code for the algorithms presented in this section is open-source and available at [74].

2.3 Materials & Methods

2.3.1 Data acquisition and pre-processing

The filtering algorithm was tested on tracts obtained from multi-shell dMRI data acquired with the following parameters: TR = 4842ms, TE = 77 ms, 2 mm isotropic voxels, in-plane FOV: 220 × 220 mm^2, Δ = 35.7 ms, δ = 22.9 ms, 64 gradients at b = 1000, 32 at b = 2000, 3000, 5000 s/mm^2, and 7 interspersed b0 images.
Preprocessing of the diffusion data included brain extraction [75], thermal denoising [55], Eddy-current distortion and head-motion correction [57].

2.3.2 Streamline generation

Streamlines were generated using two different methods to verify the effectiveness of the proposed filtering algorithm on tracts obtained via different approaches.

Method 1: using a limited number of inclusion ROIs. Since the objective was to remove the need for an extensive list of inclusion and exclusion ROIs, a maximum of three inclusion regions were used for each tract, with no exclusion regions.

Method 2: using an atlas-based segmentation and anatomical definitions. For this purpose, the white matter query language (WMQL) [37] was used. The tracts created could present a wider variety of streamlines within a single bundle compared to the first method, with short and long fibers as well as multiple pathways or end points.

In both cases, the local modeling was estimated with MSMT-CSD [26] to make use of the multi-shell data and the probabilistic tractography algorithm was iFOD2 [32]. The tractography was carried out with a maximum angle of 15°, step size of 1 mm and cutoff of 0.1.

2.3.3 Streamline filtering

The streamline filter generated with our method was compared with filtering techniques employing density thresholding, RFBC [72], CCI [64] and BundleCleaner [73]. The filtering algorithms were tested on three tracts of varying morphology and streamline density: the arcuate fasciculus (AF), the uncinate fasciculus (UF) and the middle posterior section of the corpus callosum (CC).

To compare the effects of different filtering algorithms on the tract, various metrics were reported, including the number of streamlines removed, the overlap and the average absolute difference in density per voxel. The overlap compared the footprint of the input $\mathcal{M}_A$ and output $\mathcal{M}_B$ of the filtering process

$$\text{overlap}(\mathcal{M}^A, \mathcal{M}^B) = \frac{|\mathcal{M}^A \cap \mathcal{M}^B|}{\mathcal{M}^A}, \tag{2.4}$$

where $\mathcal{M}^A, \mathcal{M}^B$ are binary mask of the voxels containing tracts A and B. The difference in density relies on the total length of streamline segments per voxel l_v, normalized by the total length of the streamlines in the tract

$$\delta(A,B) = \sum_v \text{abs}\left(\frac{l_v^A}{\sum_v l_v^A} - \frac{l_v^B}{\sum_v l_v^B}\right).$$

2.3.4 Along-tract analysis

To illustrate the along-tract analysis, the fractional anisotropy (FA) of a bundle of the corpus callosum was estimated with a single-fixel (DTI [76]) and multi-fixel model (DIAMOND [20]) with UNRAVEL [77] to visualize the impact of crossing fibers on metric estimation. Both estimations were done using the *tsl* weights for the weighted mean per subregion $\mathcal{R}_p$.

The segmentation into subsections presented in the methodology was compared to the segmentation performed with the BUAN framework. In both cases, the corpus callosum, corticospinal tract, and arcuate fasciculus were each segmented into 32 segments along their pathways.
The along-tract profiles of the FA_{DTI} estimates for these tracts were compared to the profiles obtained with AFQ. The profiles were sampled at 32 intervals. Conventionally, AFQ uses weights based on the distance to an average centroid streamline to determine the contribution of each streamline to the profile estimation. This weighting was disabled to enable a more direct comparison between the two methods.

To further examine the usefulness of along-tract analysis in regions of crossing fibers, the intersection of the corpus callosum with the frontal aslant tract (FAT) was also investigated with the tract-specific FA obtained with DIAMOND.

2.4 Results

2.4.1 Streamline filtering

The results of the comparison of the filtering methods are displayed in Fig. 2.6. The arcuate fasciculus (AF) shown in Fig. 2.6A had a high number of streamlines and presented a complex shape with multiple end regions. The spurious streamlines were removed in all methods. However, the computation time of RFBC and BundleCleaner greatly increased with the number of streamlines. Furthermore, RFBC resulted in the loss of most of the AF's shape. The proposed method removed spurious streamlines while preserving more of the shape of the AF compared to other techniques.
The uncinate fasciculus (UF) displayed in Fig. 2.6B had a low number of streamlines and presented spurious streamlines at the top, which all methods suc-

cessfully eliminated. However, density thresholding and CCI removed many coherent streamlines due to the low density of the tract.
Regarding the results for the corpus callosum bundle shown in Fig. 2.6C, all methods yielded similar outcomes, with varying degrees of streamline removal. The proposed method did not eliminate all spurious streamlines in this case.

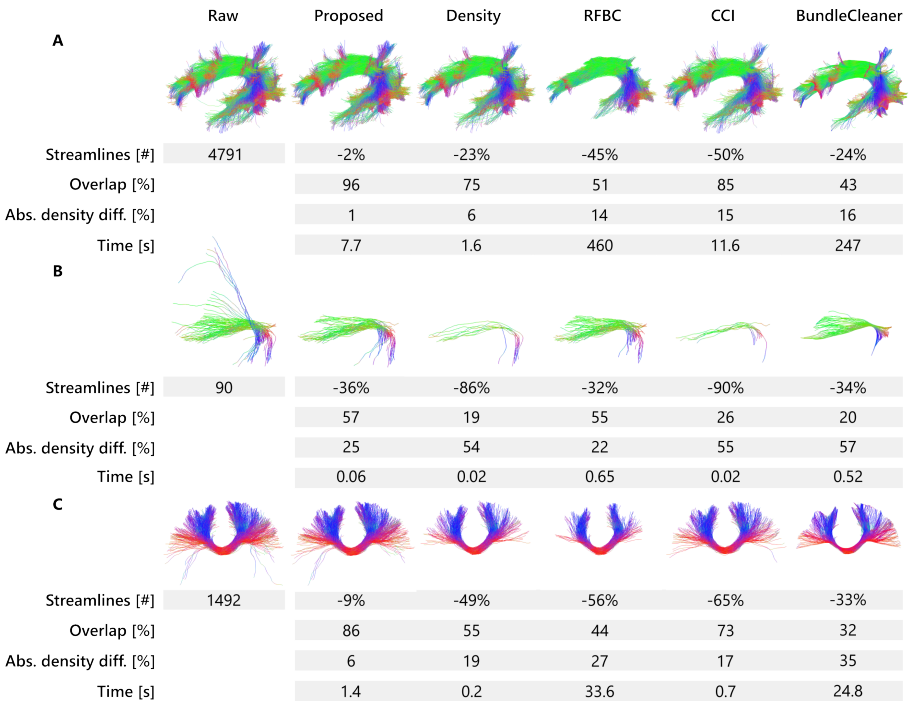

Figure 2.6: Filtering of tracts of the **A** arcuate fasciculus, **B** uncinate fasciculus and **C** the middle posterior bundle of the corpus callosum using five filtering methods: the proposed method, density thresholding, RFBC, CCI and BundleCleaner. All results were obtained with the default parameters, except for the corpus callosum with BundleCleaner which provided no results. The execution time, number of filtered streamlines, overlap and absolute difference in density are reported below each filtered tract.

Regarding the overlap defined in Eq. (2.4) between the tracts before and after filtering, the proposed algorithm produced tracts with greater overlap compared to the other methods. Additionally, the proposed method exhibited a lower absolute density difference between the two tracts, except for the UF where RFBC displayed in a lower difference. BundleCleaner had the highest absolute density difference across all three tracts.

2.4.2 Along-tract analysis

The along-tract analysis on Fig. 2.7 highlighted the benefit of multi-fixel analysis in comparison to single-fixel models, such as DTI. With FA_{DTI}, a decrease in values was observed at the beginning and end of the tract, due to the presence of crossing fibers in the left and right hemispheres. Conversely, in the middle of the tract where a single fiber population exists, the results aligned more closely with the values obtained through $FA_{DMD,ang}$.

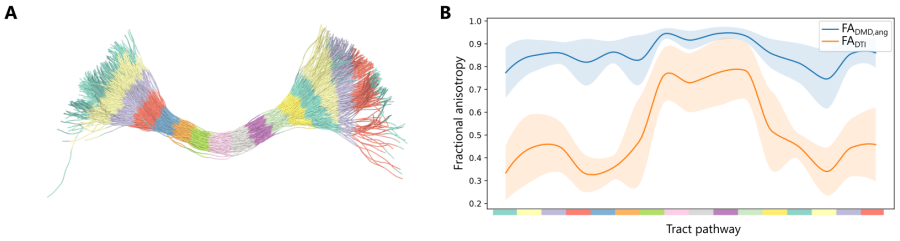

Figure 2.7: **A** Streamlines passing through the anterior midbody of the corpus callosum divided into twelve subregions along its pathway. **B** Evolution of the FA along the pathway estimated with DTI (orange) and DIAMOND (blue) with UNRAVEL.

The subdivision of white matter bundles into segments using the proposed method was similar to the subdivision obtained with BUAN. Several differences were noted: the extremities of the corpus callosum bundle were more disorganized with the proposed method (Fig. 2.8A). The subdivisions of the corticospinal tract were similar, but BUAN displayed larger regions for the start and end portions (Fig. 2.8B). In the case of the AF, the proposed method also resulted in a more disorganized segmentation. However, the BUAN segmentation incorrectly attributed the same labels to the start and end regions due to the AF's arched shape (Fig. 2.8C).
The along-tract profiles derived from the proposed method were similar to those obtained using AFQ, except for the AF (Fig. 2.8C), where the proposed method showed an increased noise in its estimation. Overall, the profiles generated with AFQ were smoother and displayed lower values at the extremities.

Examining the intersection of the CC with the FAT in Fig. 2.9A and their respective microstructure metrics in Fig. 2.9B, revealed not only diverse microstructure variations along their trajectories but also distinct estimated FA values in the region of intersection. In this crossing region, the FA was estimated to be around 0.85 and 0.82 for the FAT and CC, respectively.

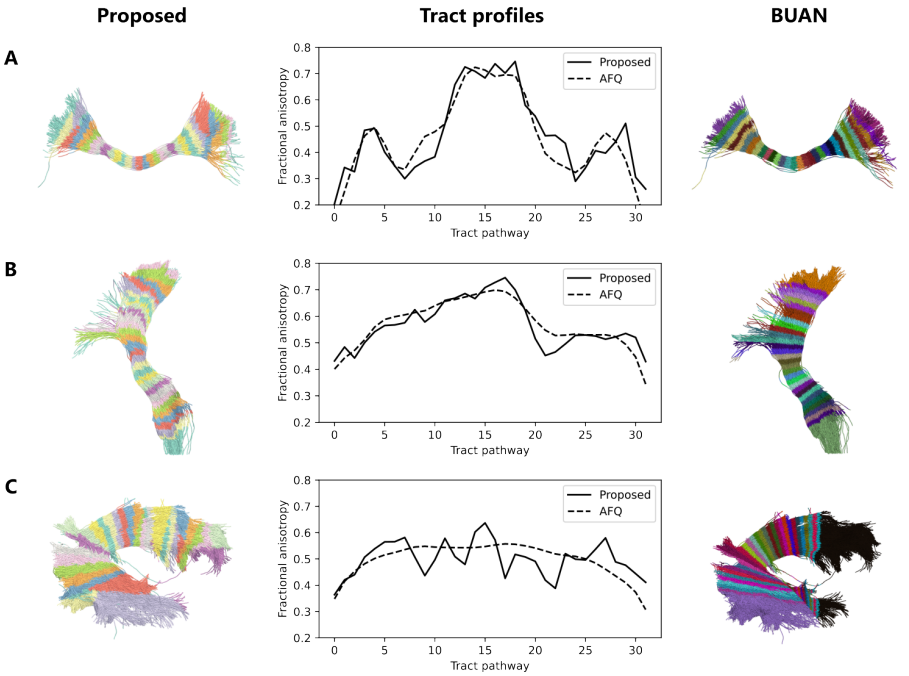

Figure 2.8: Comparison of the subdivision of the **A** anterior midbody of the corpus callosum, **B** corticospinal tract and **C** arcuate fasciculus into 32 sections with the proposed method and BUAN. The tract profiles of the FA_{DTI} along each tract is displayed with the proposed along-tract analysis and AFQ.

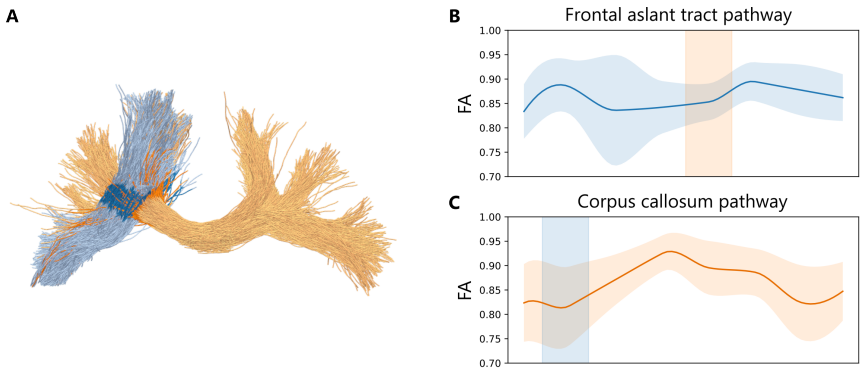

Figure 2.9: **A** Representation of the crossing between the corpus callosum (orange) and frontal aslant tract (blue). **B** Evolution of the tract-specific fractional anisotropy for each tract.

2.5 Discussion

2.5.1 A fast and conservative alternative

The proposed algorithm demonstrated a fast computation time, second only to the density thresholding heuristic. While density thresholding presents a higher computation speed, thresholding the streamlines passing through voxels with low density indiscriminately removed streamlines irrespective of the average fiber dispersion in that area. This caused a loss of U-fibers connections and changed the overall shape of the tract by removing small subbundles of shorter end points along the tract. Filtering methods should take into account the variation in density along certain portions of the pathway to not remove entire connections within the tract. Density thresholding also removed the majority of streamlines in tracts of low density, which can cause loss of the overall shape of the tract.
The proposed method preserved the original shape of the tracts, demonstrating high overlap between the tracts before and after filtering. Additionally, it had minimal impact on the distribution of streamline density, which are desirable characteristics for a conservative algorithm.

2.5.2 Along-tract analysis

The tract profiles generated using the proposed method were consistent with those obtained through AFQ, except for the lower start and end values in the AFQ estimates and a smoother profile with AFQ. The lower values at the extremities in AFQ are due to its resampling approach, which considers the first and last points of each streamline rather than the first and last sections. These points are closer to the gray matter, and therefore, exhibit lower FA values. The smoother appearance of the AFQ profile could also result from resampling into smaller sections, as each streamline is resampled and shorter streamlines contribute across the entire length of the tract profile. As a result, AFQ is more accurate when all streamlines traverse the entire tract, compared to tracts with short streamlines and multiple end points.
The main difference appeared in the estimation of the AF profile, which was irregular when using the proposed method. This irregularity is due to a lack of robustness in estimating the average pathway as the number of subdivisions increases.

Nonetheless, the byproducts of the filtering process can be used for along-tract analysis. Moreover, contrarily to TRACULA and other methods where only DTI metrics are available or metrics are limited to single-fixel models, the proposed method allows for fixel-specific analyses using the output from a wide range of multi-fixel models.

2.5.3 Limitations & future perspectives

The algorithm did not remove all streamlines that could be considered spurious in certain cases, such as in the corpus callosum example shown in Fig. 2.6. In this particular case, it was caused by several streamlines presenting a similar pathway, which prevented them from being classified as isolated by the exclusion criteria. While these streamlines could be removed by manually increasing the parameter that adjusts the required number of neighbors, adapting the default behavior of this parameter to automatically adjust based on the number of streamlines in the tract would reduce the amount of fine-tuning required.

The proposed tract segmentation into sub-sections struggled with tract displaying highly non-linear profiles as branching into several pathways is incorrectly estimated by a single average position. To solve this issue, other options to represent the mean trajectory could be investigated such as Reeb graphs, which would also allow branching in the mean pathway [78], or using multiple centroid streamline such as in QuickBundles. Another option would be to use the streamline with the highest average kernel density estimate as the centroid instead of the average position on the plane.
This could also improve the robustness of the method when the number of subsections increases, as currently increasing the number of subdivisions makes the estimation of the average pathway unstable and greatly increases the computation time.

2.6 Conclusion

The proposed method demonstrated a conservative filtering with a low computation time, making it well-suited for tracts with a high number of streamlines and tracts of low density. The absence of a template enables the exploration of lesser-known tracts or the extraction of tracts of interest based on regions obtained with other modalities, such as fMRI-activated regions. This approach holds promise for patients with abnormal brain structures or a high number of lesions, enabling tailored and patient-specific analyses of neural pathways, which is a step towards personalized medicine. Certain areas require further improvement, such as refining the removal of spurious streamlines within non-linear fascicles. Nonetheless, the algorithm should prove to be valuable for individuals seeking to filter spurious streamlines while preserving the tract morphology and to perform along-tract analyses with multi-fixel models.

Chapter III

Unraveling multi-fixel microstructure with tractography and angular weighting

Extended version of an article published as:
Delinte N, Dricot L, Macq B, Gosse C, Van Reybroeck M and Rensonnet G (2023) Unraveling multi-fixel microstructure with tractography and angular weighting. Front. Neurosci. 17:1199568. [77]

3.1 Introduction

In the field of brain research, diffusion MRI (dMRI) leveraging multi-shell sequences has emerged as an essential tool through its ability to detect changes in the microscopic and macroscopic structure of white matter which other MRI modalities are unable to capture.

At the microscopic scale, within each imaging voxel, adequate dMRI modeling estimates the orientation of axons or fascicles of axons [25, 79], and finer morphological properties, referred to as *microstructure*, such as the axon diameter, axonal density or diffusivity [80, 40]. The majority of white matter (WM) voxels contain complex crossing configurations of two or three fiber populations per voxel [81], which will be referred to in this work as *fixels*, as proposed in [82]. At the macroscopic scale, tractography algorithms piece together the orientational information collected at each voxel to generate streamlines representing the course of a bundle of axons across multiple WM voxels. Tractography is a visualization tool of great interest in clinical practice, but further processing is required for quantitative analyses.

Assigning microstructural properties to macroscopic streamlines in a consistent way remains a challenging task [83], yet it is of great interest for the study of brain structure and function, in healthy and pathological conditions [84]. It is particularly useful in population studies where the shape of WM tracts may vary significantly between patients, leading simple voxel-based comparisons to fail [85, 86]. By far the most common method to characterize WM tracts to date has been to rely on scalar maps of WM properties derived from single-fixel models such as in Diffusion Tensor Imaging (DTI) [76]. A WM tract is characterized by averaging the microstructural properties of all voxels containing streamlines of the tract, with possible refinements such as weighting by a tract probability atlas and distance from an average streamline [85]. The main limitation of this approach is its inability to interpret the microstructure in voxels where multiple fiber populations intersect [87], although such voxels are abundant at clinical imaging resolution [81, 88]. Consequently, streamlines belonging to different macroscopic tracts but passing through the same voxels are inevitably assigned the same microstructural metrics. Multi-fixel models, such as [6, 20, 21, 89], address the limitations of single-fixel models in areas of crossing fibers, but are more difficult to interpret and combine with macroscopic information, because of one-to-zero, one-to-one and one-to-many correspondence issues between local fixels and macroscopic tracts [87, 90, 91]. We identify two classes of approaches to overcome these limitations: i) microstructure-informed tractography and ii) combining tractography information with the output of multi-fixel models.

Microstructure-informed tractography has received a lot of attention in the literature. Frameworks such as MicroTrack [92], SIFT [33], SIFT2 [34], COMMIT [35], COMMIT2 [36], COMMIT-T_2 [93], COMMIT_tree [94] and MesoFT [95] use a generative signal model for each streamline, assume constant microstructure along each streamline and solve a global optimization over the whole WM to simultaneously filter streamlines and estimate their microstructural properties. These methods may be limited in the range of microstructural parameters which can be assigned to WM tracts: SIFT and SIFT2 are mainly designed to estimate fiber volume and density while COMMIT methods estimate the diameter of each streamline and may not enable the estimation of more phenomenological properties such as diffusivities. AxTract [96] relaxes the hypothesis of constant microstructure along streamlines but requires a multi-fixel model with an estimate of the axon diameter for each fixel, which is challenging with current acquisition protocols. Recently, an extension of the COMMIT framework was proposed to estimate the myelin content of crossing streamlines separately from a scalar map of voxel-wise myelin content [97].

Fewer approaches have been proposed to combine multi-fixel models with tractography. Connectivity-based fixel enhancement (CFE) [82] and a fixel-based analysis (FBA) framework [90, 86] were proposed for group comparisons of fixel-specific measures across the white matter, wherein fixel-specific metrics are smoothed only with the fixels sharing common streamlines, with a focus on axon density. However, a challenging step of this method is the creation of a group-averaged template of fiber Orientation Distribution Functions (fODFs). This may introduce distortions, artifacts or excessive smoothing when the brain morphology presents abnormalities. Furthermore, a streamline segment in a voxel is only assigned the metrics of the fixel with the closest orientation, which does not allow multiple local fixels to contribute to a given streamline. This "closest-fixel-only" strategy was also used in [16, 21, 91] when analyzing the microstructural properties of macrostructural WM tracts using a multi-fixel model.

This work focuses on the latter class of approaches, i.e., the combination of multi-fixel models and tractography, and introduces a framework named UNRAVEL. The only inputs required for our framework are any choice of multi-fixel microstructural model and a set of streamlines specific to a macroscopic tract of interest, which can be generated by any tractography algorithm and isolated with any method [37]. The streamlines can be generated independently and do not need to match the orientations of the fixels in the microstructural model. We propose a lightweight framework relating stream-

line segments to local fixels, which includes the closest-fixel-only and a proposed *angular weighting* strategy among various options. Our framework also allows microstructural properties to vary along the course of an individual streamline. We provide theoretical interpretations at the tract and at the streamline segment level, which enables UNRAVEL to estimate the microstructure at the streamline level as well as mean microstructural values for a whole tract. We validate the method on a synthetic phantom, on a scan-rescan experiment on a healthy adult, as well as on a small population of children with dyslexia and control children.

3.2 Theory

The UNRAVEL framework requires two inputs for each subject, schematically illustrated in Fig. 3.1. First, an estimation of a K-fixel model in every voxel v of the WM, in which every fixel k is characterized by a principal orientation $\hat{\mathbf{u}}_{vk}^{\mu}$ and fixel-specific microstructural metrics M_{vk}^{μ}, $k = 1, \ldots, K$, where typically $K = 2$ or 3. Second, a macroscopic tract $\mathcal{T}$, defined as a set of streamlines, based on anatomical or functional relevance. Each streamline $\mathcal{L}$ is composed of small, straight segments s, with a length equal to the step size parameter in the tractography.

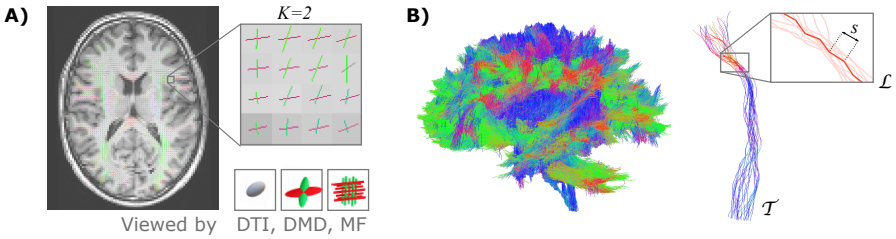

Figure 3.1: The proposed UNRAVEL framework requires two independent inputs: a multi-fixel microstructural model estimated in the white matter and the streamlines of a given macroscopic tract of interest. A 2D slice of a volume with up to K fixels in each voxel obtained with a multi-fixel model (such as DIAMOND [DMD] and Microstructure Fingerprinting [MF]), with each fixel possessing a main orientation (shown as colored sticks) and different microstructural properties. **B** Illustration of a macroscopic tract $\mathcal{T}$, composed of streamlines $\mathcal{L}$ made of segments s. In this illustration, tract $\mathcal{T}$ was isolated from a set of whole-brain tractography streamlines.

3.2.1 The UNRAVEL framework

The main concept behind UNRAVEL is to treat each streamline segment s of a macroscopic tract $\mathcal{T}$ individually and assign each segment microstructural properties in each voxel v based on the fixels in that voxel. The key quantity to achieve this is defined below.

Relative contribution of a fixel to a streamline segment

The relative contribution of fixel k to a streamline segment s in voxel v is denoted α_{vsk} and must satisfy

$$\begin{aligned} &\alpha_{vsk} \in [0, 1] \\ &\sum_{k=1}^{K} \alpha_{vsk} = 1 \quad \forall\, v, s. \end{aligned} \tag{3.1}$$

Streamline segments crossing voxels boundaries are divided into smaller subsegments, each of which is enclosed within a single voxel and is then processed individually. Four definitions are considered below, referred to as relative volume weighting, closest-fixel-only and angular weighting. In contrast to the relative volume weighting approach, which is independent of the angle between the segment s and the fixel k, closest-fixel-only and angular weighting are determined by the angular difference between the two.

Relative volume weighting (*vol*) This method attributes a relative contribution using the relative volume fraction of each fixel in a voxel v

$$\alpha_{vsk} = \frac{f_{vk}}{\sum_k f_{vk}}, \tag{3.2}$$

where f_{vk} is the volume fraction of fixel k estimated by the multi-fixel model. The resulting relative contribution is not dependent on s. In the absence of an isotropic compartment, this equation can be simplified to $\alpha_{vsk} = f_{vk}$ as the volume fraction of each fixel sum to one, as in [98].

Closest-fixel-only (*cfo*) A segment receives a contribution from a single fixel in the voxel, based on the angular distance. The fixel k with orientation $\hat{\mathbf{u}}_{vk}^{\mu}$ closest to the orientation $\hat{\mathbf{u}}_{vs}$ of a streamline segment s in voxel v gives its properties to segment s while the other fixels do not contribute. This is the most commonly used strategy in methods combining microstructure and

tractography such as MicroTrack [92], CFE [82] and Magic DIAMOND [91]. Mathematically, for $k = 1, \dots, K$,

$$\alpha_{vsk} = \begin{cases} 1 & \text{if } k = \arg\min_{k'} \angle \hat{\mathbf{u}}_{vs}, \hat{\mathbf{u}}^{\mu}_{vk'} \\ 0 & \text{elsewhere,} \end{cases} \tag{3.3}$$

where $\angle \mathbf{a}, \mathbf{b}$ denotes the angle between vectors $\mathbf{a}$ and $\mathbf{b}$.

Angular weighting (*ang*) A relative contribution α_{vsk} is assigned to all fixels k in a voxel v based on the relative angle difference between the fixels and the orientation of the streamline segment s. The closer a fiber population orientation is to the orientation of the segment, the closer α_{vsk} is to 1 and the more this fixel contributes to the microstructural properties assigned to s. Mathematically, for $k = 1, \dots, K$,

$$\alpha_{vsk} = \begin{cases} \frac{\sum_{k'=1}^{K} \angle \hat{\mathbf{u}}_{vs}, \hat{\mathbf{u}}^{\mu}_{vk'} - \angle \hat{\mathbf{u}}_{vs}, \hat{\mathbf{u}}^{\mu}_{vk}}{(K-1) \cdot \sum_{k'=1}^{K} \angle \hat{\mathbf{u}}_{vs}, \hat{\mathbf{u}}^{\mu}_{vk'}} & \text{for } K > 1, \\ 1 & \text{for } K = 1. \end{cases} \tag{3.4}$$

This definition is expected to be useful in tracts $\mathcal{T}$ in which axons exhibit microscopic dispersion [99, 100] where multiple fixels may be required to explain the signal. It also captures the stochastic nature of the streamline segment orientation in probabilistic tractography.
While Eq. (3.4) has the expected behavior when K=2, increasing the number of fixels decreases the weight attributed to a perfectly aligned fixel. This equation can be re-formulated avoid reducing the weight of a perfectly aligned fixel when K>2,

$$\alpha_{vsk} = \begin{cases} \frac{\prod_{k'=1, k' \neq k}^{K} \angle \hat{\mathbf{u}}_{vs}, \hat{\mathbf{u}}^{\mu}_{vk'}}{\sum_{k''=1}^{K} \prod_{k'=1, k' \neq k''}^{K} \angle \hat{\mathbf{u}}_{vs}, \hat{\mathbf{u}}^{\mu}_{vk'}} & \text{for } K > 1, \\ 1 & \text{for } K = 1. \end{cases} \tag{3.5}$$

Relative angular weighting (*raw*) Decreases the weights of fixels orthogonal to the streamline segment s

$$\begin{aligned} \phi &= \min(90, \sum_{k'=1}^{K} \angle \hat{\mathbf{u}}_{vs}, \hat{\mathbf{u}}^{\mu}_{vk'}) \\ \alpha_{vsk} &= \begin{cases} \frac{\phi - \angle \hat{\mathbf{u}}_{vs}, \hat{\mathbf{u}}^{\mu}_{vk}}{\phi \cdot K - \sum_{k'=1}^{K} \angle \hat{\mathbf{u}}_{vs}, \hat{\mathbf{u}}^{\mu}_{vk'}} & \text{for } K > 1, \\ 1 & \text{for } K = 1. \end{cases} \end{aligned} \tag{3.6}$$

This definition is expected to be useful in tracts $\mathcal{T}$ in which axons exhibit microscopic dispersion [99, 100] where multiple fixels may be required to explain the signal. It also captures the stochastic nature of the streamline segment orientation in probabilistic tractography. Following the changes made in Eq. (3.5), Eq. (3.6) can be rewritten as

$$\alpha_{vsk} = \begin{cases} \frac{\prod_{k'=1,k'\neq k}^{K} \angle \hat{\mathbf{u}}_{vs}, \hat{\mathbf{u}}^{\mu}_{vk'}}{\sum_{k''}^{K} \prod_{k'=1,k'\neq k''}^{K} \angle \hat{\mathbf{u}}_{vs}, \hat{\mathbf{u}}^{\mu}_{vk'}} \cdot \frac{90 - \angle \hat{\mathbf{u}}_{vs}, \hat{\mathbf{u}}^{\mu}_{vk}}{90 \cdot K - \sum_{k'=1}^{K} \angle \hat{\mathbf{u}}_{vs}, \hat{\mathbf{u}}^{\mu}_{vk'}} & \text{for } K > 1, \\ 1 & \text{for } K = 1. \end{cases}$$

Figure 3.2 graphically compares the above definitions of α_{vsk} in a case with $K = 2$ fixels in a voxel. With these definitions, streamline- and tract-specific maps and metrics can now be defined.

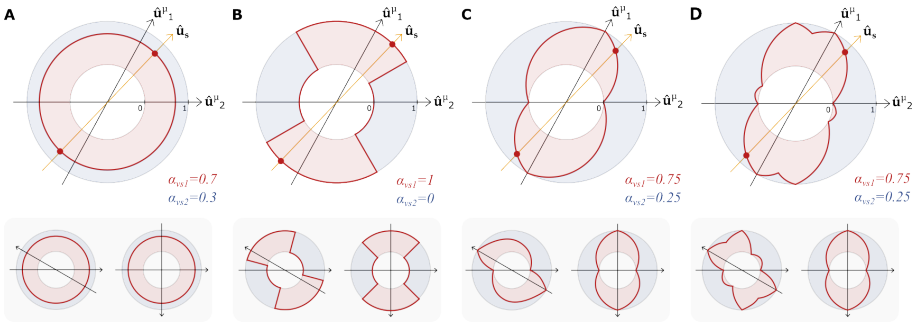

Figure 3.2: Angular weighting attributes a relative weight to all fixels based on the angle difference. Graphical representation of the orientations $\hat{\mathbf{u}}^{\mu}_1$ and $\hat{\mathbf{u}}^{\mu}_2$ of two fixels and a segment s of a streamline $\mathcal{L}$ (orange) in a voxel v and the relative contribution α_{vsk} of fixel 1 ($k = 1$, red) and fixel 2 ($k = 2$, blue) with **A** relative volume weighting, **B** closest-fixel-only, **C** angular weighting and **D** relative angular weighting strategies as a function of the orientation $\hat{\mathbf{u}}_s$ of the streamline segment in the voxel. Each weighting strategy is also represented with an angle difference of 150° (left) and 270° (right).

Streamline microstructure

For all segments s of a given streamline, the segment-specific microstructural metric M_{vs} is defined in voxel v as

$$M_{vs} = \sum_{k=1}^{K} \alpha_{vsk} M^{\mu}_{vk}. \tag{3.7}$$

This value varies with s, which allows a streamline to have non-constant microstructure along its course.

Fixel weight maps

We first define the segment-specific fixel weight w_{vsk} as

$$w_{vsk} = \alpha_{vsk} l_{vs},$$

where l_{vs} is the length of segment s, restricted to voxel v if segment s spans multiple voxels. For each fixel k, a fixel weight map $w_{vk}^{\mathcal{T}}$ of the streamline segments s in tract $\mathcal{T}$ is then defined as

$$w_{vk}^{\mathcal{T}} = \sum_s w_{vsk} = \sum_s \alpha_{vsk} l_{vs}. \tag{3.8}$$

Such a map shows in each voxel v the importance of fixel k in assigning microstructural properties to the segments of tract $\mathcal{T}$, with higher weight associated to longer and more numerous streamline segments in that voxel and to higher relative contribution α_{vsk} of fixel k. Note that this map does *not* exhibit spatial smoothness in general because the k-th fixel of one voxel may not correspond to the same macroscopic tract $\mathcal{T}$ as the k-th fixel in neighboring voxels.

Finally, the summation of Eq. (3.8) over k gives the map of total segment lengths $w_v^{\mathcal{T}}$ in each voxel (using Eq. (3.1) for the last equality)

$$w_v^{\mathcal{T}} = \sum_{k=1}^{K} w_{vk}^{\mathcal{T}} = \sum_{k=1}^{K} \sum_s \alpha_{vsk} l_{vs} = \sum_s l_{vs}, \tag{3.9}$$

which does not depend on the fixels' microstructural properties and is entirely determined by the tractography. This map will generally exhibit spatial smoothness and can be interpreted as the probability of the presence of tract $\mathcal{T}$.

Microstructure maps

Summing the fixel-specific microstructural metrics M_{vk}^{μ} provided as input to our method weighted by the above-defined fixel weight maps produces the following map

$$M_v^{\mathcal{T}} = \frac{\sum_{k=1}^{K} w_{vk}^{\mathcal{T}} M_{vk}^{\mu}}{\sum_{k=1}^{K} w_{vk}^{\mathcal{T}}}, \tag{3.10}$$

which gives an average microstructural metric in each voxel v representing all the streamlines of tract $\mathcal{T}$. This map exhibits more spatial smoothness and facilitates visualization of tract microstructure. The confidence level of its values can be guided by the segment lengths map defined in Eq. (3.9) above.

Mean tract microstructural metric

An overall scalar summary $\bar{M}^{\mathcal{T}}$ of a specific microstructural metric M^{μ} for tract $\mathcal{T}$ can be defined using Eq. (3.10) and a weighted map $\gamma_v^{\mathcal{T}}$, specifying the respective weights of each voxels for the mean value

$$\bar{M}^{\mathcal{T}} = \frac{\sum_v \gamma_v^{\mathcal{T}} M_v^{\mathcal{T}}}{\sum_v \gamma_v^{\mathcal{T}}}. \tag{3.11}$$

Two definitions of weighted map $\gamma_v^{\mathcal{T}}$ are considered below, referred to as total segment length and region of interest weighting.

Total segment length weighting (*tsl*) A first weighted map can be defined using the total segment length $w_v^{\mathcal{T}}$ defined in Eq. (3.9), where voxels with a high fixel weight contribute more to the final metric.

$$\gamma_v^{\mathcal{T}} = w_v^{\mathcal{T}}. \tag{3.12}$$

Region of interest weighting (*roi*) Another weighted map can be defined by attributing equal weights to all voxels v contained in the tract.

$$\gamma_v^{\mathcal{T}} = \begin{cases} 1 & \forall\, v \in \mathcal{T} \\ 0 & \text{elsewhere.} \end{cases} \tag{3.13}$$

3.2.2 Interpretation at the segment level

Equation (3.10) can be rewritten as (see details in Appendix B)

$$\begin{aligned} M_v^{\mathcal{T}} &= \frac{\sum_{k=1}^{K} w_{vk}^{\mathcal{T}} M_{vk}^{\mu}}{\sum_{k=1}^{K} w_{vk}^{\mathcal{T}}} \\ &= \frac{\sum_s l_{vs} M_{vs}}{\sum_s l_{vs}}, \end{aligned} \tag{3.14}$$

which states that the tract-specific map in a voxel v results from the contributions of all streamline segments in a specific voxel. Each segment contributes its segment-specific microstructural metric $M_{vs}^{\mathcal{T}}$ defined in Eq. (3.7), weighted by its intra-voxel length l_{vs}. The quantity is normalized by the total segment length in that voxel.

Similarly, Eq. (3.11) using Eq. (3.12) can be rewritten as (see Appendix B)

$$\begin{aligned} \bar{M}^{\mathcal{T}} &= \frac{\sum_v \gamma_v^{\mathcal{T}} M_v^{\mathcal{T}}}{\sum_v \gamma_v^{\mathcal{T}}} \\ &= \frac{\sum_v \sum_s l_{vs} M_{vs}}{\sum_v \sum_s l_{vs}}, \end{aligned}$$

where the interpretation is similar to the tract-specific microstructure map $M_v^{\mathcal{T}}$ above, except for the contributions which are from all segments over all the voxels containing streamlines of tract $\mathcal{T}$.

3.3 Materials and methods

3.3.1 Datasets

Our proposed framework and angular weighting strategy were validated using three datasets: a synthetic phantom, a scan and rescan on a healthy adult volunteer and cohorts of dyslexic children and control children. The synthetic phantom provided a comparison of the different approaches to a known ground truth. The scan and rescan enabled an analysis of the variability and reproducibility of the results. Lastly, the dyslexic cohort served as proof of concept that our framework could be applied to clinical populations.

Experiment I: Synthetic phantom

A synthetic phantom based on Monte Carlo simulations of the dMRI signal [101, 102, 103] was created to compare the microstructural metrics obtained to a known ground truth. The dMRI protocol used for the phantom matched as closely as possible the protocol used in the *in vivo* acquisitions described below. Axons were modeled as straight, randomly packed cylinders with diameters drawn from a gamma distribution with mean and variance fixed to 1 μm and 0.6 μm respectively [102]. The cylinder packing density was interpreted as a fiber volume fraction (FVF). Intra-axonal diffusivity was fixed to 2 $\mu m^2/ms$ [104]. As visible in Fig. 3.4, the phantom was a 2D slice containing four tracts: two horizontal and two vertical tracts. The top and bottom tracts had a FVF of 0.70 and 0.66, respectively, while the vertical tracts had an increasing FVF from top to bottom. All voxels had an extracellular diffusivity $D_{\text{ex}} = 1\ \mu m^2/ms$. Each vertical tract crossed both horizontal tracts over multiple voxels. Regions of isotropic diffusion representing cerebrospinal fluid (CSF) were also included.

Experiment II: Scan & rescan

A healthy adult participant underwent two consecutive dMRI scans to study the variability in the outputs of our method. The scans were performed on a 3T GE SIGNA Premier scanner (GE Healthcare, Chicago, IL) with the following parameters: TR = 4842 ms, TE = 77 ms, 2 mm isotropic voxels, in-plane

FOV: 220x220 mm^2, Δ = 35.7 ms, δ = 22.9 ms, 64 gradients at b = 1000, 32 at b = 2000,3000,5000 s/mm^2, corresponding to diffusion gradient intensities up to 68.9 mT/m, and 7 interspersed b0 images. Preprocessing included thermal denoising [55], Gibbs ringing correction [56], eddy-current distortion and movement correction [57]. The movement correction procedure provided variables representing the relative movement of the patient during the scan time [105]. The total relative motion, representing the average voxel displacement across all voxels with respect to the previous volume, for all volumes, was selected as a summary measure X_{mov} of the patient's movement. A 3D T1 image (TE = 2.96ms, TR = 2188.16ms, TI = 900ms, 156 slices, 1mm isotropic, in-plane FOV: 256x256mm^2) was also acquired with each scan. Registration to the Desikan-Killiany atlas [60] was accomplished using the *FreeSurfer*[1] function `recon-all`, with an additional parcellation of the brainstem. Differences in all tract-specific metrics were computed between the scan and the rescan in 38 major white matter pathways (see methodological details in Section 3.3.2).

Experiment III: Dyslexia study

The study consisted of 16 children with dyslexia, a reading and spelling disorder, and 18 healthy controls in the same age range (9.5 ± 1 years old). The experiment was carried out in accordance with the ethical standards of the Declaration of Helsinki and received approval by the Ethics Committee of the University Hospital of Saint-Luc (number: B403201942022). All participants underwent a dMRI sequence with the same parameters as in Experiment II above. The registration also used the *FreeSurfer* parcellation. Two macroscopic WM tracts of interest were selected to compare the two populations: the right arcuate fasciculus (AF) and the right superior longitudinal fasciculus II (SLFII). These tracts were selected for their involvement in the language-related pathways and, potentially, dyslexia [106, 107, 108, 109]. For each average microstructural metric M in each tract and for each of the analysis methods described below, the following regression model was estimated

$$M = \beta_0 + \beta_{\text{dys}} \cdot X_{\text{dys}} + \beta_{\text{mov}} \cdot X_{\text{mov}},$$

where $X_{\text{dys}} \in \{0, 1\}$ encodes the participant's group and X_{mov} is the aggregate movement metric computed with FSL's motion correction routine [105]. Estimates and p-values of β_{dys} were reported to assess the difference between the two populations attributed to dyslexia after correcting for movement during the acquisition.

[1] `https://surfer.nmr.mgh.harvard.edu/`

3.3.2 Data processing and analysis

Four types of estimates for a microstructural property M were obtained following the pipeline depicted in Fig. 3.3, described in more detail in the following paragraphs.

Microstructural diffusion models

As shown in the second row of Fig. 3.3, either a single- or a multi-fixel model was estimated at this stage. DTI [76] was selected as the single-fixel model while DIAMOND (DMD) [20] and Microstructure Fingerprinting (MF) [21] served as multi-fixel models. DTI and DIAMOND provided tensor-derived metrics such as the fractional anisotropy (FA) while MF estimated the fiber volume fraction (FVF) of each fixel. An isotropic signal contribution was allowed for the multi-fixel models.

Macroscopic tractography analysis

This stage (second row, right in Fig. 3.3) consisted in generating tractography streamlines specific to a tract of interest $\mathcal{T}$. In our experiments, tractography of the WM was performed using a probabilistic algorithm based on the Constrained Spherical Deconvolution (CSD) model [25] to produce a whole-brain tractogram [54]. However, the UNRAVEL framework does not constrain the choice of tractography algorithm. In the phantom of Experiment I, the seeds and target regions were placed at the start and end of each tract. In the *in vivo* Experiments II and III, the seeds were placed inside of a T1-based white matter mask with a density of 8 seeds per voxel. The other selected parameters were: a step size of 1 mm, a stopping criterion of 0.35 on the generalized anisotropy and a maximum angle of 15° between streamline segments. The WM tracts of interest were extracted from the whole brain tractography using White Matter Query Language (WMQL) [37][2].

[2]The WMQL queries used are available on the GitHub page of our project at `https://github.com/DelinteNicolas/UNRAVEL`

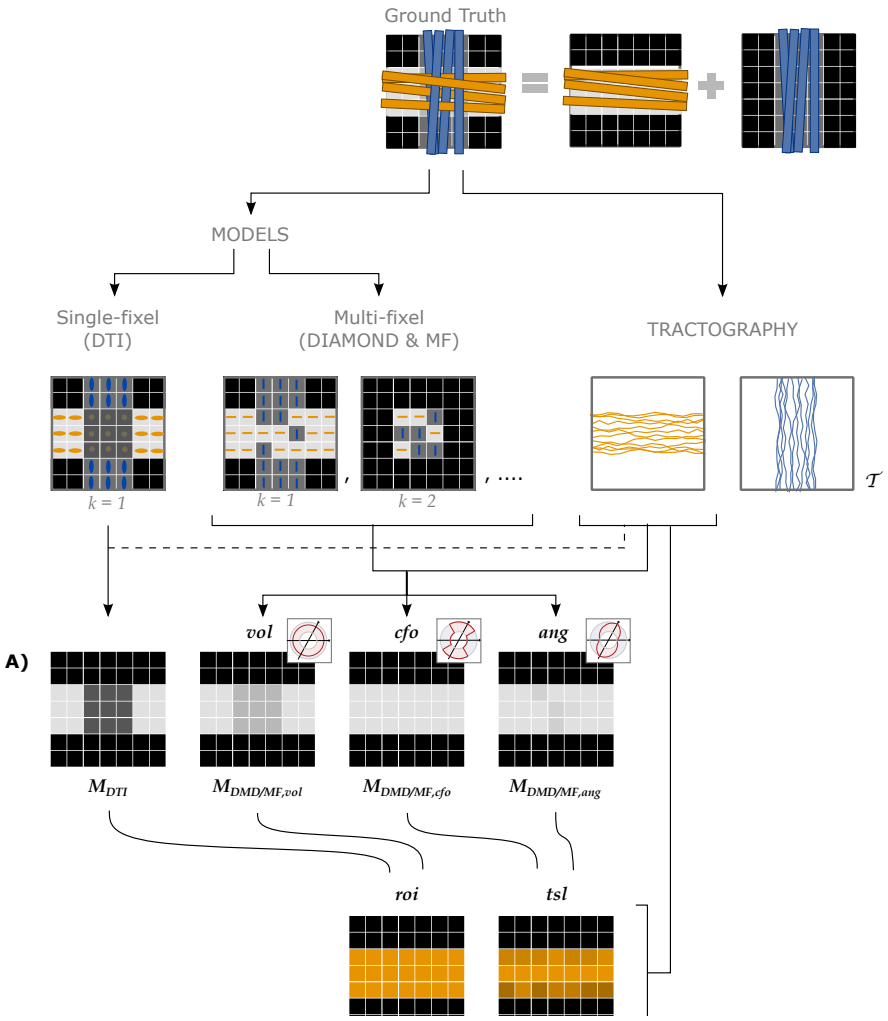

Figure 3.3: Different approaches to attribute microstructural properties to macroscopic tracts with our proposed UNRAVEL framework. The ground truth (top row) schematically depicts crossing fascicles of axons (not to scale). The grayscale maps in the background show the value of a tract-specific microstructural metric M. Either a single- or a multi-fixel model (with $K = 2$ in our example) is estimated (second row). Note that a multi-fixel model does not guarantee a consistent separation of fixels in regions of crossings. The outputs of the proposed method are: **A** Microstructure maps (Eq. (3.10)), created for each tract $\mathcal{T}$ using a relative contribution defined by either *vol*, *cfo* or *ang*. **B** The maps are then averaged as a single value (Eq. (3.11)) with the *roi* or *tsl* option.

Microstructure maps and scalars

The final stages consisted in computing maps (Fig. 3.3A) and averages (Fig. 3.3B) of the metrics of the tracts of interest. For ease of notation, we denote the microstructure map of a tract $\mathcal{T}$ for a metric M from a model (either DTI, DMD or MF) as

$$M^{\mathcal{T}}_{\text{MODEL},\mathcal{A}},$$

where $\mathcal{A} \in \{cfo, ang, vol\}$ specifies the strategy used to define the relative contribution α_{vsk} of a fixel to a streamline segment, as defined in Section 3.2.1. Similarly, the mean of the microstructure map is written as

$$\bar{M}^{\mathcal{T}}_{\text{MODEL},\mathcal{A},C},$$

where $C \in \{tsl, roi\}$ specifies the tract-averaging strategy $\gamma_v^{\mathcal{T}}$ selected as defined in Section 3.2.1.

Although all combinations of $\mathcal{A}$ and C are compatible, four cases were selected to showcase the currently available options and the variety of analysis possible with the UNRAVEL framework, and to serve as a baseline to compare our proposed angular weighting strategy (Fig. 3.3). The commonly used ROI-based single-fixel analysis was represented by the DTI model with region of interest weighting (*roi*). A similar heuristic approach is developed using multi-fixel output with a relative volume and region of interest weighting (*vol,roi*), where the streamline orientation and density do not have an effect on the final estimate. In contrast, the last two approaches, corresponding to either closest-fixel-only or angular weighting combined with total segment length weighting (*cfo/ang,tsl*), are highly impacted by the tractography with the influence of streamline orientation and density on the estimated mean metric. The closest-fixel-only (*cfo*) strategy is commonly used when assigning multi-fixel microstructural properties to streamlines [82, 21, 91] and serves as a baseline for the proposed angular weighting (*ang*) approach.

For all three experiments, we reported estimates of the FA obtained with the four approaches using the FA from DTI and the FA of the diffusion tensors found by DIAMOND (DMD) and named $FA^{\mathcal{T}}_{\text{DTI}}$, $FA^{\mathcal{T}}_{\text{DMD},vol}$, $FA^{\mathcal{T}}_{\text{DMD},cfo}$ and $FA^{\mathcal{T}}_{\text{DMD},ang}$. Metrics obtained with DTI do not specify the α_{vsk} used since all three definitions attribute all the weight to the only fixel present. The FVF was only obtained with the last three approaches, corresponding to $FVF^{\mathcal{T}}_{\text{MF},vol}$, $FVF^{\mathcal{T}}_{\text{MF},cfo}$ and $FVF^{\mathcal{T}}_{\text{MF},ang}$, since this variable was only available with MF.

3.4 Results

3.4.1 Experiment I: Synthetic phantom

Figure 3.4 reports the tract-specific FA and FVF maps found with the different approaches as well as the means, medians, and interquartile ranges for each tract. With the single-fascicle model, FA_{DTI} presented a noticeable decrease in areas of crossing fibers between the horizontal and vertical tracts. The variation along all tracts was high, with FA_{DTI} ranging from 0.55 to 0.97 in tracts $\mathcal{T}_1$ and $\mathcal{T}_2$ where the ground truth value did not vary along the tract. The mean $\bar{FA}_{\mathrm{DTI},roi}$ in all three tracts was lower than the minimum value in the ground truth. With a multi-fixel model and relative volume weighting, the $FA_{\mathrm{DMD},vol}$ values were closer to the ground truth than the traditional FA_{DTI} in all tracts, especially in areas of crossing fascicles. The values still underestimated the ground truth except in tract $\mathcal{T}_3$ where the median of the $FA_{\mathrm{DMD},vol}$ estimates exceeded the highest value in the ground truth. The closest-fixel-only approach displayed less variation than FA_{DTI} and $FA_{\mathrm{DMD},vol}$, but overestimated the $FA_{\mathrm{DMD},cfo}$ values. Our proposed $FA_{\mathrm{DMD},ang}$ values also displayed less variation than FA_{DTI} and $FA_{\mathrm{DMD},vol}$ but was closer to the ground truth than $FA_{\mathrm{DMD},cfo}$. Estimates of $FVF_{\mathrm{MF},cfo}$ and $FVF_{\mathrm{MF},ang}$ were similar and presented less variation compared to $FVF_{\mathrm{MF},vol}$, except for tract $\mathcal{T}_2$ where $FVF_{\mathrm{MF},ang}$ exhibited a larger variation. The values of the $FA_{\mathrm{DMD},ang}$ and $FVF_{\mathrm{MF},ang}$ microstructure maps displayed in Fig. 3.4 should be interpreted with caution along the edges of the tracts as a low number of streamline segments were contained in those voxels.

The differences between closest-fixel-only and angular weighting were investigated in Fig. 3.5, which shows the evolution of the segment-specific microstructural metrics FA, from DIAMOND, and FVF, from MF, assigned to each segment of a single streamline isolated from tract $\mathcal{T}_3$, as defined by Eq. (3.7), using relative volume weighting (Eq. (3.2)), closest-fixel-only (Eq. (3.3)) and angular weighting (Eq. (3.4)). In Fig. 3.5B, DIAMOND incorrectly detected two different fixels in the voxels of the upper part of tract $\mathcal{T}_3$ whereas the ground truth only contained one fixel. The erroneous fixel most aligned with the streamline exhibited a FA greater than the ground truth, while the other presented a lower FA. This led to an overestimation of the streamline-specific $FA_{\mathrm{DMD},cfo}$, whereas there was either less or no impact on $FA_{\mathrm{DMD},ang}$, which enables multiple fixels to contribute to a streamline segment. In Fig. 3.5C, with the orientations used by MF, the closest-fixel-only and angular weighting strategies yielded similar estimates of the streamline-specific FVF_{MF}, which gradually decreased from the lower to the upper part of the isolated streamline.

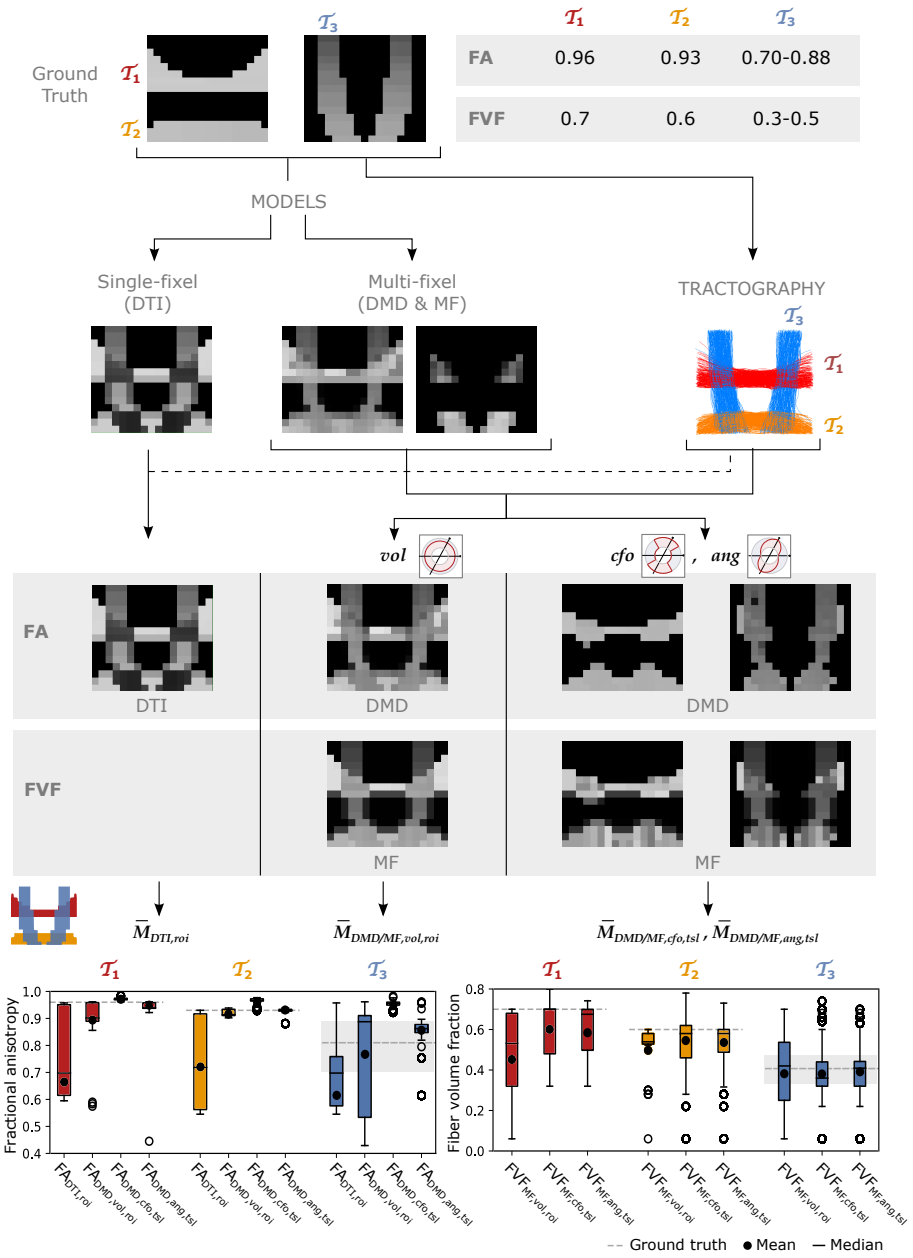

Figure 3.4: The UNRAVEL framework enables more accurate estimation of the tract-specific microstructure, less impacted by tract crossings. Two horizontal tracts $\mathcal{T}_1$ and $\mathcal{T}_2$ with a high FA and FVF are crossed by vertical tracts $\mathcal{T}_3$ with lower FA and FVF. Tract-specific microstructure maps, defined by Eq. (3.10), are shown for the microstructural metrics FA and FVF. Bottom row: the mean (circle), median (dash) and interquartile range (boxes) of FA and FVF values found for each tract are displayed, the average ground truth value is indicated by a continuous gray line while the minimum and maximum values are shown by dashed gray lines.

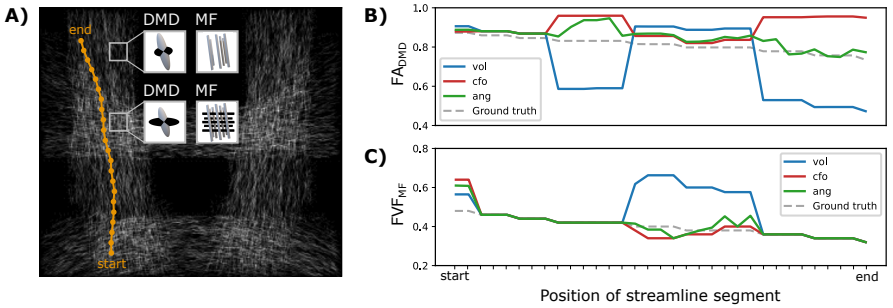

Figure 3.5: Angular-weighted relative fixel contribution robustly captures varying microstructure along the course of a single streamline. **A** A single streamline was isolated (in orange) and all its segments were investigated. The local multi-fixel models were **B** DIAMOND (DMD) and **C** Microstructure Fingerprinting (MF), each leading to different fixel orientations in each voxel. The DMD model incorrectly estimated two populations in the top half of the vertical tracts. The **B** FA or **C** FVF values attributed to the streamline segments were computed from the FA or FVF of the multiple fixels in the voxel, following Eq. (3.7). For both **B** and **C**, the values were estimated using the relative volume weighting approach (Eq. (3.2), in blue), closest-fixel-only approach (Eq. (3.3), in red) and the angular weighting approach (Eq. (3.4), in green).

3.4.2 Experiment II: Scan & rescan

Bland-Altman plots for the tract-wide means $\bar{FA}_{\text{DTI},roi}$ (Fig. 3.6A), $\bar{FA}_{\text{DMD},vol,roi}$ (Fig. 3.6B), $\bar{FA}_{\text{DMD},cfo,tsl}$ (Fig. 3.6C) and our proposed average $\bar{FA}_{\text{DMD},ang,tsl}$ (Fig. 3.6D) defined by Eq. (3.11) for each of the 38 selected tracts suggest smaller changes between the scan and the rescan for $\bar{FA}_{\text{DMD},vol,roi}$, $\bar{FA}_{\text{DMD},cfo,tsl}$ and the proposed $\bar{FA}_{\text{DMD},ang,tsl}$ than for $\bar{FA}_{\text{DTI},roi}$ across the 38 WM regions. Tracts with a higher mean FA showed less variation between the two scans across all approaches. The mean percentage change of $\bar{FA}_{\text{DMD},ang,tsl}$ was closer to zero compared to $\bar{FA}_{\text{DMD},vol,roi}$ and $\bar{FA}_{\text{DMD},cfo,tsl}$. The tract-wide means were higher for $\bar{FA}_{\text{DMD},cfo,tsl}$ and $\bar{FA}_{\text{DMD},ang,tsl}$ than for $\bar{FA}_{\text{DMD},vol,roi}$, all being considerably higher than the traditional $\bar{FA}_{\text{DTI},roi}$.

Similarly to Experiment I, the evolution of the microstructural properties along the path of a single streamline can be obtained with *in vivo* tracts. Figure 3.7 displays the relative contribution α_{vsk} using angular weighting (Eq. (3.4)) as well as the associated metrics $FA_{\text{DMD},ang}$ and $FVF_{\text{MF},ang}$ for an isolated streamline passing through the corpus callosum. The neural fibers in the middle of the pathway, linking the left and right hemispheres, presented a

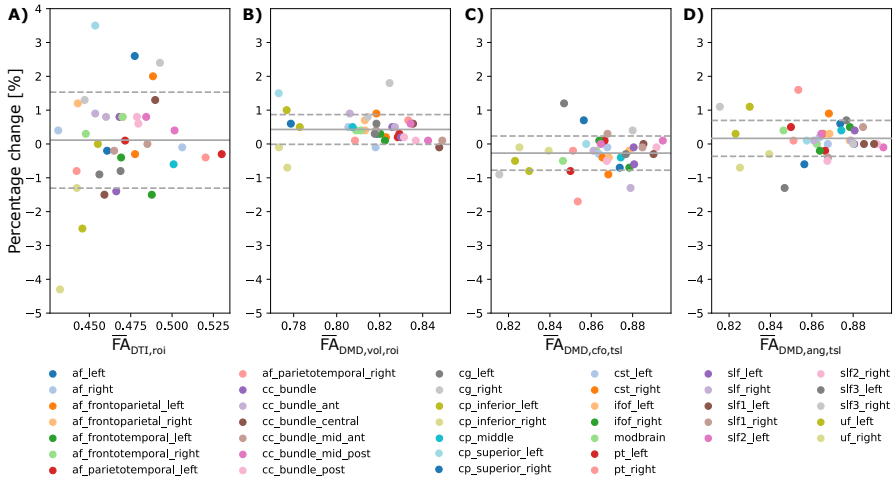

Figure 3.6: Multi-fixel metrics combined with angular weighting shows smaller variability compared to single-fixel metrics and smaller mean bias compared to relative fraction weighting in a scan/rescan experiment. Bland-Altman plots of the percentage change between the scan and the rescan of respectively **A** $\bar{FA}_{\text{DTI},roi}$ (Mean=0.11;SD=1.4), **B** $\bar{FA}_{\text{DMD},vol,roi}$ (Mean=0.43;SD=0.44, **C** $\bar{FA}_{\text{DMD},cfo,tsl}$ (Mean=-0.27;SD=0.51) and **D** the proposed $\bar{FA}_{\text{DMD},ang,tsl}$ (Mean=0.17;SD=0.53) from Eq. (3.11) across the 38 considered WM tracts.

high $FA_{\text{DMD},ang}$ and $FVF_{\text{MF},ang}$, were well aligned and accurately represented by a single fiber population. The end and start of the pathway displayed lower $FA_{\text{DMD},ang}$ and $FVF_{\text{MF},ang}$ with smaller relative contributions and weights.

3.4.3 Experiment III: Dyslexia study

The distributions of tract-wide microstructural means for the dyslexic and control populations are shown in Fig. 3.8. The distribution of tract-wide mean FA values ($\bar{FA}_{\text{DTI,roi}}$, $\bar{FA}_{\text{DMD},vol,roi}$, $\bar{FA}_{\text{DMD},cfo,tsl}$, $\bar{FA}_{\text{DMD},ang,tsl}$) in each group showed the same behavior, with $\bar{FA}_{\text{DMD},cfo,tsl}$ and the proposed $\bar{FA}_{\text{DMD},ang,tsl}$ having the highest values, followed by $\bar{FA}_{\text{DMD},vol,roi}$ and then by $\bar{FA}_{\text{DTI,roi}}$. The same ordering was observed for $\bar{FVF}_{\text{MF},cfo,tsl}$, $\bar{FVF}_{\text{MF},ang,tsl}$ and $\bar{FVF}_{\text{MF},vol,roi}$. The mean of the distribution of tract-wide mean FA and FVF was lower in the dyslexic population compared to healthy controls in all cases. Two p-values were below 0.05 when comparing the two groups, $\bar{FVF}_{\text{MF},cfo,tsl}$ and $\bar{FVF}_{\text{MF},ang,tsl}$ in the right SLFII. No statistically significant differences were found using the apparent fiber density (AFD) metric from the FBA framework.

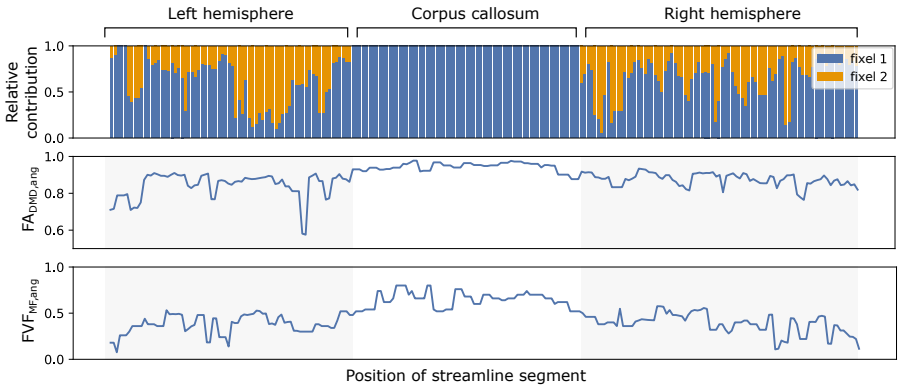

Figure 3.7: The microstructure along a streamline follows macrostructural changes through brain regions with different neural fiber configurations. The evolution of the relative contributions α_{vsk} of two fixels (in blue and orange) for a single callosal streamline along its path (top). Segment-specific FA_{vs} (middle) and FVF_{vs} (bottom) values computed with the UNRAVEL framework using Eq. (3.7).

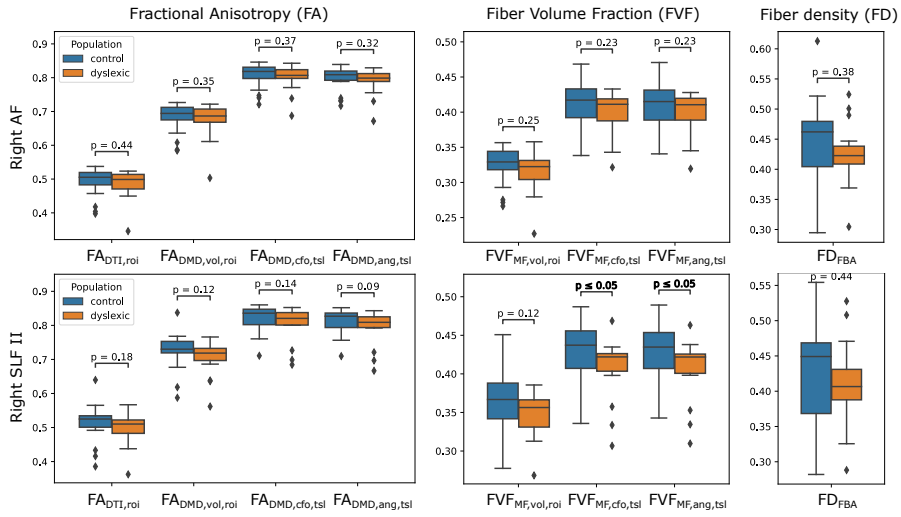

Figure 3.8: Estimates of FA and FVF obtained with the UNRAVEL framework suggest values are slightly lower in children with dyslexia compared to controls. Boxplots of the tract-wide mean of the fractional anisotropy ($\bar{FA}_{\text{DTI}}$,$\bar{FA}_{\text{DMD},vol}$,$\bar{FA}_{\text{DMD},cfo,tsl}$,$\bar{FA}_{\text{DMD},ang,tsl}$), fiber volume fraction ($\bar{FVF}_{\text{MF},vol}$, $\bar{FVF}_{\text{MF},cfo,tsl}$, $\bar{FVF}_{\text{MF},ang,tsl}$) and the mean of the fiber density maps obtained with the FBA pipeline AFD_{FBA} for the dyslexic (orange) and control (blue) cohort in the right arcuate fasciculus (AF, top) and the right superior longitudinal fasciculus II (SLFII, bottom).

Figure 3.9 displays maps of FA_{DTI}, $FA_{\text{DMD},vol}$, $FA_{\text{DMD},cfo}$ and $FA_{\text{DMD},ang}$ on a slice of the AF in a control participant. The traditional FA_{DTI} values obtained with DTI are lower overall and present several dark spots in areas where the AF fibers are crossing other neural fibers. The $FA_{\text{DMD},vol}$ map shows higher values and fewer dark spots, while the $FA_{\text{DMD},cfo}$ and $FA_{\text{DMD},ang}$ maps show an even more uniform FA map and the dark areas have nearly all disappeared. The total segment length map $w_v^{\mathcal{T}}$, obtained with Eq. (3.9), shows the attribution of a higher weight to voxels in the center part of the AF compared to voxels on the edges.

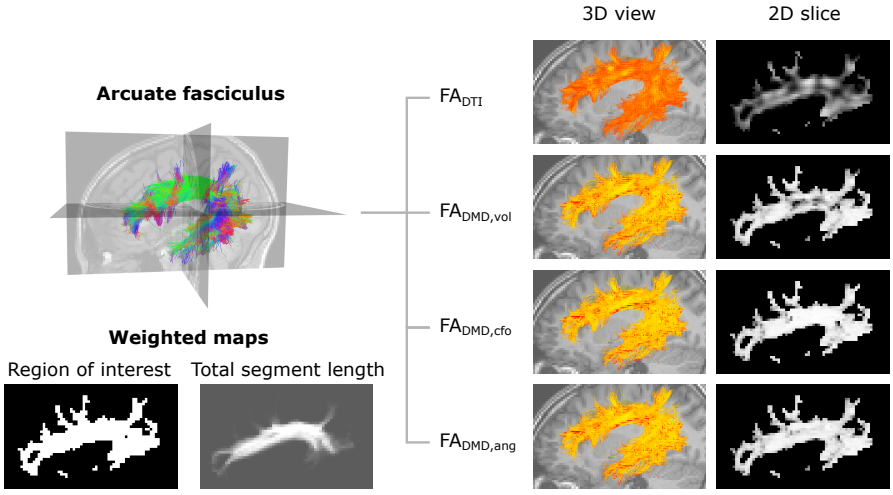

Figure 3.9: Metrics maps obtained with angular weighting are less impacted by the properties of crossing fibers Top-left: representation of the streamlines of the left arcuate fasciculus tract, color-coded for orientation. Bottom-left: weighted maps. The tract-specific total segment length map was obtained with Eq.(3.9) and corresponds to the total length of segments belonging to the AF in each voxel. Right: visualization of the microstructure map over a set of 3D streamlines and a 2D slice of the fractional anisotropy obtained with DTI (FA_{DTI}) and multi-fixel models with: relative volume weighting ($FA_{\text{DMD},vol}$, see Eq. (3.2)), closest-fixel-only ($FA_{\text{DMD},cfo}$, see Eq. (3.3)) and our proposed angular weight ($FA_{\text{DMD},ang}$, see Eq. (3.4)).

The microstructural maps obtained with multi-fixel models combined with angular weighting displayed in Fig. 3.10 show a more uniform orientation in areas of crossing fibers compared to the maps obtained with the single-fixel model DTI. The AF (Fig. 3.10A-B) is predominantly aligned in the antero-posterior direction (green) in the area where it crosses the frontal aslant tract (FAT), whereas maps obtained with DTI present more diverging orientations

and a dominant left-right (red) orientation in several voxels. The FA_{DTI} obtained was also lower in areas of crossing fibers. The FAT shows similar results (Fig. 3.10C-D) where it crosses the corpus callosum connections, with a gain in directionality and a more coherent FVF measure compared to DTI indices.

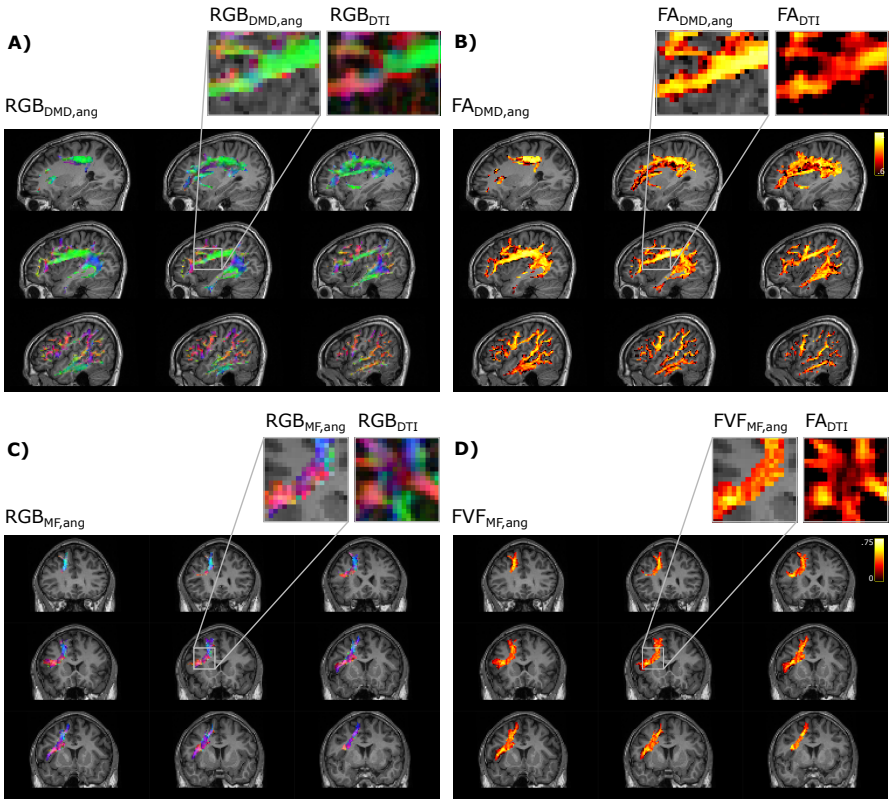

Figure 3.10: Metrics maps using angular weight recover the properties along the direction of the tract. Microstructure maps of the arcuate fasciculus (A,B) and the frontal aslant tract (C,D). **A** Color-coded maps (RGB) of the orientation of the fixel obtained with DIAMOND (DMD) and **C** Microstructure Fingerprinting (MF) are compared to maps obtained with DTI. Microstructural maps of the **B** FA and **D** FVF are also compared to the FA obtained with DTI.

3.5 Discussion

3.5.1 Accuracy of estimation of tract-specific microstructure

When comparing the closest-fixel-only and the proposed angular weighting strategies with relative volume weighting in multi-fixel metrics and with the single-fixel metrics, we observed differences in FA and FVF across all three datasets (Fig. 3.4, 3.6 and 3.8), due to i) multi-fixel information being more accurate than single-fixel information and ii) a focus on the fixels aligned with the tract of interest in each voxel, leading to less contamination by crossing fascicles.

In the synthetic phantom (Fig.3.4), the single-fixel model was inadequate in areas of crossing fibers, as the estimated microstructural properties corresponded to neither of the fiber populations present in the voxel. Using a multi-fixel model capable of discerning the properties of multiple fiber populations in a single voxel, the FA and FVF were still underestimated with relative volume weighting (*vol*) in the horizontal tracts with high ground truth values. Showing that a macroscopic analysis that does not take into account the orientation of the microstructural fixels leads to a sub-optimal estimation of the underlying microstructure. An increased tract-wide mean with angular and total segment length weighting (*ang,tsl*) compared to relative volume and region of interest weighting (*vol,roi*) was also observed in Experiments II and III, which we attribute to the reduction of contamination by crossing fascicles and the use of the total segment length (*tsl*) as a weighted map (Eq. (3.9)). Voxels occupied by more tract segments have a larger weight in the tract-wide average, which mirrors a higher probability of belonging to the tract of interest. This was further illustrated in Fig. 3.9,3.10, where approaches that did not make use of the streamline direction conflated the microstructural metrics of the other fiber tracts intersecting the AF. In Figure 3.9, some of the anomalies visible with traditional DTI disappeared in the $FA_{\mathrm{DMD},vol}$ map. Anomalies remaining with $FA_{\mathrm{DMD},vol}$ were likely due to the averaging of the main fixel properties with a secondary fixel possessing a different FA. The closest-fixel-only and proposed angular weighting strategies bypass these issues by using the orientations obtained from the tractography to more accurately describe brain structures, without interference from crossing fiber tracts.

3.5.2 Robustness to tractography and multi-fixel estimation errors

UNRAVEL makes full use of multi-fixel information and produces results with less variability than single-fixel metrics. In Experiment II (Fig. 3.6), the decreased percentage change of $FA_{\text{DMD},vol}$ and $FA_{\text{DMD},ang}$ compared to traditional DTI indicated a higher reliability of these methods in repeated analyses of the same patient, which is a desirable feature in longitudinal studies.

At the microscopic scale, observing the varying microstructure along the course of a single streamline (Fig. 3.7) showed our framework deals with both "one-to-one" and "one-to-many" correspondence issues between fixels of neighboring voxels. Indeed, the most tract-relevant population switched between the two fixels as their orientations became more aligned with the streamlines of the tract and the method had no issues going from a two-fixel voxel to a single-fixel voxel. The segment-specific FA_{vs} and FVF_{vs} values of a streamline obtained with UNRAVEL are also consistent with the known macrostructure of the corpus callosum, with the segments in the middle of the path presenting higher axonal density. In a configuration with two fiber populations per voxel ($K = 2$), the proposed angular weighting (Eq. (3.4)) is more robust than the commonly used closest-fixel-only strategy (Eq. (3.3)) when the number of fixels is incorrectly estimated by the local microstructural model, as seen in Fig. 3.4 and Fig. 3.5, where an incorrect estimation of the number of fixels in the DIAMOND model led to an overestimation of the microstructural metric. In addition, areas in which angular weighting computes fixels' relative contributions close to $1/K$ will likely lead to more stable estimates than with closest-fixel-only, as streamline segments would have been attributed the microstructural properties of different fixels in the same voxel based on small differences in orientation. Angular weighting should also provide more accurate results in areas where there are more fiber populations than estimated fixels, as the properties of the undetected fixels will be distributed among the K fixels found by the microstructural model, and angular weighting ensures every fixel will have an impact if they are close to the considered orientation.

At the macroscopic scale, the use of total segment length weighting (*tsl*), defined by Eq. (3.12), reduces the impact of outlier and false-positive streamlines on the proposed tract-based metrics, compared to ROI-based means (*roi*), defined in Eq. (3.13). The total segment length map in Fig. 3.9 illustrates this effect, with a reduced weight on the edge of the tract, as well as a weight close to zero in isolated voxels.

3.5.3 Flexibility and usability

The proposed UNRAVEL framework requires little computing power and accepts a wide range of inputs. The choice of a multi-fixel microstructural model is free as long as each fixel has a principal orientation. This means many fixel-specific properties can be investigated, from diffusivity to axon diameter distribution. This is an advantage compared to methods such as FBA [90] which focus on axon fiber density and bundle cross-section, COMMIT [35, 36, 94] and AxTract [96] which require an axon diameter estimation. With our framework, the input streamlines can be generated by any tractography method and segmented into tracts of interest by any approach, from manual to (semi-) automated [37, 110]. Another important degree of freedom is the definition of the relative contribution of a fixel to a streamline segment α_{vsk} and weighted map $\gamma_v^{\mathcal{T}}$. Besides the definitions presented in Section 3.2.1, additional weighting strategies can be defined and included in our framework. In cases where tractography is not available, the tract-specific microstructure maps obtained with relative volume weighting (*vol*) can be used to perform traditional voxel-based analysis (VBA) and region-based analysis using the region of interest weighting (*roi*) by supplying a ROI as input instead of a tract of interest, since relative volume weighting is not dependent on the angular information contained in the tractography, as shown in Fig. 3.2. Finally, our framework enables analysis at different scales: microstructural properties can be obtained for individual streamlines via Eq. (3.7) as in Fig. 3.5 and 3.7, as well as volumetric maps specific to a tract via Eq. (3.10) as in Fig. 3.4, 3.9 and 3.10, and tract-wide summary metrics via Eq. (3.11) as in Fig. 3.6 and 3.8.

3.5.4 Limitations

The UNRAVEL framework is affected by errors in its two inputs and may propagate those estimation errors. Multi-fixel models may incorrectly characterize the fiber populations in a voxel, as in Experiment I (Fig. 3.5). However, the choice of angular weighting (Eq. (3.4)) was shown to reduce this impact. Additionally, total segment length weighting was found to reduce the variability of probabilistic tractography, as seen in Fig. 3.5 and Fig. 3.9. Nonetheless, the UNRAVEL framework is affected by noise from local estimates, resulting in noisy estimates as in the FVF maps in Fig. 3.4. To address this limitation, spatial regularization across fixels belonging to similar macroscopic tracts could be implemented, as proposed in [82].

Another limitation of our experiments is the restriction of multi-fixel models to only two fixels per voxel ($K = 2$), which is known to be insufficient in regions such as the centrum semiovale where the corticospinal tract, fibers

from the corpus callosum, and the superior longitudinal fasciculus intersect. This decision was made due to the challenges in achieving a stable and robust fit for complex multi-fixel models with up to three fixels using current clinical dMRI acquisitions. Other relative contribution definitions might be more suitable when $K > 2$, as the relative weights of aligned fixels will decrease as K increases.

The WM tracts analyzed in our *in vivo* experiments were limited to long-range main white matter pathways, and did not include short-range WM fibers connecting neighboring cortical areas, known as U-fibers. However, the analysis of such fibers using UNRAVEL should not raise issues beyond the need for an accurate tractogram and model estimation as inputs. Furthermore, since the UNRAVEL framework is not dependent on a single model or tractography algorithm, any future improvements in the accuracy of either input will be compatible with our framework and lead to more accurate results.

Finally, although changes in $FA_{\mathrm{DMD},ang}$ and $FVF_{\mathrm{MF},ang}$ suggested the same trend, few statistically significant differences between control and dyslexic children were found in Experiment III. However, this might be due to the restricted sample size and small effect size, which is a well-known pitfall of neuroimaging studies in psychology and psychiatry [111, 112]. Nevertheless, we demonstrated the feasibility of applying our framework to clinical populations and the consistency of the metrics obtained with our approach.

3.6 Conclusion

In this study, we have introduced UNRAVEL, a framework combining the macrostructural information of tractography with the microstructural metrics of multi-fixel models. Combining these two scales with the proposed angular weighting strategy allows tract-specific analyses to be less impacted by crossing fiber tracts, while retaining some robustness in case of erroneous tractography or diffusion model estimations. We demonstrated the feasibility of our framework and the accuracy of our angular weighting algorithm both on synthetic and *in vivo* data. The UNRAVEL framework will provide researchers in the medical field and the diffusion MRI community with a flexible tool to study, visualize and more easily interpret the microstructure of macroscopic white matter pathways in individual cases as well as population studies.

Data Availability Statement

The code is open source and freely available[3]. The programming language is Python and the package is platform independent. The brain MRI data was obtained in the Brussels Saint-Luc University Hospital, Belgium. The data of the adult participant is available from the corresponding author upon reasonable request. The data related to the dyslexic and control children is not available due to privacy issues of clinical data.

Funding

This work was supported by the ARC program of the Wallonia-Brussels Federation (ND) and the Fonds de la Recherche Scientifique - FNRS under Grants n°1.A.690.18F (CG) and J.0214.20 (MV).

[3] https://github.com/DelinteNicolas/UNRAVEL

Part II

Application to population studies

"*When a general knowledge of the structure of the brain is acquired by the student a useful and practical step is gained, because he will not only be able to describe the situation of a lesion and understand the descriptions made by others, but he will be in a situation to intelligently discuss the functions of its parts, and is prepared to work in the field of discovery.*"

-William Fuller, 1896

With the methodologies outlined in Chapter 2 and 3 at our disposal, we are now better equipped to study the evolution of microstructural metrics in population studies. In addition to the dyslexic cohort in Chapter 3, the proposed methods have been applied in several studies analyzing the relationship between brain function and the microstructural properties of neural fibers. The studies, either multi-shell or single-shell, focused on different topics such as unilateral vocal fold paralysis [113], post-lingual deafness and refractory epilepsy [114].

The results obtained using the proposed methodology in these studies have been compared with voxel-based analyses, demonstrating an agreement between the identified tracts and their localized differences, and the voxels highlighting discrepancies between populations. However, there are limitations to the applicability of these methods. While the filtering algorithm described in Chapters 1,2 performs consistently across various datasets as long as the tractography benefits from a sufficient number of gradient directions, the framework in Chapter 3 is dependent on the quality of both the tractography and the selected diffusion model as errors and biases from both components are integrated into the resulting output. As demonstrated in Chapter 3, the errors in tractography can be mitigated by the streamline weighing, while the model errors can be lessened by angular weighting. Nevertheless, this methodology greatly benefits from multi-shell data with a high number of directions. In instances where a single shell was acquired, the tract properties can nonetheless be estimated with DTI, as this is equivalent to a simplification of the algorithm where there is a single fixel to account for.

The following chapters present two examples of multi-shell studies where the methodology developed in this thesis has been applied.
The first study, detailed in Chapter 4, focused on the effects of neurorehabilitation on the microstructural properties of motor neural fibers in children with unilateral cerebral palsy and adults with stroke. Participants in both cohorts experienced limited mobility or limb paralysis due to either abnormal brain development during pregnancy or childbirth, or a cerebrovascular accident that caused cellular death in a brain region. Participants were divided into case and control groups and underwent scans over several months to study the longitudinal effects of motor rehabilitation on the microstructure of the corticospinal tract, the neural pathway connecting the spinal cord to the motor cortex. The microstructure of neural fibers on the lesion-affected side showed different properties compared to the healthier side, with the affected side's properties tending towards those of the healthier side over the course of the study. This change was more pronounced in children, likely due to their higher neuroplasticity and natural development. This study under-

scores the potential of intense and long-term neurorehabilitation to enhance connectivity to motor areas, particularly in children.

The second study, presented in chapter 5, was centered on alcohol use disorder (AUD), a commonly known but complex condition including affective, cognitive and motivational dimensions. While AUD is known to induce whole-brain damages such as grey matter shrinkage and ventricular enlargement, the microstructural changes it induces in the white matter remain incompletely understood. This study leveraged multi-shell diffusion MRI and multi-fixel models, with two aims: i) to investigate differences in white matter tract microstructure between AUD participants tested at the very beginning of alcohol withdrawal and a control cohort; ii) to test the effects of 18 days of abstinence in the AUD group and compare it with a similar delay for retest in the controls. The primary tracts of interest were the corpus callosum, fornix, cingulum and the internal capsule. Comparative analyses between the two cohorts revealed disparities in axial diffusivity and volume fraction across most tracts. Along-tract analyses further discerned differences that were localized in specific sections of certain tracts, while in other tracts the impact was observed all along their pathway. These tract-specific observations bring further insight on the precise impact of AUD on transcallosal fibers and tracts associated with the limbic system, and their potential role on the persistence of AUD. Overall, these findings highlight the long-term vulnerability of tracts associated with the limbic system in AUD and their potential implications for the pathophysiology of alcohol-related conditions.

Chapter IV

Assessment of the white matter microstructure in motor pathways in patients with brain damage

4.1 Introduction

Brain damage can impact several brain functions depending on the lesion's location, including motor skills, sensory processing, cognition, and the overall well-being of the affected person. For those suffering from motor deficits, motor training is a crucial component of neurorehabilitation as it may reduce motor impairment and enhance recovery through brain plasticity. Understanding the extent of brain damage and identifying the damaged areas that can be recruited, those that are beyond recovery, and those that can predict motor recovery is essential for obtaining an early and accurate diagnosis of motor disability and guiding rehabilitation program planning.

Neuroimaging techniques, such as diffusion MRI (dMRI) and its advancements in brain microstructure estimation, have the potential to enhance our understanding of the link between brain structure and motor recovery [115]. These techniques offer new methods for assessing microstructural changes in the damaged brain and predicting patient recovery. Multi-compartment models and other advanced microstructural descriptors have demonstrated the potential of providing more comprehensive descriptions of adults with chronic stroke compared to control subjects [116, 117, 118]. These approaches, when compared to indices derived from the traditionally used diffusion tensor imaging (DTI) model [119, 115], have the potential to offer more specific insights into the structural alterations associated with motor impairments and the response to therapy. In the longer term, they could facilitate the development of predictive biomarkers to guide neurorehabilitation.

The present study leverages these novel approaches to identify damaged areas of the brain and, more specifically, to assess the microstructural properties of the neural pathways connecting to motor control areas. We aim to demonstrate that advanced microstructure analyses can provide deeper insights into the causes of motor impairment and that intensive rehabilitation programs during the early phase of impairment can improve motor recovery. Two cohorts were recruited for this study: adults who had experienced a stroke and children with cerebral palsy. Both neuropathologies are characterized by motor impairments leading to varying degrees of dependence for activities due to brain damage. Both cohorts underwent the Hand and Arm Bimanual Intensive Therapy Including Lower Extremities (HABIT-ILE) rehabilitation method [120] and were scanned at multiple time points throughout the study. The microstructural properties of the corticospinal tract were then assessed at each time point, given its role in motor function and its relevance in stroke [116, 117, 115].

4.2 Materials & Methods

4.2.1 Participants

This study was conducted on two cohorts to investigate the impact of motor training and neurorehabilitation on participants experiencing motor deficits from distinct pathologies.

1^{st} cohort: Children with cerebral palsy

The first cohort consisted of children (N=32) aged 6–18 months with unilesional cerebral palsy (CP), an umbrella term for movement and postural disorders due to brain damage during the brain's development. The brain lesions lead to variable limitations in motor function and manual dexterity, which can impair the execution of daily activities. The children were scanned three (case group) to four (control group) times to study the effect of an intense neurorehabilitation program on the participant's motricity. Several participants of the case group were also scanned four times. The case group followed the HABIT-ILE rehabilitation program in between the first (E0) and second (E1) data acquisition sessions whereas the control group followed the HABIT-ILE method after the third (E2) acquisition session. The timeline of the data acquisition and HABIT-ILE training sessions is illustrated in Fig. 4.1. All children continued their usual care during the study, including nursery and ongoing therapy, generally consisting of a few hours of neurodevelopmental therapy per week. The complete protocol is described in more detail in [121].

2^{nd} cohort: Adults with chronic stroke

The second population was composed of adults with chronic stroke (N=32) aged 40 years or more. Stroke is one of the most common causes of motor disability in adults. Due to a cerebrovascular accident, the blood supply to brain regions is interrupted, causing the death of the cells within those regions. This can result in motor, sensory, and cognitive impairments, as well as an overall decrease in quality of life. The timeline was similar to the one followed with the first cohort, presented in Fig. 4.1. During the time span between two scans, the participants kept their usual motor activity and regular clinical rehabilitation sessions.
Eligible participants presented a diagnosis of hemiparesis following chronic stroke, i.e., 6 months after the initial symptoms. The lesion location varied from one participant to another with the right and left Sylvian segment being the most impacted. Potential participants were excluded if they presented major cognitive impairment or addictions interfering with the study, uncon-

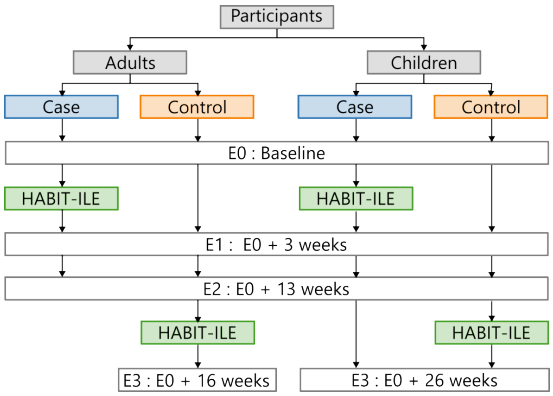

Figure 4.1: Timeline of the data acquisition for both populations: children with cerebral palsy and adults with chronic stroke. Both cohorts were divided into a case (in blue) and control (in orange) group. The HABIT-ILE neurorehabilitation program was followed after E0 by the case group and after E2 for the control group.

trolled health issues, or any contraindications to magnetic resonance imagery such as metal implants or pacemakers. Participants signed a written informed consent ahead of participation. The complete protocol is described in further detail in [122].

4.2.2 Data acquisition & preprocessing

All participants from both cohorts underwent a dMRI sequence on a 3T GE SIGNA Premier scanner (GE Healthcare, Chicago, IL) at each data acquisition session with the following parameters: TR=4837 ms, TE=78 ms, 2 mm isotropic voxels (in-plane FOV: 220x220 mm^2), 110x110x68 x 170 matrix, Δ =35.7 ms, δ=22.9 ms, 64 gradients at b=700, 32 at b=2000, 3000, 5000 s/mm^2, corresponding to diffusion gradients up to 68.9 mT/m, and 7 interspersed b0 images.
Compared to the other multi-shell studies presented in this thesis, the first shell had a b-value of 700 instead of 1000 as the brains of young infants have higher water content compared to adults, with T2- and ADC-values 25-40% longer. In these patients the b-value is often made shorter, in the range of 600-700 s/mm^2. A useful rule of thumb is to pick the b-value so that (b × ADC) ≈ 1, see Appendix A.3 for more information. This change was also applied to the adult population to facilitate the comparison between both cohorts.

A 3D T1-weighted image (TE=4 ms, TR=2312 ms, TI=900 ms) as well as a T2-weighted image (TE=97 ms, TE=2502) were also acquired with 166 slices,

0.8 mm isotropic, in-plane FOV: 256x256 mm^2 for a 166x312x312 matrix.

The preprocessing of the diffusion data was performed using the Elikopy pipeline [123] and included brain extraction [124], denoising with MPPCA [55], Gibbs ringing correction [56], Eddy currents distortion and movement correction [57]. Noise and movement during the scan were estimated with QUAD [105].

4.2.3 Tractography

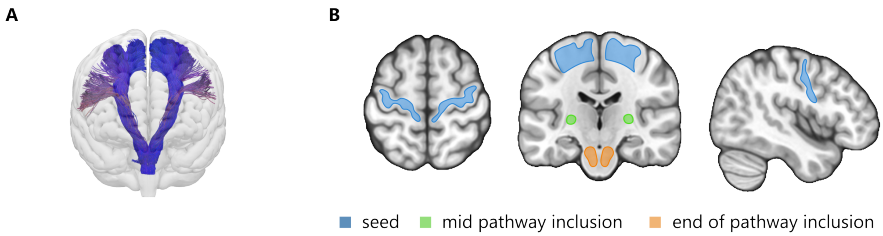

Figure 4.2: A Representation of the corticospinal tracts and **B** the corresponding regions of seed/inclusion used to isolate the streamlines: the precentral gyrus (blue), posterior limb of the internal capsule (green) and medullary pyramids (orange).

To isolate the corticospinal tracts (CST), a seed region was placed in the white matter adjacent to the left and right precentral gyrus to select to primary motor cortex and inclusion regions were added in the posterior limb of the internal capsule and the medullary pyramids in the brainstem [125], as shown in Fig. 4.2B. The regions were drawn in the MNI space using the Harvard-Oxford cortical parcellation [60] and registered to each participant's native space. Several participants (stroke: n=5, CP: n=4) were acquired with fewer slices, removing the inferior part of the brain. For those participants, only the two superior inclusion regions were used, i.e., the motor cortex and posterior limb of the internal capsule.

The MSMT-CSD [26] algorithm was utilized for the local modeling to make full use of the multi-shell data by exploiting the b-value dependencies of the different tissue types. Streamlines were obtained with the iFOD2 [32] algorithm available in the MRtrix3 software [126] with the following parameters: maximum angle of 15°, step size of 1 mm and cutoff of 0.08. A probabilistic tractography algorithm based on MSMT-CSD was used rather than a deterministic one for the increased detection of differences in diffusion characteristics between healthy and affected motor pathways previously shown

in stroke participants [119]. The resulting tracts were cleaned using the methods developed in Chapter 2 to remove spurious streamlines.

4.2.4 Microstructural models and metrics

To assess the morphological alterations in the CST, the volume occupied by the tract's streamlines was utilized to quantify the tract's spatial footprint. Specifically, the number of voxels traversed by streamlines attributed to the CST was aggregated into a *voxel count* metric. This approach served as a model-free method to measure the macroscopic volumetric changes seen in the CST.

Four different diffusion models were used in the analysis to capture different microstructural changes. DTI [76] was selected as the single-fixel model, for comparative purposes with prior studies on motor recovery [119, 115].
DIAMOND was chosen as a multi-tensor and multi-compartment model [20]. Two fiber population compartments and an isotropic volume fraction were allowed to represent the diffusion signal, all compartments are represented using diffusion tensors. Each compartment provided an estimation of the fractional anisotropy (FA), radial diffusivity (RD), axial diffusivity (AD) and volume fraction.
Microstructure Fingerprinting (MF) [21] was chosen as a multi-fixel numerical model, in contrast to DTI and DIAMOND which can be considered analytical models due to their modelling of the diffusion process as tensors. Similarly to DIAMOND, two fixels and an isotropic compartment were allowed to approximate the diffusion signal. MF used the two main directions obtained from MSMT-CSD as input for its metric estimation. Its main output was an estimated fiber volume fraction (FVF) and a volume fraction.
Additionally, the apparent fiber density (AFD) [29] and dispersion were computed from the integral and width of the fODF lobes obtained from MSMT-CSD [29]. Only the three main peaks and their AFD were retained from the full fODF.

The metrics of each model were attributed to the left and right CST of each participant using the methodology developed in Chapter 3.

4.2.5 Analysis

As a result of gradient cycling within the MRI scanner, the presence of patient movement induced noise in the resulting scans. The microstructural metrics

obtained with the aforementioned models, including FA and others, are vulnerable to the effects of noise and motion [127, 128]. To mitigate the impact of the slice-to-volume motion not addressed by the motion correction during the preprocessing, a linear regression was applied on each metric M, to lessen the influence of noise.

$$\begin{aligned}\hat{M} =&\beta_0 + \beta_{SNR} \cdot X_{SNR},\\ M_{res} =&M - \hat{M},\end{aligned}$$

where X_{SNR} is the noise estimation metric computed with FSL's motion correction routine [105], β_0 is the intercept, and β_{SNR} is the regression slope. The tract-specific metrics M_{res}, enable a comparison of the differences unattributed to noise in the two cohorts.

The corrected metrics were employed alongside three analytical tools:

Tool I: Evolution of the contra- and ipsilesional sides This entails grouping the left corticospinal tracts in participants with left-sided brain lesions with the right corticospinal tracts of the participants with a right-sided lesions into an *ipsilesional* group. Conversely, the CST on the unaffected side were grouped into a *contralesional* group.

Tool II: Symmetry ratio We defined a symmetry ratio (SR) between the ipsi- and contralesional sides, which tends to one when both tracts present similar properties.

$$\text{SR} = \frac{M_{contra}}{M_{ipsi}}.$$

This ratio has the benefit of being less sensitive to the variations due to movement and noise, as well as reducing the impact of participants having different metric baselines.

Tool III: Along-tract analysis Using the tools developed in Chapter 2 and 3, an along-tract analysis of the microstructural properties was performed for the ipsi- and contralesional CST. A representation of the major steps is displayed in Fig. 4.3, where both left and right CST are isolated and segmented into smaller subsections to obtain the evolution of microstructural metrics along the pathway.

Figure 4.3: Representation of the different steps of the along tract analysis: **A** tractography of the ipsi- and contralesional corticospinal tracts (in red and green, respectively), **B** segmentation of each tract into smaller subsection along its pathway and **C** analysis of the microstructural metrics of interest for each section along the tract pathway.

4.3 Results

4.3.1 Isolation of the corticospinal tract

The automated generation of corticospinal tracts for children with CP and adults with stroke revealed streamlines connecting the brainstem to the primary motor cortex in both hemispheres in 84% (27/32) and 90% (29/32) of cases, respectively. These tracts, depicted in Fig. 4.4, exhibited accurate anatomical connections with a low number of stray streamlines, mostly in the inferior part of the CST.

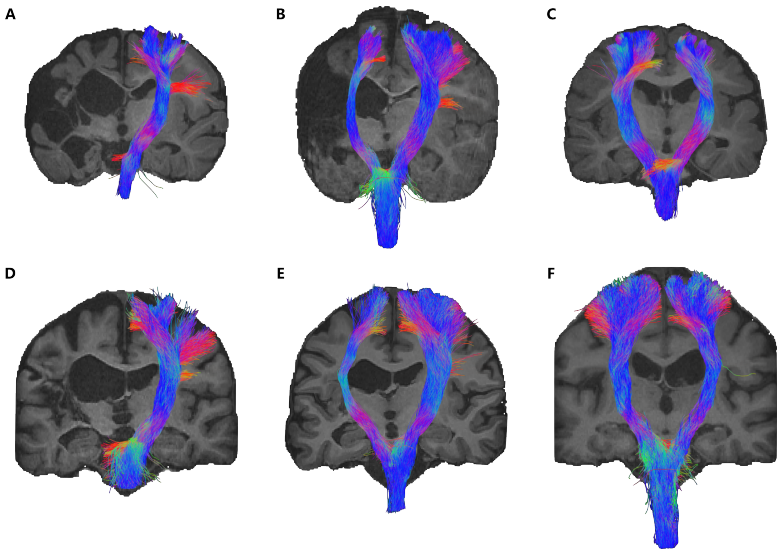

Figure 4.4: Examples of the corticospinal tracts generated for three children with CP (**A**,**B**,**C**) and adults with stroke (**D**,**E**,**F**). The tracts presented have different levels of asymmetry: high (**A**,**D**), medium (**B**,**E**) and low (**C**,**F**).

4.3.2 Longitudinal evolution

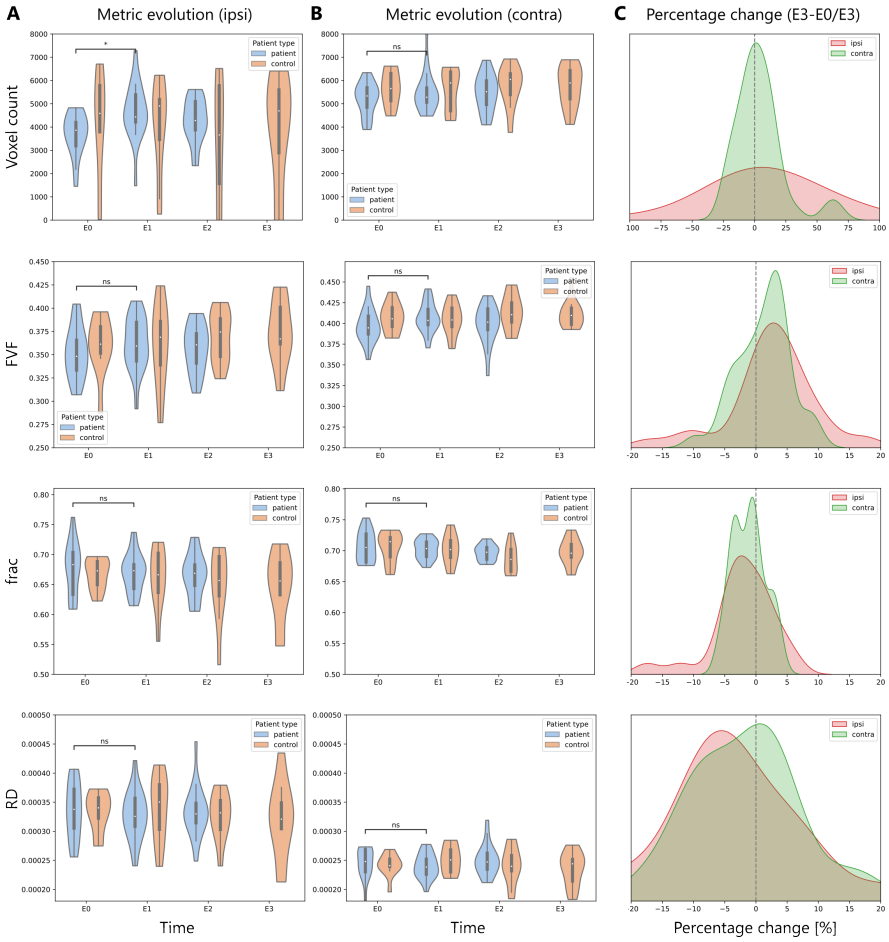

Figure 4.5: Violin plots of the distribution of the different metrics (voxel_count: tract volume, FVF: fiber volume fraction, RD: radial diffusivity, frac: volume fraction) across time for the **A** ipsi- and **B** contralesional sides of the CST for the control (orange) and case (blue) adults with stroke. **C** Distribution of the percentage change between the first and last scan of each participant for the ipsi- (in red) and contralesional side (in green).

Stroke cohort

The metrics demonstrating the most notable evolution over time in the adults cohort are presented in Fig. 4.5. A statistically significant increase in the number of voxels crossed by the CST between time points E0 and E1 was observed on the lesion side in case participants, indicating an increase in CST volume.

These time points consisted of the scans taken immediately before and after the neurorehabilitation training period. Compared to the contralateral side, the ipsilesional side exhibited a lower voxel count, FVF, and volume fraction, along with higher RD. Throughout the study, both tracts demonstrated an increase in voxel count and FVF, while the volume fraction estimated by MF decreased in both tracts on average. Additionally, the RD slightly decreased in the ipsilesional side over the course of the study.

The symmetry ratio, displayed in Fig. 4.6, showed a significant increase in voxel count for the case participants between E0 and E1. Overall, there was an apparent trend for both voxel count and FVF ratios to tend to 1 over time.

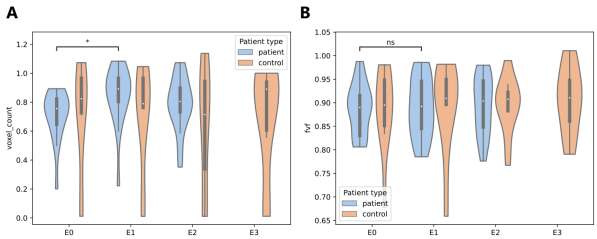

Figure 4.6: Evolution of the distribution of the symmetry ratio of **A** the voxel count and **B** the fiber volume fraction (FVF) between the contra and ipsilesional sides for the control (orange) and case (blue) group across time for adults with stroke.

Cerebral palsy cohort

Changes were more apparent in the children cohort, with both the control and case participants displaying an increased volume for the CST on the lesion side at the final scan compared to the initial scan (Fig. 4.7). The control group also showed a significant increase in volume after the intensive neurorehabilitation training, between time points E2 and E3. Additionally, an increased volume for the CST was noted on the contralesional side. The ipsilesional side showed a significant increase in FVF for the control group at the initial and final scans for the control group. The FA_{DTI} exhibited a significant difference between the control and case groups at time point E1.
Overall, both CST showed an increase of voxel count, FVF, FA, FA_{DTI}, coupled with a decrease in RD, with these changes being slightly more pronounced on the ipsilesional side.

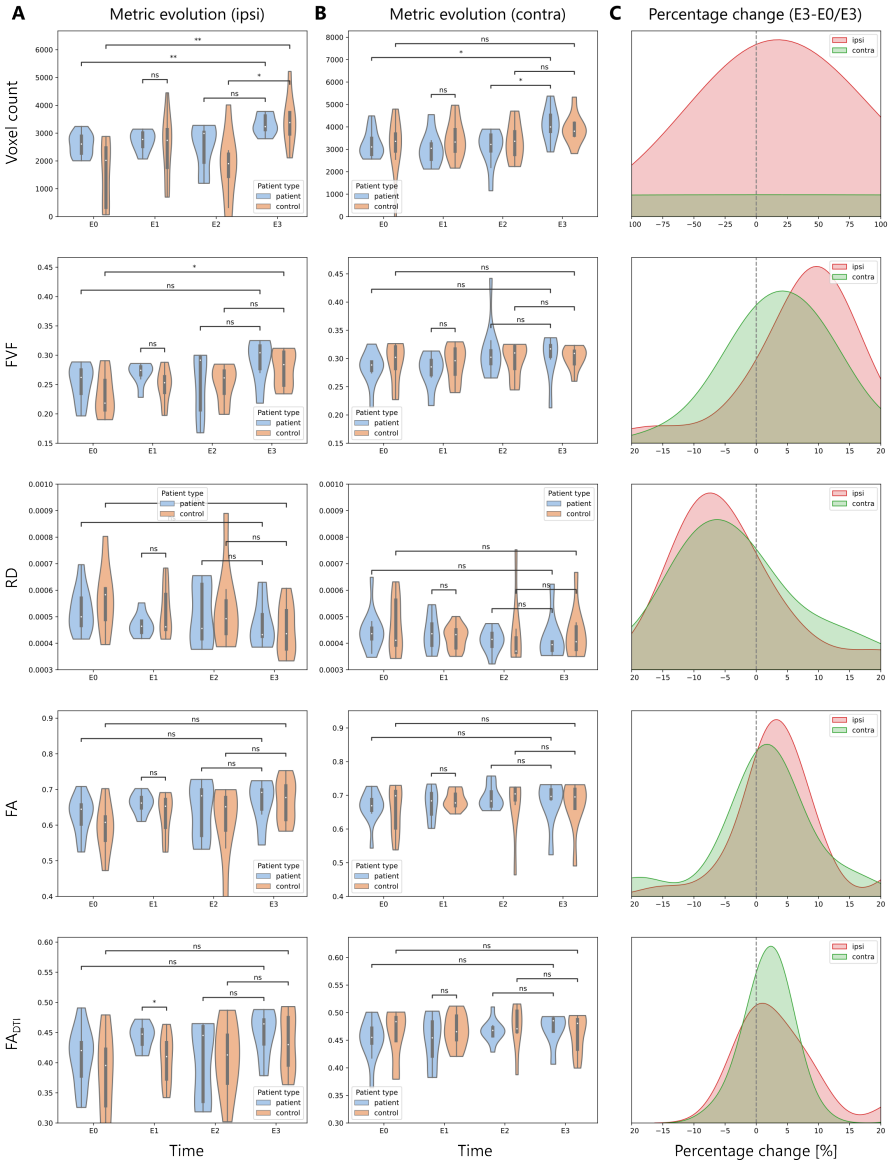

Figure 4.7: Violin plots of the distribution of the different metrics (voxel_count: tract volume, FVF: fiber volume fraction, RD: radial diffusivity, FA: fractional anisotropy) across time for the **A** ipsi- and **B** contralesional sides of the CST for the control (orange) and case (blue) children with CP. **C** Distribution of the percentage change between the first and last scan of each participant for the ipsi- (in red) and contralesional side (in green).

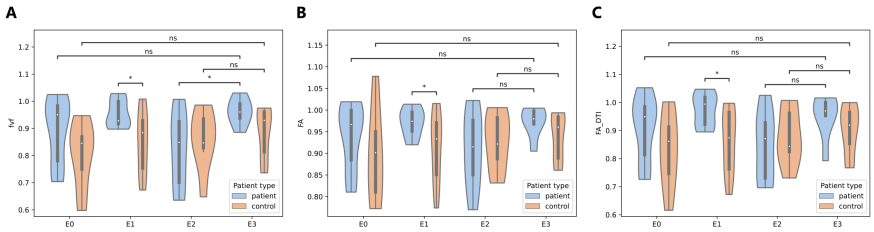

Figure 4.8: Evolution of the distribution of the symmetry ratio of the **A** fiber volume fraction (FVF), **B** FA and **C** FA obtained with DTI between the contra and ipsilesional sides for the control (orange) and case (blue) group across time for children with CP.

The symmetry ratios of the FVF, FA and FA_{DTI} also appeared to tend to 1 as the study progressed, although these changes were had low magnitude and were not statistically significant in most cases (Fig. 4.8).

4.3.3 Evolution along tract

Examining the microstructural metrics along the pathways of the ipsi- and contralesional CST provided a more detailed insight into the specific locations where differences between the two tracts arose.

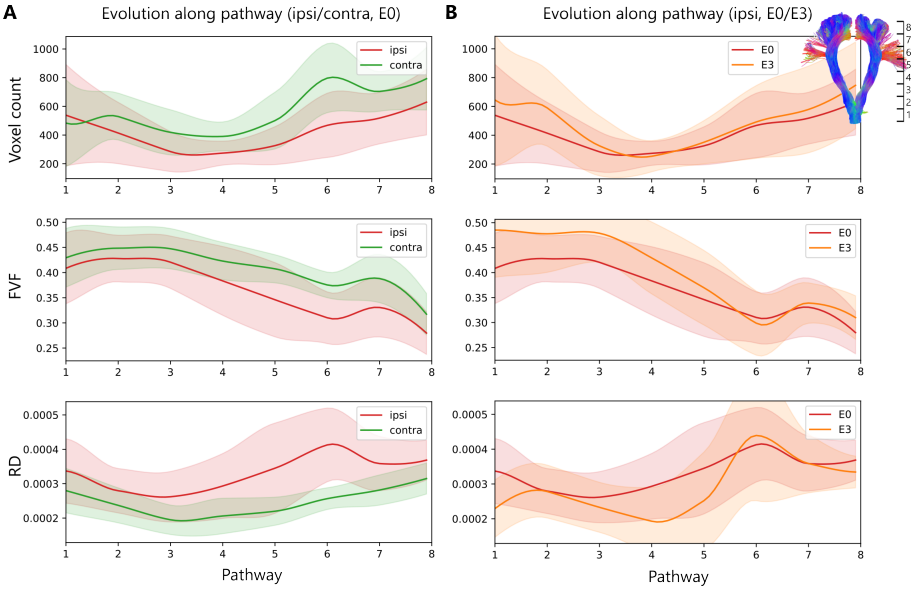

Figure 4.9: Evolution of the different metrics along the pathway of the CST in adults with stroke for **A** the ipsi- and contralesional side at E0 (in red and green, respectively) and **B** for the ipsilesional side at time E0 and E3 (in red and orange, respectively).

Stroke cohort

In the adult cohort, the main differences between the ipsi- and contralesional sides in voxel count, FVF and RD were mainly located above the internal capsule in the pathways displayed in Fig. 4.9A.
The along-tract symmetry ratios for the corresponding metrics, provided in the supplementary materials (Fig. C.1B), exhibited similar values along their pathways at E0 and E3.

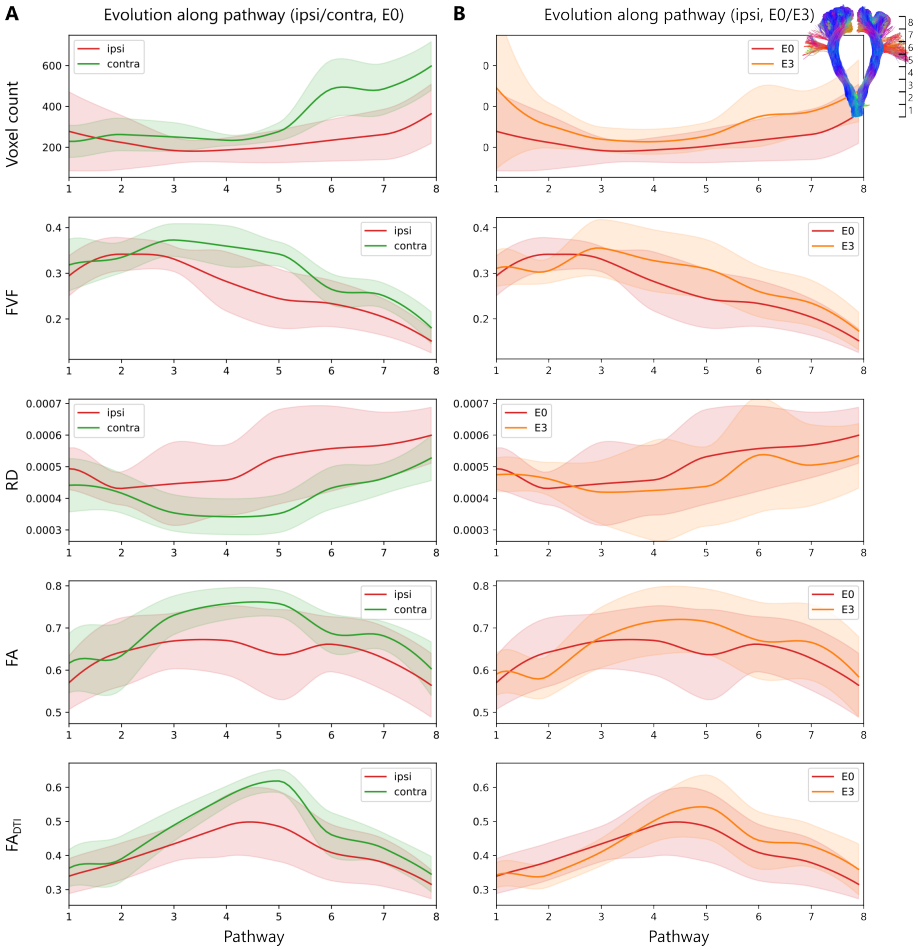

Figure 4.10: Evolution of the different metrics (voxel_count: tract volume, FVF: fiber volume fraction, RD: radial diffusivity, FA: fractional anisotropy) along the pathway of the CST in CP children for **A** the ipsi- and contralesional side at E0 (in red and green, respectively) and **B** for the ipsilesional side at time E0 and E3 (in red and orange, respectively).

Cerebral palsy cohort

Similarly to the stroke cohort, the difference between the ipsi- and contralesional sides were mainly situated above the internal capsule (Fig. 4.10). The differences in the ipsilesional sides throughout the study were more pronounced in the children cohort compared to the adults, with a lower voxel count, FVF, FA, FA_{DTI} and a higher RD in the ipsilesional side. The profiles of the microstructural properties of the ipsilesional CST were closer to the profiles of the initial contralesional tract after the study (E3) compared to the initial scans (E0).
The along-tract symmetry ratios for the corresponding metrics, provided in the supplementary materials (Fig. C.1A), exhibited reduced variability along their pathways and show a mean value closer to 1 at E3 compared to E0.

4.4 Discussion

The primary differences observed in this study included increases in both the volume and fiber density of the CST on the ipsilesional side, with a comparatively smaller increase in volume observed on the contralesional side. While there were instances of a more pronounced increase in CST volume immediately following neurorehabilitation sessions, the majority of changes were observed over the duration of the study.

While the small sample size limits the number of statistically significant differences in other metrics, several trends are discernible from the results presented in the previous section.

4.4.1 Difference between ipsi- and contralesional sides

The majority of the metrics studied in this analysis showed distinct microstructural properties between the contra- and ipsilesional sides. The evolution trends were often similar in both sides of the CST, with a more pronounced change observed in the hemisphere affected by the lesion. The changes observed in the ipsilesional side after the study tended to align more closely with the properties of the contralesional side than in the initial scan. This is especially visible in Fig. 4.10, where the ipsilesional tract pathway profiles tended towards the values of the healthy side, and the shape of the profile was also closer to the contralesional CST.

Although to a lesser extent, the contralesional side also demonstrated changes in its microstructure, tending away from the values observed in the ipsilesional side.

4.4.2 Difference between adults and children

Both cohorts displayed an increased CST volume, fiber volume fraction and reduced radial diffusivity. Although dMRI metrics are sensitive but not entirely specific to biological alterations, these changes may suggest an increased number of neural fibers connecting to the primary motor cortex and a higher myelin coverage [129].

In addition to these common trends, there were cohort-specific distinctions. Specifically, the adults cohort exhibited a decrease in volume fraction, which, when coupled with the increased FVF, could suggest the presence of more densely packed fibers surrounded by partial volumes of other tissue types.

The CP cohort displayed more pronounced changes and differences overall, characterized by a greater number of statistically significant differences and tract profiles that more clearly tended towards the profile of the healthy side after the study.
The children participants also had greater changes in their fractional anisotropy, estimated either with DTI of the fixel-specific FA obtained with DIAMOND. DTI exhibited a greater deviation in its metrics and lower anisotropy at the end of the CST pathway, attributed to the presence of crossing fibers. However, since the CST is one of the primary white matter tracts, its microstructure remained discernible despite the presence of crossing regions.
Both the increase rate of change and the increased FA observed in children compared to the adult cohort are probably due to their ongoing brain development. The general increase in FA might reflect the ongoing maturation of white matter tracts, while the neuroplasticity characteristic of children may further contribute to these observed differences.

4.4.3 Limitations & future perspectives

Due to the position of several participants in the scanner, the medullary pyramids were not always present in the resulting scans. The region of interest for the inferior part of the CST was thus made to include a higher portion of the brainstem to guarantee that the ROI was present in every participant. This included several fibers exiting the cerebellar peduncles. The automated filtering of spurious streamlines used often failed to remove these streamlines connecting the motor cortex to the cerebellum, i.e., fibers belonging to the superior cerebellar fasciculus rather than the CST. This increased the variation of the metrics estimated in the inferior portion of the CST in the along-tract analysis.
Furthermore, several participants were acquired with a fewer number of ax-

ial slices. Brain structures below the occipital lobe were not present in those scans. For these participants, the CST was tracked with only two regions of inclusion: the posterior limb of the internal capsule and the motor cortex.

The challenges in obtaining lengthy MRI scans from children with CP resulted in a substantial number of missing time points, with approximately 60% successful scans, compared to a success rate of 90% in adults with stroke. This substantial amount of missing data may have influenced the outcomes of the study.

For the along-tract analysis on Fig. 4.10B, the E3 time point was taken as the final acquisition to make sure every participant had gone through the neurorehabilitation session, but the first (E0 or E1) and final scans (E1, E2 or E3) could have been used instead.

Future perspectives include a more detailed analysis of the motor tracts by refining the ROIs. For example, the pathway of the corticospinal tract could be modified to incorporate the premotor and sensory cortex. Additionally, separating the different cortical areas that represent various body parts (such as the upper and lower limbs) could help isolate functional changes specific to each body part. Combining these measures with behavioral and motor scores from participants throughout the study could provide deeper insights into the mechanisms underlying motor recovery.
Moreover, examining the corticospinal tract pathway below the brainstem could provide information about the structure of the decussation of motor fibers and their ipsilateral or contralateral organization.

4.5 Conclusion

Although few statistically significant differences were observed immediately before and after the HABIT-ILE program, the changes observed throughout the study hint towards an augmented volume and fiber density following the rehabilitation training, perhaps due to the continuous motor therapy done throughout the study. This increase was more pronounced in the children cohort, probably due to their ongoing brain development and increased neuroplasticity. The changes were also more pronounced in the ipsilesional corticospinal tract, despite the contralesional side displaying similar trends. Overall, this study underscores the potential microstructural changes in motor pathways following intensive rehabilitation programs and their potential implications for enhancing motor function recovery in individuals with neurological disorders such as cerebral palsy and stroke.

Funding

This work was supported by the ARC program of the Wallonia-Brussels Federation. Computational resources have been provided by the Consortium des Équipements de Calcul Intensif (CECI), funded by the Fonds de la Recherche Scientifique de Belgique (F.R.S.-FNRS) under Grant No. 2.5020.11 and by the Walloon Region.

Ethic statement

The studies involving human participants were reviewed and approved by the Ethics Committee of the University Hospital of Saint-Luc
(number: 2013/01MAR/069B403201316810).

Acknowledgements

The data was acquired by A. Carton de Tournai, L. Dricot, E. Gathy and E. Herman of the Institute of NeuroScience (IoNS) of UCLouvain, in the University Hospital of Saint-Luc, Belgium.

Chapter V

Microstructure alterations of white matter tracts associated to the limbic system due to Alcohol Use Disorder

Preliminary version of an article to be submitted as:
Delinte N, Salavrakos M, Dausort M, Dricot L, Hermans P, de Timary P, and Macq B (2024) *Title to be determined*

5.1 Introduction

Alcohol Use Disorder (AUD) is a condition characterized by a problematic pattern of alcohol consumption, where the subject presents a loss of control over its alcohol intake despite the negative consequences on his mental and physical health, social and working obligations, and relationships [130]. It is a complex disorder including affective, cognitive and motivational dimensions and a major public health issue [131, 132]. The direct toxicity of alcohol is mediated by astrocyte swelling, which leads to oxidative and nitrosative stress, impaired intracellular signaling, and modifications of protein and gene expression [133]. In addition, cofactors such as deficiencies in folate, thiamine, pyridoxine and zinc may play critical roles in neurodegeneration caused by alcohol abuse [134]. Magnetic resonance imaging (MRI) of the brain is a valuable tool for unraveling the structural and functional underpinnings of AUD and assessing damages caused by alcohol consumption. Through MRI observations, it has been shown that chronic alcohol abuse entails severe damage to the structure and function of the brain, with widespread effects across cortical and subcortical regions akin to accelerated brain ageing [135], such as gray matter volume loss [136, 137], ventricular enlargement [138, 139] and reduction of white matter "coherence" [140, 141]. Grey matter volume was shown to be largely reduced in several regions of the brain such as the prefrontal cortex and corticostriatal-limbic circuits, including the superior temporal gyrus, striatum, precentral gyrus, left thalamus and right hippocampus [142, 143].

More recently, the development of richer diffusion-weighted MRI (dMRI) sequences helped provide insight into the microstructural underpinnings of AUD in the white matter (WM). In 2022, a meta-analysis by Spindler et al. [144] pooled the results from 18 different studies examining white matter changes through voxel-based morphometry (VBM) and diffusion tensor imaging (DTI). They revealed four clusters of convergent macro- and micro-structural WM alterations. These clusters include the genu and body of the corpus callosum, with extensions to the fornix and the anterior and posterior cingulum bundle, as well as the right posterior limb of the internal capsule. When conducting a meta-analysis based on DTI studies only, they found an additional cluster in the posterior parts of the left corpus callosum.

Studies have been inconclusive regarding the functional repercussions of these structural findings. Altered prefrontal white matter pathways suggested abnormal structural connectivity, where these alterations might underlie deficits and in executive performance in treatment-seeking AUD patients [145]. Studies showed compromised integrity of cortico-striatal fibers, frontal white matter, and limbic pathways, all possibly contributing to exec-

utive functions and impulse control deficits [146, 147]. A recent study correlated microstructural loss of integrity of the fimbria in AUD subjects to cognitive impairments [148]. Furthermore, higher relapse rates were observed in individuals exhibiting lower fractional anisotropy and higher mean diffusivity in the corpus callosum and fornix [149]. Finally, microstructural alterations in the corpus callosum and the internal capsule of AUD patients correlated to the presence of panic disorder as a comorbidity [150].

Spindler et al., concluded their metananalysis by highlighting the importance of studies designed to unravel the respective behavioral implications of the different clusters of WM alterations, and to evaluate the extent of reversibility of these alcohol-related WM changes. Our study was designed as a first attempt to fill this gap in a cohort of 53 AUD patients, admitted at our university hospital for alcohol withdrawal, and carefully selected to still be actively drinking. The alterations of white matter tracts on the day of admission were examined to evaluate whether the above-mentioned findings using dMRI could be replicated. These findings were compared with behavioral measures of depression, anxiety and craving taken by validated questionnaires obtained on the next day. Then, the evolution of these alterations after a period of supervised withdrawal of 18 days was investigated. Results were compared with a control population of 20 healthy subjects, that were also tested twice with an 18-day interval.

From a methodological point of view, most existing studies rely on Diffusion Tensor Imaging (DTI) [11] for the local modelling. However, DTI is limited in its ability to characterize fibers in areas of crossing fascicles. Moreover, the use of tools such as Tract-based spatial statistics (TBSS) [151] may compromise spatial resolution due to the registration of the Fractional Anisotropy (FA) skeleton, in contrast to analyses conducted in native space. Additionally, techniques such as VBM [152] may blend adjacent tract information due to the smoothing step and the registration of misaligned brain structures resulting from brain deformations or differences in the folding pattern.
The present study addresses these limitations by leveraging multi-shell, high-gradient dMRI data, analyzed with a multi-fixel model. Multi-fixel models estimate the properties of multiple fiber populations per voxel, known as *fixels*, enabling the investigation of microstructural metric evolution along specific tracts without taking into account the microstructural properties of crossing tracts. The selection of the tracts of interest is based first on the meta-analysis by Spindler et al. but also confirmed by the results of a multi-fixel whole-brain analysis.

5.2 Materials & Methods

5.2.1 Participants

Participants were recruited in a population of patients diagnosed with AUD and hospitalized at Cliniques Universitaires Saint-Luc for a three-week alcohol withdrawal. Patients were actively drinking until the day of admission; their last alcohol intake had to be the day of admission or the day before. Exclusion criteria were the presence of severe psychiatric comorbidities (i.e., schizophrenia, bipolar disorder) as estimated by a psychiatrist (MS, PdT), chronic inflammatory diseases (i.e., lupus, vasculitis), regular use of anti-inflammatory drugs, the presence of metallic implants (i.e., pacemakers) or unremovable jewelry causing artifacts in the MRI scans. Fifty-three patients met these criteria and were willing to participate in the study. The sample was constituted of 42 men and 11 women, with a mean age of 47,64 years (SD:±10.5; minimum: 28, maximum: 71). The majority of patients were smokers (29 smokers/24 non-smokers). Their average daily alcohol consumption was 17.34 units (SD:±11.35; 1 unit = 10g of ethanol). The difference in alcohol intake between men and women was not statistically significant (18.9 units ±11.72 for men vs 11.36 units ±7.67 for women, F = 2,192, p-value = 0,145). They underwent MRI scans on the day of admission (D1) and after 18 days of withdrawal (D19). In the initial first seven days, participants received a treatment with oral diazepam (a benzodiazepine) to prevent the emergence of withdrawal symptoms (i.e., seizures, confusion), which was progressively tapered.

Additionally, a control group comprising 20 healthy adults was recruited for comparative analysis. They did not differ for age (mean age was 51.3 years ±15.07, p=0.245) or gender (13 men/7 women, p=0.233). For 6 patients, technical problems occurred during the first MRI acquisition. Four more patients had insufficient data quality for the diffusion-weighted MRI sequence. This left a total of 43 patients for E1. Two patients withdrew their consent before E2, two others were excluded for alcohol reconsumption, and one patient had to leave the hospital for family reasons. One patient had the second MRI at E2 but the quality of the diffusion data was insufficient. One control subject also dropped out. Thus 37 a total of patients and 19 controls had their two interpretable scans at D1 and D19, see Fig 5.1 for a summary of the dropouts.

The experiment was carried out with respect to the ethical standards of the Declaration of Helsinki and received approval by the Ethics Committee of the University Hospital of Saint-Luc (number: B403201523514).

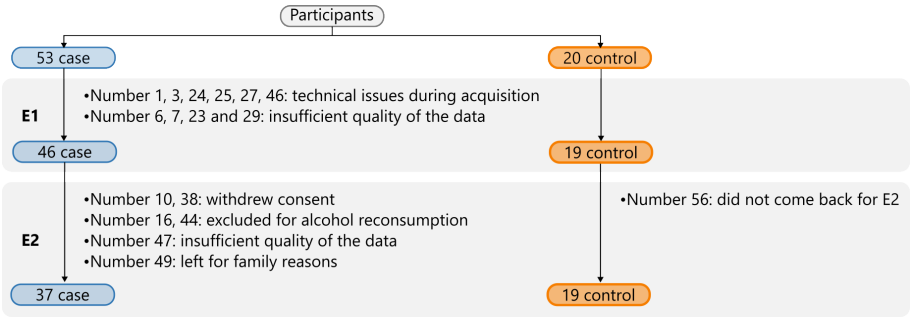

Figure 5.1: Simplified representation of the total participants in the case and control groups, as well as the respective dropouts in each cohort for each acquisition at admission (E1) and after the 18 day abstinence period (E2).

5.2.2 Behavioral assessment

In all individuals on the second day of the program (D2), behavioral data was collected using validated questionnaires, including the Beck Depression Inventory (BDI) for depression, the State Anxiety Inventory (SAI) for anxiety, and the Obsessive Compulsive Drinking Scale (OCDS) for obsessions and compulsions related to drinking (Fig. 5.2B).

5.2.3 Data acquisition and pre-processing

The 37 AUD participants underwent two dMRI scans: the first and second scans were performed on day 1 and 19 of the three-week withdrawal period. Similarly, the 19 healthy adults underwent two dMRI scans 18 days apart. All scans were performed on a 3T GE SIGNA Premier scanner (GE Healthcare, Chicago, IL) with the following parameters: TR = 4837 ms, TE = 80 ms, 2 mm isotropic voxels, in-plane FOV: 220 × 220 mm^2, 110x110x68 x 168 matrix, Δ = 35.7 ms, δ = 22.9 ms, 64 gradients at b = 1000, 32 at b = 2000, 3000, 5000 s/mm^2, corresponding to diffusion gradient intensities up to 68.9 mT/m, and 7 interspersed b0 images.
Preprocessing of the diffusion data was performed using the Elikopy pipeline [123] and included brain extraction [75], thermal denoising [55], Eddy-current distortion and head-motion correction [57] (Fig. 5.2A). Noise and movement during the scan were estimated with QUAD [105].
A 3D T1 image was also acquired with each scan with the following parameters: TE = 2.96 ms, TR = 2188.16 ms, TI = 900 ms, 156 slices, 1 mm isotropic, in-plane FOV: 256 × 256 mm^2.

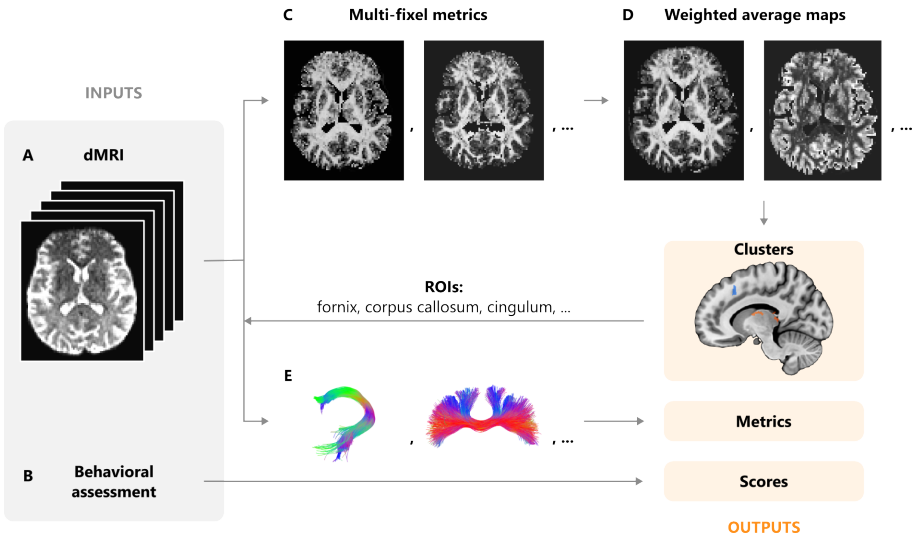

Figure 5.2: Global overview of the analysis pipeline. The two main inputs are: **A** preprocessed diffusion MRI data and **B** behavioral assessments. The **C** metric outputs of the multi fixel model are combined to create **D** whole-brain microstructure maps. The maps are used to detect clusters of interest. The locations of the clusters are used to select tracts of interest and **E** tractography is then generated to obtain tract-specific microstructural metrics.

5.2.4 Microstructural model

To evaluate the microstructural differences between both cohorts, DIAMOND [20] was selected as the multi-fixel model. DIAMOND provided tensor-derived metrics, including fractional anisotropy (FA), axial diffusivity (AD), radial diffusivity (RD), and mean diffusivity (MD) for each estimated fixel (Fig. 5.2C). FA is an index of white matter coherence that decreases when neural fibers are damaged. AD represents the diffusivity in the primary direction of the ellipsoid (longitudinal or parallel diffusivity), whereas RD represents the diffusivity along the two axes perpendicular to the axial diffusivity (transverse or perpendicular). MD represents the average isotropic diffusivity.

Two fiber populations and an isotropic signal contribution were allowed in each voxel, each compartment was attributed a volume fraction. The diffusivity of the isotropic compartment was set to $3 * 10^{-9}\ m^2/s$ to match the diffusion coefficient of free water at 37°C.

5.2.5 Whole-brain analysis

The per-fixel metrics M_k estimated by DIAMOND were aggregated into a single microstructure map per metric using the relative volume fraction weight for the mean voxel value [77]. The weighted metric will be noted as

$$wM = \frac{\sum_{k=1}^{2} f_k M_k}{\sum_{k=1}^{2} f_k}, \tag{5.1}$$

where M is the metric, k the fixel number and f its relative volume fraction.

Volume-weighted microstructure maps were computed for each subject (AUD and control) at E1 and E2 (Fig. 5.2D). A voxel-based analysis was performed on all microstructure maps. We ran a single-factor analysis of variance (ANOVA) comparing four groups: AUD male subjects, AUD female subjects, male controls, and female controls. Additionally, we ran a correlation between subject values and covariate values computing the age of participants. The homogeneity of the slopes was examined, and no differences were found between groups in the clusters of interest, concluding that age was not a confounding factor in our analysis. A threshold of 200 voxels per cluster and a p-value of 0.001 were selected for significance.

5.2.6 Tracking of the neural pathways of interest

Based on the MNI peak-voxel coordinates of clusters of white matter alterations [144], tractography was used to generate streamlines specific to four tracts of interest intersecting the voxels coordinates (Fig. 5.2E), namely the fornix, the corpus callosum, the cingulum and the tracts passing through the internal capsule, illustrated in Fig. 5.3.

The MSMT-CSD [26] algorithm was utilized for the local modeling to make full use of the multi-shell data by exploiting the b-value dependencies of the different tissue types. Streamlines were obtained with the iFOD2 [32] algorithm available in the MRtrix3 software [126] with the following parameters: maximum angle of 15°, step size of 1 mm and cutoff of 0.1. All the regions of interest (ROIs) for the inclusion zones were drawn to have at least 5mm of width in the MNI space to ensure that all ROI had at least two voxels of depth when registered in the native diffusion space. The registration of the ROIs was done using a Python implementation of the ANTS algorithm [153], which employed both linear and nonrigid transformations to optimize the mutual information between the FA maps on the patient's native space and the FSL HCP1065 FA template. The output was cleaned by removing streamlines with an insufficient number of neighbors along the tract pathways based

on kernel density estimates [41]. Each bilateral tract of interest was divided into its left and right component.

The tracts and inclusion zones used to generate the streamlines are shown in Fig. 5.3 and detailed below:

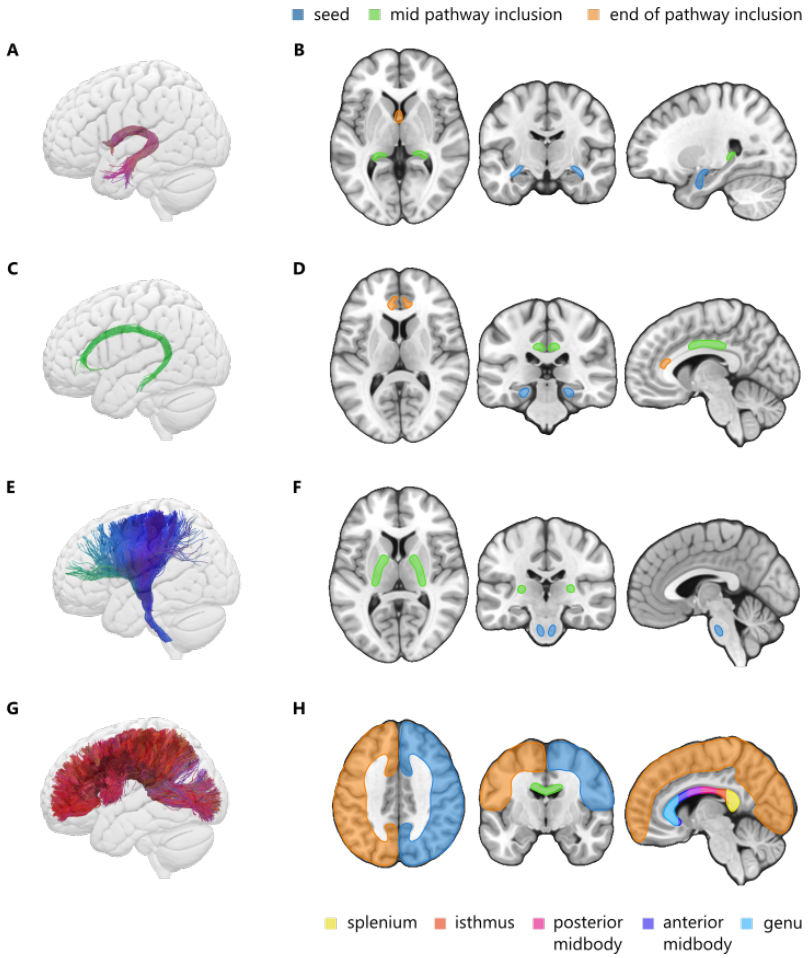

Figure 5.3: Representation of the tracts of interest (**A,C,E,G**) and the corresponding seed (in blue) and inclusion (green, intermediary; orange, termination) regions used to generate the streamlines (**B,D,F,H**) of the fornix (**A,B**), cingulum (**C,D**) internal capsule (**E,F**) and corpus callosum (**G,H**). The corpus callosum is further divided into five regions.

The fornix (Fig 5.3A,B) is a bundle of neural fibers connecting the hypothalamus to several subcortical structures. It is linked to memory formation and provides mnemonic representations to brain structures guiding motivated behavior [154]. The inclusion ROIs for the fornix and fimbria were the columns (anterior pillars) and the crura (posterior pillars) of the fornix, and their connections to the hippocampus [154].

The cingulum (Fig 5.3C,D) is a central structure which interconnects frontal, parietal and medial temporal brain regions as well as subcortical nuclei to the cingulate gyrus. It is implicated in executive control, emotion, appraisal of pain and reinforcement of behavior reducing it (dorsal cingulum), and episodic memory (parahippocampal cingulum) [155]. The ROIs used to generate the main pathway of the cingulum were the anterior part of the cingulum near the genu, and its midcingulate and parahippocampal portions [155].

The internal capsule (Fig 5.3E,F) is located in the inferomedial portion of each brain hemisphere; it is a two-way tract for the transmission of information to and from the cortex. In the Spindler et al. review [144], it was mostly the posterior limb of the internal capsule, which contains corticospinal and sensory fibers, that showed significant white matter alterations. The ROIs used for the generation of the tracts passing through the internal capsule were the medullary pyramids and the posterior limb of the internal capsule.

The Corpus Callosum (CC) (Fig 5.3G,H) is the main interhemispheric white matter tract, with an important role in communicating perceptual, cognitive, and learned information [156]. The ROIs used for the isolation of the corpus callosum tracts were the left and right cortex as well as the corpus callosum proper. The CC was further divided into five subsections (displayed in the sagittal view on Fig 5.3J) using Hofer & Frahm's scheme [156]: the genu, anterior midbody, posterior midbody, isthmus and splenium.

5.2.7 Tract microstructure analysis

With the tracts of interest and microstructure estimates at our disposal, the subsequent step consisted of computing maps (Fig. 5.4B) and averages (Fig. 5.4E) for each metric in the tracts of interest (Fig. 5.4C). For each region, estimates of the FA, AD, RD, MD and volume fraction of the diffusion tensors obtained

with DIAMOND were reported. The mean metric value per tract was obtained with the UNRAVEL framework using the angular weighting for the attribution fixel properties, and the streamline density weighted average to decrease the effect of stray streamlines [77, 74].
To provide more insight on the specific localization of differences between the two cohorts, the evolution of the metric values along the tract pathway (Fig. 5.4G) was calculated by partitioning the mean trajectory into eight subsections (Fig. 5.4D) using the methodology described in [41].

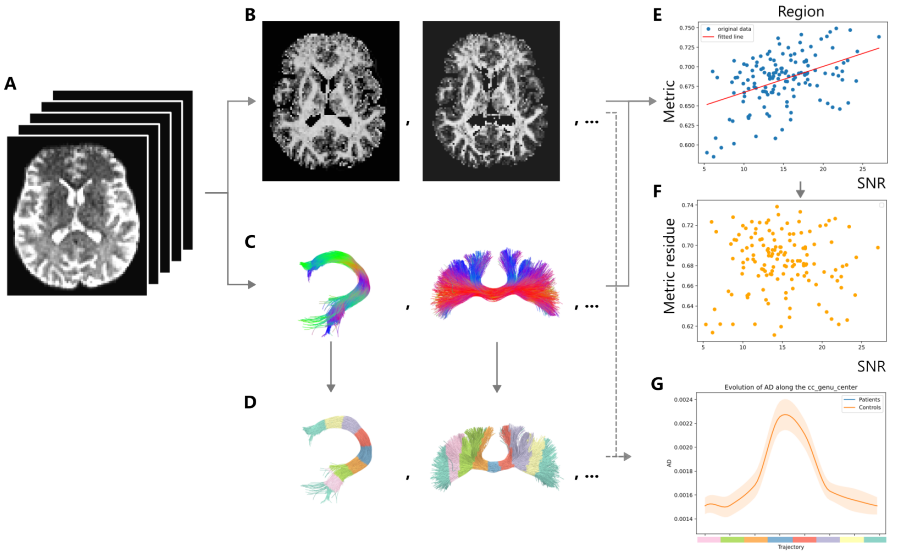

Figure 5.4: Representation of the analysis pipeline, the preprocessed dMRI data (**A**) is processed with multi-fixel models to estimate microstructure metrics (**B**) and with tractography algorithms to generate the streamlines of interest (**C**). Both are then combined to provide an average metric per tract (**E**) which is corrected for movement (**F**). The tracts are also divided into subsections along their pathway (**D**) to obtain the metric evolution along the tract trajectory (**G**).

Due to the implementation of gradient cycling on the MRI scanner, patient movement in the scanner introduced noise. This slice-to-volume motion is not addressed by the head-motion correction during the preprocessing. Since metrics such as FA and others are susceptible to the influence of noise and motion [127, 128], we opted to apply linear regression on each metric M to remove the influence of noise (Fig. 5.4E)

$$\hat{M} = \beta_0 + \beta_{SNR} \cdot X_{SNR},$$
$$M_{res} = M - \hat{M},$$

where X_{SNR} is the noise estimation metric computed with FSL's motion correction routine [105], β_0 is the intercept, and β_{SNR} is the regression slope. The outcome consisted of tract-specific metrics M_{res}, enabling a comparison of differences unattributed to noise between the two cohorts (Fig. 5.4F).
The microstructural metrics of the AUD cohort and control cohort were compared with Welch's t-tests to account for the unequal variances and unequal sample sizes. To account for multiple comparisons, the Benjamini–Hochberg procedure was applied with a false discovery rate set to $\alpha = 0.05$.

5.2.8 Behavioral associations

Behavioral measures were first analyzed independently from dMRI data. Measures of depression, obsession-compulsion, and anxiety were compared between subjects and controls at admission (E1), as well as within subjects between E1 and E2.
Then, correlations between behavioral scores and tract-specific microstructural metrics at E1 (FA, AD, RD and MD) as two independent variables were computed to explore the link between dMRI metrics and behavior. A threshold of a p-value of 0.05 was set for significance.
Using a linear regression model, we tested whether microstructural metrics values that correlated with a behavioral score at E1 could predict the evolution of the said behavioral score at E2.

5.3 Results

5.3.1 Clusters highlighted in the whole-brain analysis

The analysis of the microstructural maps representing the volume fraction weighted metrics obtained with Eq. (5.1) identified several clusters of interest. Among the areas most impacted in terms of volume weighted AD (wAD), displayed in Table 5.1, were the left and right cingulum, the corpus callosum, and the fornix.
For the clusters found with the volume weighted RD (wRD), also displayed in Table 5.1, the left and right cingulum were again prominent, along with several clusters in the corpus callosum.

	MNI coord.					
#	x	y	z	*t*-value	*p*-value	Anatomical label
wAD						
1	8	30	21	7.514	0.000000	**Right cingulum**
2	11	32	−16	5.396	0.000001	
3	0	−15	−33	5.397	0.000001	**Left cingulum**
4	3	−8	4	5.734	0.000000	195R
5	−1	24	31	6.930	0.000000	179L
6	−10	−29	14	5.124	0.000004	**Corpus callosum**
7	−3	5	−17	5.864	0.000000	**Fornix**
8	0	−32	54	5.204	0.000003	67L
9	−2	49	10	6.094	0.000000	187L
10	−10	−2	11	5.705	0.000000	**Fornix**
11	−32	12	−8	5.976	0.000000	Left inferior frontal fasciculus
12	−33	3	6	5.582	0.000001	173L
13	−40	26	8	5.758	0.000000	
14	−43	1	−15	6.027	0.000000	77L
wRD						
1	39	−27	23	−5.833	0.000000	Right Medial Lemniscus
2	50	6	−4	6.283	0.000000	74R
3	22	42	22	−5.422	0.000001	
4	19	33	33	−6.395	0.000000	
5	20	−43	53	−5.961	0.000000	
6	15	−55	40	−4.975	0.000007	**Corpus callosum**
7	18	57	14	−4.644	0.000022	
8	12	−18	49	−5.661	0.000001	**Corpus callosum**
9	8	33	17	−6.414	0.000000	**Right cingulum**
10	0	15	33	−5.334	0.000002	180R
11	10	−32	9	5.886	0.000000	**Corpus callosum**
12	0	−20	51	7.896	0.000000	67L
13	−1	7	53	5.832	0.000000	1L
14	−3	47	14	6.536	0.000000	179L
15	−2	−33	6	5.526	0.000001	**Corpus callosum**
16	−1	11	−12	6.269	0.000000	49L
17	−5	−59	25	−6.198	0.000000	**Left cingulum**
18	−13	41	40	−4.791	0.000013	5L
19	−14	20	39	−5.456	0.000001	**Corpus callosum**
20	−24	−36	−21	5.208	0.000003	103L
21	−27	45	1	−5.692	0.000001	Left Superior Longitudinal Fasciculus
22	−47	11	−11	5.985	0.000000	77L

Table 5.1: Values of the peak voxel coordinates in MNI space, *t*-values and *p*-values, as well as the corresponding anatomical labels, for each statistically significant cluster of the wAD and wRD metrics.

5.3.2 Microstructure of the tracts of interest

The statistically significant p-values resulting from the Welch's t-tests, comparing both cohorts at each time frame for each tract of interest, are presented in Fig. 5.5 to Fig.5.8. Additional graphs are depicted in the supplementary materials (Fig. C.2).

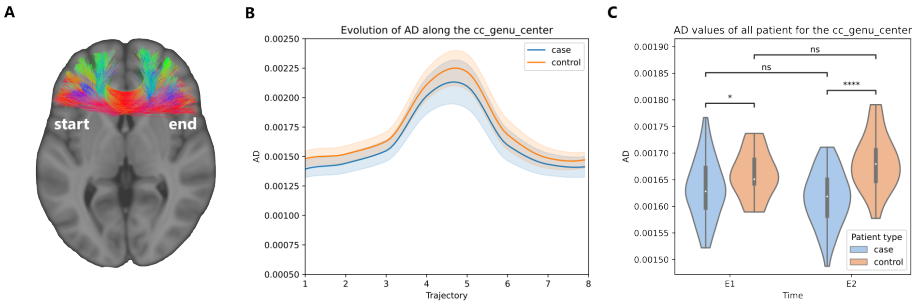

Figure 5.5: Representation of **A** the genu of the corpus callosum (CC), **B** the evolution of AD tract-specific along the tract pathway, and **C** violin plots of the distribution of the genu of the CC microstructure metrics for the AUD (blue) and control (orange) population, before (E1) and after (E2) an 18-day period.

The tract-specific AD was significantly lower in the genu of the CC (Fig. 5.5C), the left fornix (Fig. 5.7C) and the left and right cingulum (Fig. C.2B,C) for the AUD participants compared to controls. The evolution of the metric along the tracts showed a global decrease of the mean AD for participants with AUD in the genu of the CC (Fig. 5.5B), with a decreased mean value across the whole length of the tract.
Conversely, the along-tract analysis in Fig. 5.7B indicated that the primary differences in the fornix between both cohorts originated in the body of the fornix, with less impact in the crura and fimbria.

The volume fraction was higher for the AUD participants in the genu and isthmus of the CC (Fig. C.2A) and in the streamlines passing through the internal capsule (Fig. 5.6C).
Furthermore, differences in the streamlines passing through the internal capsule were predominantly localized in the middle section of their pathway, specifically when the fibers crossed the internal capsule (Fig. 5.6B).

The FA in the left and right cingulum were lower in participants with AUD, as shown in Fig. 5.8C. The main differences between control and AUD were located in the dorsal section of the cingulum (Fig. 5.8B). The temporal

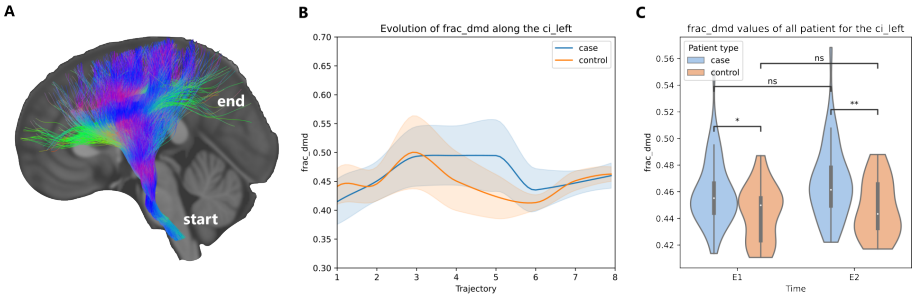

Figure 5.6: Representation of **A** the left streamlines passing through the internal capsule, **B** the evolution of the tract-specific volume fraction along the tract pathway, and **C** violin plots of the distribution of the microstructure metrics for the AUD (blue) and control (orange) population, before (E1) and after (E2) an 18-day period.

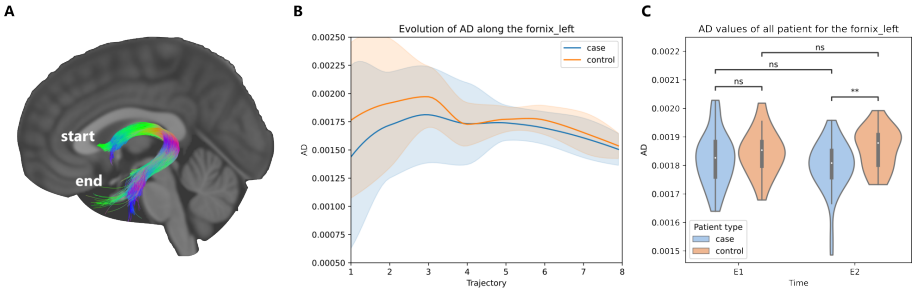

Figure 5.7: Representation of **A** the left fornix/fimbria, **B** the evolution of tract-specific AD along the tract pathway, and **C** violin plots of the distribution of the fornix microstructure metrics for the AUD (blue) and control (orange) population, before (E1) and after (E2) an 18-day period.

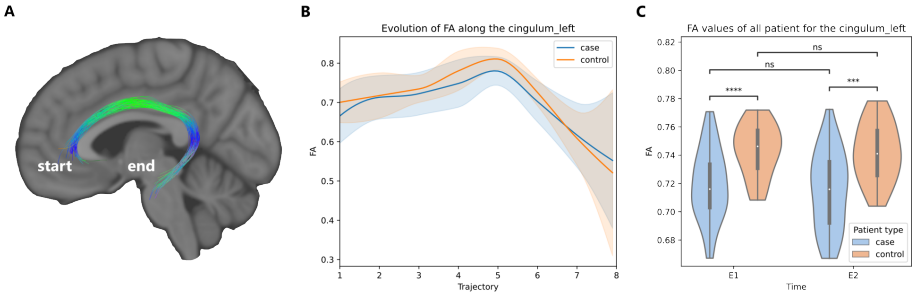

Figure 5.8: Representation of **A** the left cingulum, **B** the evolution of tract-specific FA along the tract pathway, and **C** violin plots of the distribution of the cingulum microstructure metrics for the AUD (blue) and control (orange) population, before (E1) and after (E2) an 18-day period.

section was characterized by a higher standard deviation across participants in AUD and controls.

Finally, there was a decrease in MD in the left and right fibers passing through the posterior limb of the internal capsule in the AUD cohort after the abstinence period (Fig. C.2D).

5.3.3 Differences in behavioral scores and correlations

Behavioral measures were initially examined independently. At E1, subjects exhibited higher scores for depression (BDI), anxiety (SAI), and obsessions-compulsions (OCDS) compared to controls, a difference that was statistically significant (Table 5.2). Among the subjects, there was a significant reduction in all behavioral measures between E1 and E2 (also shown in Table 5.2).

	E1	**vs E2**			**vs Controls**		
	Mean	**Mean**	***t*-value**	***p*-value**	**Mean**	***t*-value**	***p*-value**
BDI	22.41	14.41	4.874	<0.001	5.42	8.136	<0.001
OCDS	14.65	8.27	5.567	<0.001	1.32	10.430	<0.001
SAI	44.57	38.84	3.455	<0.001	29.16	5.746	<0.001

Table 5.2: Comparison of behavioral scores between E1 and E2 in case subjects and between case and controls at E1, and for several questionnaires: Beck Depression Inventory (BDI) for depression, the State Anxiety Inventory (SAI) for anxiety, and the Obsessive Compulsive Drinking Scale (OCDS) for obsessions and compulsions related to drinking.

Regarding the correlations between microstructural metrics and behavioral measures computed at E1 for subjects, significant associations were identified between depression and both the tract-specific FA and RD in several regions (Table 5.3). Specifically, a high depression score was correlated with a low FA, and a high RD. However, no significant correlations were observed for AD and MD; also, no correlations were found for anxiety and OCDS scores.

The prediction of the evolution of the depression score at E2 from the tract-specific FA and RD values correlating with depression at E1 using a linear regression model did not produce any significant results.

	Pearson (r)	p-value
FA		
Anterior midbody of the corpus callosum	−0.365	0.026
Posterior midbody of the corpus callosum	−0.354	0.032
Isthmus of the corpus callosum	−0.514	<0.001
Splenium of the corpus callosum	−0.340	0.039
Left internal capsule	−0.382	0.020
Right internal capsule	−0.375	0.022
RD		
Posterior midbody of the corpus callosum	0.325	0.049
Isthmus of the corpus callosum	0.477	0.003
Right fornix	0.354	0.037
Left internal capsule	0.363	0.027
Right internal capsule	0.382	0.020

Table 5.3: Significant correlations between the tract-specific diffusion metrics and behavioral measures in the group of subjects at E1.

5.4 Discussion

5.4.1 Controls vs AUD

The more pronounced differences appear in the comparisons between the AUD population and the control group.

In the whole-brain analysis, the clusters highlighted several areas within the left and right cingulum and the corpus callosum, which presented lower wAD and higher wRD in AUD patients than in controls. Furthermore, the fornix showed a lower wAD in AUD patients. These regions were also identified as clusters of convergent alterations by Spindler et al. [144]
Three other regions, which did not appear in the later meta-analysis, were also found as clusters of interest in our analysis. The left inferior frontal fasciculus plays a role in language processing and goal-oriented behavior [157]. The medial lemniscus is implicated in sensory function. The left superior longitudinal fasciculus is an associative bundle of tracts involved in speech processing and visuospatial functioning [158].

In the tract-specific analysis, the tracts affected by chronic alcohol consumption in this study were the left fornix, left and right cingulum, the left internal capsule and the genu of the corpus callosum. These tracts predomi-

nantly exhibited either a decreased AD compared to controls, or an increased fiber fraction. The cingulum also displayed a reduction in FA among the AUD participants.
Furthermore, an inverse correlation between the tract-specific FA and depression scores was found in sections of the corpus callosum, namely the splenium and isthmus, and the internal capsules. A previous study in depressive subjects showed an inverse correlation between FA in the corpus callosum and peripheral inflammation [159], which could be the underlying mechanism in AUD subjects as well.

Most dMRI metrics do not directly measure microstructure; although they are sensitive to biological changes in microstructure, they lack specificity for a singular change [160]. Despite this limitation, the significance of each metric can be hypothesized based on common interpretations and an understanding of the associations between biology and metrics derived from prior postmortem studies. The observed decrease in AD may suggest axonal degeneration or deletion [129]. The increased volume fraction associated with a fixel may be indicative of increased fiber density or inflammation in neural fibers. Additionally, since the volume fractions of the different compartments always sums to unity, the increased volume fraction could also result from a reduction in either the volume of crossing fibers or the volume attributed to isotropic diffusivity, such as cerebrospinal fluid or extracellular bodies.
The exact biological processes causing these changes need to be investigated in further studies, with histological analyses.

The microstructural alterations in the fornix are consistent with previous studies which depicted a reduction in FA [148] and indicate that the decreased FA observed with DTI might be due to a decreased AD rather than an increased RD. Excessive alcohol consumption influences the fornix microstructure, with possible consequences for memory formation and cognitive flexibility.
The impact of AUD on the dorsal part of the cingulum might influence the regulation of executive control, high-level processing, and emotion formation [155].
Moreover, AUD may influence the regulation of emotions through its effects on the neural fibers traversing the genu of the CC, also known as the forceps minor. These tracts present connections in the prefrontal cortex and are known to mediate structural connectivity among central executive, salience and default mode networks [145]. Prior DTI studies have linked the forceps minor microstructure to cognitive reappraisal, a central process of emotion regulation [161].

Overall, our study confirms the existence of several clusters of consistent microstructural alterations in AUD subjects. These clusters are part of white matter tracts of the limbic system, regulating emotions, behavior and long-term memory, and the prefrontal cortex, which manages competing goals, as well as executive, affective and motivational functions [162]. Significant associations between depression scores and FA in clusters of the corpus callosum and of the internal capsule point to a link between axonal deletion or degeneration and the depressive symptoms present in most AUD patients before withdrawal. Altogether, these observations support that alcohol-consumption induces a self-perpetuating cycle in AUD patients by altering the brain white matter structure, which induces depression and detrimentally influences cognitive faculties related to judgment and self-control, consequently sustaining a pattern of excessive intake.

Our study highlights the potential of multi-fixel and tract-specific analysis to offer more comprehensive insights than conventional analyses, such as the frequently observed reduction in FA in affected regions (fornix, cingulum, genu) [163, 148], which our findings suggest may be driven by a concurrent decrease in AD rather than a decrease of fiber volume.

5.4.2 Limitations

This study presents several limitations that could be addressed in future research. Firstly, an abstinence period of 18 days might be too short to notice microstructural changes, as alterations during early abstinence have been reported within a broader range of 2-6 weeks [163].
Additionally, the sample size was limited, and the findings should be replicated in a larger cohort to confirm their validity.

Furthermore, the cingulum was considered as a single, continuous bundle. However, it can be divided into two, three or five regions each with different connections in the cingulate cortex and functions [164, 155].

5.5 Conclusion

Previous studies have underlined the need for innovations in data processing and computer modelling to clarify previous observations. This study highlights the potential of leveraging multi-shell data and multi-fixel microstructural modeling to refine the description of the underlying biological processes associated with chronic alcohol consumption. The impact of alcohol on the

microstructure of white matter tracts associated with the limbic system and transcallosal connections is demonstrated to remain into early abstinence, revealing both localized and widespread alterations. The persistence of alterations of diffusion metrics in early abstinence, despite a fast improvement of behavioral measures, points to long lasting effects of excessive alcohol consumption on these structures rather than a faster-recovering effect attributable for example to inflammatory processes. However, this would have to be confirmed by future studies examining the evolution of diffusion metrics into late abstinence. Integrating these observations with other modalities could unveil new biomarkers, paving the way for the development of personalized medicine with practical outcomes benefiting people affected by AUD.

Funding

The MedReSyst-CA project has been supported by the European Union and Wallonia as part of the "Wallonia 2021-2027" program. Computational resources have been provided by the Consortium des Équipements de Calcul Intensif (CECI), funded by the Fonds de la Recherche Scientifique de Belgique (F.R.S.-FNRS) under Grant No. 2.5020.11 and by the Walloon Region. Melissa Salavrakos was funded by a F.R.S.-FNRS grant for doctoral clinical researcher. The MRI collections were obtained thanks to a funding from Fondation Saint-Luc grant.

Ethics statement

The studies involving human participants were reviewed and approved by the Ethics Committee of the University Hospital of Saint-Luc (B403201523514). Written informed consent to participate in this study was provided by the participants' legal guardian/next of kin.

Acknowledgments

The authors thank PhD. Gaetan Duchene for the implementation of the diffusion MRI sequence on the Signa Premier.

Discussion & future perspectives

Before concluding this manuscript, we will go over the context and main results of the methodologies and applications described in the previous sections, along with my current perspective on their practical application, limitations, and the key concepts that should be investigated for future improvements. A broader view of the integration of dMRI measures with other modalities will then be briefly explored.

Synthesis of the main results

Adapting the tractography algorithm with parameter maps

The need for tract-specific parameter values in tractography emerged due to white matter tracts displaying different curvatures and geometries depending on the location of the gray matter regions they connect. Tracts traversing areas along the white-gray matter interface, which folds around the different gyri and whose diffusivity is more isotropic, require a higher maximum angle between tractography steps and a lower termination threshold.
These tractography parameters are typically manually adjusted based on the specific tract of interest, but this could be managed using a singular parameter map. This approach would enable the generation of different types of white matter tracts with diverse geometrical or structural properties with a single tractography. Adapting most tractography algorithms to incorporate this approach is generally straightforward and conceptually simple. While only an angular map with a varying maximum angle parameter has been presented in Chapter 1, this modification could be extended to other parameters, such as a variable step size or streamline termination threshold.

Ideally, location-dependent parameter maps should be determined through histological analyses, leading to the creation of open-source maps in the long term. This would allow users to more easily analyze different types of tracts exhibiting distinct properties such as the U-fibers along the cortex, deep white matter tracts or the neural fibers of the cerebellum.

Easier tract generation

Currently, strategies for generating specific white matter tracts can be categorized into two main approaches: automated procedures based on atlases and manual procedures based on the delineation of ROIs. While atlas-based strategies have improved in recent years [165, 37], their accuracy in segmenting non-standard brains and defining patient-specific tracts outside of pre-defined regions still has room for further improvement. For this reason, manual input remains essential for delineating specific tracts in highly de-

formed brains. The tools developed in Chapter 2 aim to reduce the manual effort needed to produce clean tracts, thereby decreasing the time required for analyses.

My perspective on this matter is that tract generation should involve as few parameters as possible, with those parameters kept as consistent as possible to allow for easier comparisons between tracts, patients, and studies. Adjusting parameters between regions for a single patient hinders tract comparisons in patient-specific analyses and, varying parameters between patients interferes with the results in population studies. Ideally, the number of inclusion ROIs should be limited to a low number, as increasing this number introduces user bias on the expected pathway. It is possible to generate a number of biologically implausible tracts by adding numerous inclusion and exclusion regions and setting non-strict tractography parameters, such as a low cutoff, a high number of trials, and a high maximum angle. Therefore, limiting the number of inclusion regions and restricting tractography parameters offers a more robust and less complex approach, with fewer variables involved.

Furthermore, filtering algorithms should be fast and straightforward to implement. If only a few steps are required to generate a filtered version of the tract, it allows the user to quickly assess whether the filtered output is valuable. The filtering algorithm introduced in Chapter 2 is fast and maintains the integrity of the tract shape, even in regions of low tract density. Conservative approaches are essential to avoid overly relying on processes that might inadvertently discard information.

A framework for multi-fixel analysis

Multi-fixel models produce microstructural properties for each fixel, resulting in multiple volumes for each property. However, these fixels often display coherence issues between adjacent voxel due to the complex interweaving of neural pathways in brain white matter, which is crowded with regions of fiber fanning and crossings. Ordering the fixels coherently without introducing biological criteria or biases is challenging, leading to the distribution of fixels representing a single tract across different volumes.

The UNRAVEL framework, introduced in Chapter 3, addresses this issue by enabling users to attribute fixel properties to a specific tract across these volumes. The framework offers customizable attribution strategies, including tract-agnostic volume fraction weighting and the widely used closest-

fixel-only method. Additionally, a proposed angular weighting strategy is available to increase the robustness of attribution of fixels properties when streamline segments are oriented between two fixels, thereby reducing the impact of small angular variations.

However, angular weighting is not always the most adequate weighting strategy; for instance, volume fraction weighting is recommended for whole-brain analyses, as it allows a single microstructure map to represent the properties of K fixels. For this reason, algorithms and frameworks using multi-fixel model outputs should be flexible and support several angular weighting strategies and averaging methods. The equations developed within the UNRAVEL framework's theory can provide a basis for describing the various ways of assigning microstructural properties to a tract.
Ideally, the same diffusion model should be used for both direction assignment and microstructural analysis, as combining different models can introduce conflicting assumptions and additional limitations. For instance, integrating models such as MTMs with CSD-based orientation estimation can be problematic due to their differing hypotheses regarding the signal's response function (see Background and Appendix A.6 for more information).

Populations studies

Many studies conducted in recent years for estimating the microstructural properties of neural tracts still rely on single-fixel analysis, such as DTI, despite the availability of more advanced multi-compartment models. Perhaps due to the limited availability of these models in clinical settings and their increased complexity compared to DTI. The methodology developed in this thesis leverages these models and has been applied to population studies in Chapters 4 and 5, demonstrating its feasibility for use in large cohorts. These studies would benefit from an increased sample size and the correlation between the estimated tract microstructure and behavioral measures.

One of the main challenges in analyzing multiple tracts and their corresponding metrics across different diffusion models is the increased risk of drawing inferences based on spurious correlations due to multiple comparisons. To address this, corrections such as Bonferroni and Benjamini-Hochberg are often applied to adjust the p-value threshold, but these methods can be overly restrictive. To mitigate this issue, it is useful to prioritize biological hypotheses, thereby reducing the number of regions investigated and, consequently, the number of comparisons performed.

Limitations of the methodology

Despite the features and benefits provided by the contributions above, there are limitations and specific cases where they should not be used or offer little added benefits.

Regarding the methodology developed in Chapter 1, adapting tractography algorithms with location-dependent parameters is valid only if verified with biological studies and shown to be relevant for the algorithms currently in use. Newer algorithms may not rely on the same parameters, potentially rendering these changes insignificant. Nonetheless, developers should remain mindful of the possibility of adapting parameters based on the tractography step's location. The fact that these parameters have traditionally been scalar variables does not mean they must remain so.
Other approaches using adaptive parameters are currently being investigated, such as the attribution of streamline-specific parameters [166]. Furthermore, for specific applications involving U-fibers, other toolboxes and software, such as those described in [63], may be more suitable when the U-fiber tract of interest is included in the predefined atlas and the required software is available.

The filtering algorithm proposed in Chapter 2, and more specifically the estimation of average streamline pathway, currently lacks robustness when dealing with non-linear geometries or branching structures. This limitation can lead to inaccuracies, which may impair the quality of along-tract analysis. In such scenarios, alternative methods such as density filtering for removing spurious streamlines and AFQ [46] to estimate microstructural properties along its pathway might provide more reliable results.

Since the UNRAVEL framework developed in Chapter 3 relies on the quality on its inputs, any limitations inherent in these inputs propagate to the framework's outputs. Consequently, UNRAVEL benefits significantly from multi-shell data with a high number of directions, as these acquisition protocols enhance the accuracy of both the tractography and multi-fixel models.
Moreover, using the UNRAVEL framework to assign multi-fixel properties to tracts is less meaningful if the same model was already employed to generate the tractography. For instance, in the case of CSD-based measures such as AFD, the framework will operate as intended, but the information required to assign the microstructural properties could have been obtained earlier, as the same fODF lobe is used both to measure the AFD and to guide streamline propagation, thereby removing the added value of employing the UNRAVEL framework.

Potential areas for further investigation

Several key concepts emerged as essential for the development of effective tools when implementing the methodology and integrating it with other software. These concepts highlight various areas for improvement in the methodology, which can be categorized under three main criteria.

Validity

The first concept focuses on the necessity and validity of developing the tool itself. It is necessary to assess whether the tool is truly needed: Does the problem need to be solved, or are we optimizing dead-ends? Is there not a more elegant solution?
In our case, the main microstructural analysis method developed in the methodology and applied in the population studies was centered around the outputs of multi-fixel models, which may not be the optimal direction. Other paradigms, such as COMMIT [35], might prove to provide more accurate results in the long term.

The second aspect is the validity of the tool, ensuring that the algorithm's results are accurate and unbiased. This is often challenging to verify, as most dMRI metrics represent an indirect measure of the brain's structure. The tools developed in Chapter 1 and 2 could benefit from additional validation through tests on synthetic data and comparing them to state-of-the-art methods. Furthermore, the results could be verified through histological inspections or expert evaluations.

Usability

Once an algorithm is validated as an accurate estimation of a microstructural property, the next priority is ensuring that the tool is easy to use and implement. This involves several aspects, such as the **availability** of the tool and its **visibility**. While the codes presented in this thesis are open-source and deployed as Python packages, their visibility could be enhanced by integrating them into widely known package libraries.

Implementation should ideally be **fast and straightforward**, without requiring additional programs or dependencies. If users cannot easily test an algorithm, fewer will end up using it. Furthermore, the codes should function

with default parameters and **minimal inputs**. The UNRAVEL framework currently requires several inputs to be in a specific format, simplifying this process could make it easier to use.

Given the constantly evolving software and package environment in research settings, **support** is essential to allow users to submit issues, receive updates, and stay up to date with other packages. Package maintenance could be improved for the methodology in Chapter 1, as it relies on other packages that have been updated since the algorithm was developed.

Finally, to promote the adoption and reduce the learning curve of these algorithms, **tutorials and examples** should be provided. While examples and tutorials are available for the UNRAVEL framework, they could be updated and expanded to cover new features.

Efficiency

The last key concept is code efficiency. Optimizing computation speed and resource usage will accelerate the analysis process and avoid wasting resources. An efficient algorithm not only improves user experience but also makes the methodology more accessible to users with less computing power or with a larger amount of data to process.
Moreover, methodologies and algorithms should be based on simple concepts and designs to **reduce complexity**. Over time, systems tend to become more complex. Minor adjustments and additional options might improve performance, but at the cost of an increased complexity. At some point the increase in performance becomes negligible compared to the increase in complexity. When this point is reached, effort must be deployed to actively reduce the complexity, as this complexity increases the frequency and time required for maintenance, making future development more difficult due to the inertia of an overly complex system. To avoid this, it is important to minimize complexity from the outset. Having fewer 'moving parts' reduces maintenance and enables quicker changes and future evolution, while complex systems tend to become unsustainable.
Regarding complexity, the filtering algorithm could be simplified by adopting a single method for detecting oversteps and missteps while also accounting for non-linear geometries.

A broader view of the integration of dMRI

Implementing the improvements mentioned above will streamline and accelerate the analysis process. This increased efficiency, when combined with complementary measures and imaging modalities, has the potential to enhance our understanding of the underlying mechanisms in pathological brains.

With other MRI modalities

Different MRI modalities provide different contrasts. Combining these modalities enhances the precision and amount of information that can be extracted from the brain. In this work, different contrasts have already been employed alongside dMRI, such as using T1-weighted scans in Chapter 4 and 5 to correct dMRI data artifacts and distortions [167], as well as to register atlases and other modalities using the ANTS software library [168].

Other MRI imaging modalities could be combined to provide a more complete and detailed picture of the brain's microstructure. An example is the estimation of myelin content, which is difficult to visualize with diffusion MRI, as myelin contains few water molecules [169]. However, it can be estimated using other protocols, such as magnetization transfer imaging [170, 171]. Integrating myelin information with microstructural metrics could yield measures such as the *g-ratio*. The g-ratio, defined as the ratio of the inner to outer radius of the myelin sheath surrounding the axon, helps decouple fiber density from myelin density. Research has shown that combining an MRI metric sensitive to myelin volume fraction with one sensitive to the intra-axonal volume fraction (e.g., AFD or FVF) allows for the computation of the g-ratio in each voxel, without needing to explicitly estimate axon diameter and myelin sheath thickness. [172]

Another combination would be integrating fMRI and dMRI for connectivity analyses. Currently, connectivity is divided into structural and functional connectivity, typically estimated using dMRI and fMRI, respectively, each with its own preferred atlases and experimental hypotheses. As seen previously, dMRI can estimate structural connectivity through tractography and quantitative filtering, while functional connectivity is assessed by examining the synchronization of activity across gray matter regions. These two forms of connectivity are biologically linked, as brain activity in gray matter is interconnected by the neural fibers of the white matter, forming communication pathways between regions. This interdependence between gray matter function and white matter characteristics has been partially explored in recent studies [173, 174]. However, combining their outputs within a single

framework could further enhance our understanding of the relationship between the brain's functional and structural connections.

With other imaging modalities

The estimation of multi-modal metrics could be further enhanced by incorporating modalities beyond MRI, such as computed tomography (CT), radiography, and positron emission tomography (PET) scans. Certain pathologies present biological markers linked to disease progression, such as the accumulation of tau protein tangles in Alzheimer's disease, which are associated with amyloid-beta plaque formation. In these cases, PET scans provide an invaluable tool for locating and measuring the evolution of affected brain areas.
Integrating this information with connectivity measures could offer deeper insights into how Alzheimer's disease, primarily a gray matter condition, impacts both structural and functional connectivity across brain regions. This area of research is actively being explored [175].
Furthermore, a unified framework that employs common atlases or even creates pathology-specific atlases could significantly improve the efficiency and effectiveness of multimodal analyses.

With other measures

Going further, combining imaging modalities with other measures could enhance the specificity of our interpretations and potentially lead to the development of accurate biomarkers. A way to develop such biomarkers, or at least deepen our understanding of pathologies, would be to integrate imaging data with other behavioral or biological measures such as blood samples, genetic data, or other physiological factors. This approach could help identify reliable indicators for early detection, diagnosis, and monitoring of treatment response in various neurological conditions, which would, in turn, enable medicine to become more preventive and predictive. For example, combining imaging with behavioral measures, as we did in the AUD study presented in Chapter 5, could deepen our understanding of the connections between brain microstructure and behavioral changes. Similarly, integrating genetic data, as done in [175] for Alzheimer's disease, could reveal important links between genes and brain microstructure.
These biomarkers could facilitate the development of personalized medicine which, when combined with active patient participation, could lead to more tailored and effective patient care.

Conclusion

I believe we are still in the early stages of diffusion MRI, the growth and developments that occurred in the last 30 years have transitioned the technology from proofs of concept to worldwide clinical use. The tools used in the clinical settings are still lagging behind the level of the tools used in research, which themselves do not fully leverage the theoretical advancements made in diffusion models. To go a bit further, the models used in diffusion MRI could also be improved by a more refined application of mathematical concepts, such as through more precise formulation of hypotheses and the implementation of faster algorithms. This multi-disciplinary interdependency is of the key factors for the dynamism of this research field with its components involving mathematics, physics, signal processing, neuroscience, biology, and statistics. Each discipline and their corresponding part in the diffusion MRI pipeline are improving over time and ultimately enhance the quality of the resulting output. Similarly, since the tools developed in this thesis are not dependent on specific implementations or models, they will benefit from future upstream improvements in the scanner sequences, diffusion models and tractography algorithms, to better characterize the microstructure of specific tracts.

Despite its reliance on setting well-defined parameters and the uncertainty in the neural pathway it reconstructs, tractography remains one of the most useful tool neurosurgeons and researchers have at their disposal to investigate the neural pathways in vivo. And as demonstrated in Chapter 1, simple modifications can be implemented in tractography algorithms to improve the accuracy of the generated fiber bundles. As of today, not all brain connections have been identified and ongoing debates persist regarding tract endpoints, the categorization of bundles with similar pathways but differing endpoints, and the subdivisions within fiber bundles. The improvements in algorithms go hand in hand with the discovery of new connections, as emerging tools are being developed to investigate specific tracts, leading to the discovery of potential new pathways. The improvements of Chapter 1 were centered around the distinction between deep white matter tracts and short associations fibers and will hopefully contribute to a more accurate analysis of those short connections, in which the medical field has a growing interest.

The automated filtering described in Chapter 2 with its ease of use, fast computation time and conservative filtering will save researchers time by preventing them from engaging in repetitive tasks to clean the tracts by manually filtering stray streamlines. The absence of a template enables the exploration of lesser-known tracts or the extraction of tracts of interest based on regions obtained with other modalities, such as fMRI-activated regions. This

approach holds promise for patients with abnormal brain structures or a high number of lesions, enabling tailored and patient-specific analyses of neural pathways.

These improvements to tractography algorithms are complemented by the ever-going development of diffusion models, which, despite their increasing complexity and diversity, gain in accuracy and robustness year after year. The UNRAVEL framework described in Chapter 3 will help with the analysis of multi-fixel models along tracts of interest and the comparison of these different models in a single framework. The proposed angular weighing allows tract-specific analyses to be less impacted by crossing fiber tracts, while the streamline density weighted mean increased the robustness in case of erroneous tractography or diffusion model estimations. The theory defined could also be of use to standardize different approaches under a single notation, which would allow researchers to more easily see the differences between the different methodologies employed in generating tract-specific mean values and facilitating implementation in their code.

The tools elaborated in this thesis aimed at facilitating the analysis of white matter tract in neuropathological brains. The feasibility of the implementation of semi-automated analysis tools tailored for neuropathological brains was illustrated with the changes observed in the population studies of Chapter 4 and 5. The studies presented the potential microstructural changes in motor pathways following intensive rehabilitation programs and their potential implications for enhancing motor function recovery. As well as the impact of chronic alcohol consumption on the white matter tracts of the limbic system. The fixel-specific along-tract differences especially look promising as differences in the whole-tract mean often originate from localized differences and a non-statistically significant mean may conceal local differences along the tract. Further integrating these observations with other modalities could unveil new biomarkers, paving the way for the development of personalized medicine.

Bibliography

[1] I. I. Rabi, J. R. Zacharias, S. Millman, and P. Kusch, "A New Method of Measuring Nuclear Magnetic Moment," *Physical Review*, vol. 53, pp. 318–318, Feb. 1938.

[2] F. Bloch, "Nuclear Induction," *Physical Review*, vol. 70, pp. 460–474, Oct. 1946.

[3] E. Odeblad and G. Lindstrom, "Some Preliminary Observations on the Proton Magnetic Resonance in Biologic Samples," *Acta Radiologica*, vol. 43, pp. 469–476, June 1955.

[4] R. Damadian, "Tumor Detection by Nuclear Magnetic Resonance," *Science*, vol. 171, pp. 1151–1153, Mar. 1971.

[5] E. O. Stejskal and J. E. Tanner, "Spin Diffusion Measurements: Spin Echoes in the Presence of a Time-Dependent Field Gradient," *The Journal of Chemical Physics*, vol. 42, pp. 288–292, Jan. 1965.

[6] D. S. Tuch, T. G. Reese, M. R. Wiegell, N. Makris, J. W. Belliveau, and V. J. Wedeen, "High angular resolution diffusion imaging reveals intravoxel white matter fiber heterogeneity," *Magnetic Resonance in Medicine*, vol. 48, pp. 577–582, Oct. 2002. 10.1002/mrm.10268.

[7] D. S. Tuch, T. G. Reese, M. R. Wiegell, and Van J. Wedeen, "Diffusion MRI of Complex Neural Architecture," *Neuron*, vol. 40, pp. 885–895, Dec. 2003.

[8] D. S. Tuch, "Q-ball imaging," *Magnetic Resonance in Medicine*, vol. 52, pp. 1358–1372, Dec. 2004.

[9] I. Aganj, C. Lenglet, G. Sapiro, E. Yacoub, K. Ugurbil, and N. Harel, "Reconstruction of the orientation distribution function in single- and multiple-shell q-ball imaging within constant solid angle," *Magnetic Resonance in Medicine*, vol. 64, pp. 554–566, Aug. 2010.

[10] E. Özarslan, C. G. Koay, T. M. Shepherd, M. E. Komlosh, M. O. İrfanoğlu, C. Pierpaoli, and P. J. Basser, "Mean apparent propagator (MAP) MRI: A novel diffusion imaging method for mapping tissue microstructure," *NeuroImage*, vol. 78, pp. 16–32, Sept. 2013.

[11] P. Basser, J. Mattiello, and D. LeBihan, "MR diffusion tensor spectroscopy and imaging," *Biophysical Journal*, vol. 66, pp. 259–267, Jan. 1994.

[12] J. H. Jensen, J. A. Helpern, A. Ramani, H. Lu, and K. Kaczynski, "Diffusional kurtosis imaging: The quantification of non-gaussian water diffusion by means of magnetic resonance imaging," *Magnetic Resonance in Medicine*, vol. 53, pp. 1432–1440, June 2005.

[13] B. Jeurissen, A. Leemans, J. Tournier, D. K. Jones, and J. Sijbers, "Investigating the prevalence of complex fiber configurations in white matter tissue with diffusion magnetic resonance imaging," *Human Brain Mapping*, vol. 34, pp. 2747–2766, Nov. 2013.

[14] O. Pasternak, N. Sochen, Y. Gur, N. Intrator, and Y. Assaf, "Free water elimination and mapping from diffusion MRI," *Magnetic Resonance in Medicine*, vol. 62, pp. 717–730, Sept. 2009.

[15] H. Zhang, T. Schneider, C. A. Wheeler-Kingshott, and D. C. Alexander, "NODDI: Practical in vivo neurite orientation dispersion and density imaging of the human brain," *NeuroImage*, vol. 61, pp. 1000–1016, July 2012. 10.1016/j.neuroimage.2012.03.072.

[16] M. W. A. Caan, H. G. Khedoe, D. H. J. Poot, A. J. Den Dekker, S. D. Olabarriaga, K. A. Grimbergen, L. J. Van Vliet, and F. M. Vos, "Estimation of Diffusion Properties in Crossing Fiber Bundles," *IEEE Transactions on Medical Imaging*, vol. 29, pp. 1504–1515, Aug. 2010.

[17] T. Behrens, M. Woolrich, M. Jenkinson, H. Johansen-Berg, R. Nunes, S. Clare, P. Matthews, J. Brady, and S. Smith, "Characterization and propagation of uncertainty in diffusion-weighted MR imaging," *Magnetic Resonance in Medicine*, vol. 50, pp. 1077–1088, Nov. 2003.

[18] Y. Assaf and P. J. Basser, "Composite hindered and restricted model of diffusion (CHARMED) MR imaging of the human brain," *NeuroImage*, vol. 27, pp. 48–58, Aug. 2005.

[19] Y. Assaf, T. Blumenfeld-Katzir, Y. Yovel, and P. J. Basser, "Axcaliber: A method for measuring axon diameter distribution from diffusion MRI," *Magnetic Resonance in Medicine*, vol. 59, pp. 1347–1354, June 2008.

[20] B. Scherrer, A. Schwartzman, M. Taquet, M. Sahin, S. P. Prabhu, and S. K. Warfield, "Characterizing brain tissue by assessment of the distribution of anisotropic microstructural environments in diffusion-compartment imaging (DIAMOND): Characterizing Brain Tissue with DIAMOND," *Magnetic Resonance in Medicine*, vol. 76, pp. 963–977, Sept. 2016. 10.1002/mrm.25912.

[21] G. Rensonnet, B. Scherrer, G. Girard, A. Jankovski, S. K. Warfield, B. Macq, J.-P. Thiran, and M. Taquet, "Towards microstructure fingerprinting: Estimation of tissue properties from a dictionary of Monte Carlo diffusion MRI simulations," *NeuroImage*, vol. 184, pp. 964–980, Jan. 2019. 10.1016/j.neuroimage.2018.09.076.

[22] J.-D. Tournier, F. Calamante, D. G. Gadian, and A. Connelly, "Direct estimation of the fiber orientation density function from diffusion-weighted MRI data using spherical deconvolution," *NeuroImage*, vol. 23, pp. 1176–1185, Nov. 2004.

[23] A. W. Anderson, "Measurement of fiber orientation distributions using high angular resolution diffusion imaging," *Magnetic Resonance in Medicine*, vol. 54, pp. 1194–1206, Nov. 2005.

[24] C. Fuchs, Q. Dessain, N. Delinte, M. Dausort, and B. Macq, "Sparse Blind Spherical Deconvolution of diffusion weighted MRI," *Frontiers in Neuroscience*, vol. 18, p. 1385975, May 2024.

[25] J.-D. Tournier, F. Calamante, and A. Connelly, "Robust determination of the fibre orientation distribution in diffusion MRI: Non-negativity constrained super-resolved spherical deconvolution," *NeuroImage*, vol. 35, pp. 1459–1472, May 2007. 10.1016/j.neuroimage.2007.02.016.

[26] B. Jeurissen, J.-D. Tournier, T. Dhollander, A. Connelly, and J. Sijbers, "Multi-tissue constrained spherical deconvolution for improved analysis of multi-shell diffusion MRI data," *NeuroImage*, vol. 103, pp. 411–426, Dec. 2014.

[27] D. Christiaens, S. Sunaert, P. Suetens, and F. Maes, "Convexity-constrained and nonnegativity-constrained spherical factorization in diffusion-weighted imaging," *NeuroImage*, vol. 146, pp. 507–517, Feb. 2017.

[28] F. Dell'Acqua, A. Simmons, S. C. Williams, and M. Catani, "Can spherical deconvolution provide more information than fiber orientations?

Hindrance modulated orientational anisotropy, a true-tract specific index to characterize white matter diffusion: Hindrance Modulated Orientational Anisotropy," *Human Brain Mapping*, vol. 34, pp. 2464–2483, Oct. 2013.

[29] D. Raffelt, J.-D. Tournier, S. Rose, G. R. Ridgway, R. Henderson, S. Crozier, O. Salvado, and A. Connelly, "Apparent Fibre Density: A novel measure for the analysis of diffusion-weighted magnetic resonance images," *NeuroImage*, vol. 59, pp. 3976–3994, Feb. 2012.

[30] D. Hutchison, T. Kanade, J. Kittler, J. M. Kleinberg, F. Mattern, J. C. Mitchell, M. Naor, O. Nierstrasz, C. Pandu Rangan, B. Steffen, M. Sudan, D. Terzopoulos, D. Tygar, M. Y. Vardi, G. Weikum, T. Schultz, C.-F. Westin, and G. Kindlmann, "Multi-Diffusion-Tensor Fitting via Spherical Deconvolution: A Unifying Framework," in *Medical Image Computing and Computer-Assisted Intervention – MICCAI 2010* (T. Jiang, N. Navab, J. P. W. Pluim, and M. A. Viergever, eds.), vol. 6361, pp. 674–681, Berlin, Heidelberg: Springer Berlin Heidelberg, 2010. Series Title: Lecture Notes in Computer Science.

[31] P. J. Basser, S. Pajevic, C. Pierpaoli, J. Duda, and A. Aldroubi, "In vivo fiber tractography using DT-MRI data," *Magnetic Resonance in Medicine*, vol. 44, pp. 625–632, Oct. 2000.

[32] J.-D. Tournier, F. Calamante, and A. Connelly, "Improved probabilistic streamlines tractography by 2nd order integration over fibre orientation distributions," *Proc. Intl. Soc. Mag. Reson. Med. (ISMRM)*, vol. 18, Jan. 2010.

[33] R. E. Smith, J.-D. Tournier, F. Calamante, and A. Connelly, "SIFT: Spherical-deconvolution informed filtering of tractograms," *NeuroImage*, vol. 67, pp. 298–312, Feb. 2013.

[34] R. E. Smith, J.-D. Tournier, F. Calamante, and A. Connelly, "SIFT2: Enabling dense quantitative assessment of brain white matter connectivity using streamlines tractography," *NeuroImage*, vol. 119, pp. 338–351, Oct. 2015. 10.1016/j.neuroimage.2015.06.092.

[35] A. Daducci, A. Dal Palu, A. Lemkaddem, and J.-P. Thiran, "COMMIT: Convex Optimization Modeling for Microstructure Informed Tractography," *IEEE Transactions on Medical Imaging*, vol. 34, pp. 246–257, Jan. 2015. 10.1109/TMI.2014.2352414.

[36] S. Schiavi, M. Ocampo-Pineda, M. Barakovic, L. Petit, M. Descoteaux, J.-P. Thiran, and A. Daducci, "A new method for accurate in vivo mapping

of human brain connections using microstructural and anatomical information," *Science Advances*, vol. 6, p. eaba8245, July 2020. 10.1126/sciadv.aba8245.

[37] D. Wassermann, N. Makris, Y. Rathi, M. Shenton, R. Kikinis, M. Kubicki, and C.-F. Westin, "The white matter query language: a novel approach for describing human white matter anatomy," *Brain Structure and Function*, vol. 221, pp. 4705–4721, Dec. 2016. 10.1007/s00429-015-1179-4.

[38] A. Daducci, E. J. Canales-Rodriguez, M. Descoteaux, E. Garyfallidis, Y. Gur, Y.-C. Lin, M. Mani, S. Merlet, M. Paquette, A. Ramirez-Manzanares, M. Reisert, P. R. Rodrigues, F. Sepehrband, E. Caruyer, J. Choupan, R. Deriche, M. Jacob, G. Menegaz, V. Prckovska, M. Rivera, Y. Wiaux, and J.-P. Thiran, "Quantitative Comparison of Reconstruction Methods for Intra-Voxel Fiber Recovery From Diffusion MRI," *IEEE Transactions on Medical Imaging*, vol. 33, pp. 384–399, Feb. 2014.

[39] L. Ning, F. Laun, Y. Gur, E. V. DiBella, S. Deslauriers-Gauthier, T. Megherbi, A. Ghosh, M. Zucchelli, G. Menegaz, R. Fick, S. St-Jean, M. Paquette, R. Aranda, M. Descoteaux, R. Deriche, L. O'Donnell, and Y. Rathi, "Sparse Reconstruction Challenge for diffusion MRI: Validation on a physical phantom to determine which acquisition scheme and analysis method to use?," *Medical Image Analysis*, vol. 26, pp. 316–331, Dec. 2015.

[40] I. O. Jelescu, M. Palombo, F. Bagnato, and K. G. Schilling, "Challenges for biophysical modeling of microstructure," *Journal of Neuroscience Methods*, vol. 344, p. 108861, Oct. 2020. 10.1016/j.jneumeth.2020.108861.

[41] N. Delinte and B. Macq, "Filtering of spurious streamlines via streamline orientation and pathway density," *Proceedings of the International Society for Magnetic Resonance in Medicine*, vol. 32, 2024.

[42] M. Catani, N. Robertsson, A. Beyh, V. Huynh, F. De Santiago Requejo, H. Howells, R. L. Barrett, M. Aiello, C. Cavaliere, T. B. Dyrby, K. Krug, M. Ptito, H. D'Arceuil, S. J. Forkel, and F. Dell'Acqua, "Short parietal lobe connections of the human and monkey brain," *Cortex*, vol. 97, pp. 339–357, Dec. 2017.

[43] K. Riley, D. O'Neill, and S. Kralik, "Subcortical U-Fibers: Signposts to the Diagnosis of White Matter Disease," *Neurographics*, vol. 8, pp. 234–243, Aug. 2018.

[44] O. R. Phillips, S. H. Joshi, F. Piras, M. D. Orfei, M. Iorio, K. L. Narr, D. W. Shattuck, C. Caltagirone, G. Spalletta, and M. Di Paola, "The superficial white matter in Alzheimer's disease: Superficial White Matter in

Alzheimer's Disease," *Human Brain Mapping*, vol. 37, pp. 1321–1334, Apr. 2016.

[45] A. Yendiki, "Automated probabilistic reconstruction of white-matter pathways in health and disease using an atlas of the underlying anatomy," *Frontiers in Neuroinformatics*, vol. 5, 2011.

[46] J. D. Yeatman, R. F. Dougherty, N. J. Myall, B. A. Wandell, and H. M. Feldman, "Tract Profiles of White Matter Properties: Automating Fiber-Tract Quantification," *PLoS ONE*, vol. 7, p. e49790, Nov. 2012.

[47] B. Q. Chandio, S. L. Risacher, F. Pestilli, D. Bullock, F.-C. Yeh, S. Koudoro, A. Rokem, J. Harezlak, and E. Garyfallidis, "Bundle analytics, a computational framework for investigating the shapes and profiles of brain pathways across populations," *Scientific Reports*, vol. 10, p. 17149, Oct. 2020.

[48] E. St-Onge, K. G. Schilling, and F. Rheault, "BundleSeg: A versatile, reliable and reproducible approach to white matter bundle segmentation," Aug. 2023. arXiv:2308.10958 [cs, eess].

[49] B. Jeurissen, M. Descoteaux, S. Mori, and A. Leemans, "Diffusion MRI fiber tractography of the brain," *NMR in Biomedicine*, vol. 32, Apr. 2019.

[50] C. Román, C. Hernández, M. Figueroa, J. Houenou, C. Poupon, J.-F. Mangin, and P. Guevara, "Superficial white matter bundle atlas based on hierarchical fiber clustering over probabilistic tractography data," *NeuroImage*, p. 119550, Aug. 2022.

[51] C. Mendoza, C. Román, J.-F. Mangin, C. Hernández, and P. Guevara, "Short fiber bundle filtering and test-retest reproducibility of the Superficial White Matter," *Frontiers in Neuroscience*, vol. 18, p. 1394681, Apr. 2024.

[52] D. Shastin, S. Genc, G. D. Parker, K. Koller, C. M. Tax, J. Evans, K. Hamandi, W. P. Gray, D. K. Jones, and M. Chamberland, "Surface-based tracking for short association fibre tractography," *NeuroImage*, vol. 260, p. 119423, Oct. 2022.

[53] H. Takemura, C. F. Caiafa, B. A. Wandell, and F. Pestilli, "Ensemble Tractography," *PLOS Computational Biology*, vol. 12, p. e1004692, Feb. 2016.

[54] E. Garyfallidis, M. Brett, B. Amirbekian, A. Rokem, S. van der Walt, M. Descoteaux, I. Nimmo-Smith, and Dipy Contributors, "Dipy, a library for the analysis of diffusion MRI data," *Frontiers in Neuroinformatics*, vol. 8, Feb. 2014. 10.3389/fninf.2014.00008.

[55] J. Veraart, D. S. Novikov, D. Christiaens, B. Ades-aron, J. Sijbers, and E. Fieremans, "Denoising of diffusion MRI using random matrix theory," *NeuroImage*, vol. 142, pp. 394–406, Nov. 2016. 10.1016/j.neuroimage.2016.08.016.

[56] E. Kellner, B. Dhital, V. G. Kiselev, and M. Reisert, "Gibbs-ringing artifact removal based on local subvoxel-shifts: Gibbs-Ringing Artifact Removal," *Magnetic Resonance in Medicine*, vol. 76, pp. 1574–1581, Nov. 2016. 10.1002/mrm.26054.

[57] J. L. Andersson and S. N. Sotiropoulos, "An integrated approach to correction for off-resonance effects and subject movement in diffusion MR imaging," *NeuroImage*, vol. 125, pp. 1063–1078, Jan. 2016. 10.1016/j.neuroimage.2015.10.019.

[58] M. S. Koyama, D. O'Connor, Z. Shehzad, and M. P. Milham, "Differential contributions of the middle frontal gyrus functional connectivity to literacy and numeracy," *Scientific Reports*, vol. 7, p. 17548, Dec. 2017.

[59] M. Andres, X. Seron, and E. Olivier, "Contribution of Hand Motor Circuits to Counting," *Journal of Cognitive Neuroscience*, vol. 19, pp. 563–576, Apr. 2007.

[60] R. S. Desikan, F. Ségonne, B. Fischl, B. T. Quinn, B. C. Dickerson, D. Blacker, R. L. Buckner, A. M. Dale, R. P. Maguire, B. T. Hyman, M. S. Albert, and R. J. Killiany, "An automated labeling system for subdividing the human cerebral cortex on MRI scans into gyral based regions of interest," *NeuroImage*, vol. 31, pp. 968–980, July 2006. 10.1016/j.neuroimage.2006.01.021.

[61] G. Girard, "The Diffusion-Simulated Connectivity Dataset," Jan. 2022. Type: dataset.

[62] D. B. Aydogan and Y. Shi, "Parallel Transport Tractography," *IEEE Transactions on Medical Imaging*, vol. 40, pp. 635–647, Feb. 2021.

[63] G. Zheng, B. Fei, A. Ge, Y. Liu, Y. Liu, Z. Yang, Z. Chen, X. Wang, H. Wang, and J. Ding, "U-fiber analysis: a toolbox for automated quantification of U-fibers and white matter hyperintensities," *Quantitative Imaging in Medicine and Surgery*, vol. 14, pp. 662–683, Jan. 2024.

[64] K. M. Jordan, B. Amirbekian, A. Keshavan, and R. G. Henry, "Cluster Confidence Index: A Streamline-Wise Pathway Reproducibility Metric for Diffusion-Weighted MRI Tractography," *Journal of Neuroimaging*, vol. 28, pp. 64–69, Jan. 2018.

[65] E. Garyfallidis, M. Brett, M. M. Correia, G. B. Williams, and I. Nimmo-Smith, "QuickBundles, a Method for Tractography Simplification," *Frontiers in Neuroscience*, vol. 6, 2012.

[66] M.-A. Côté, G. Girard, A. Boré, E. Garyfallidis, J.-C. Houde, and M. Descoteaux, "Tractometer: Towards validation of tractography pipelines," *Medical Image Analysis*, vol. 17, pp. 844–857, Oct. 2013.

[67] N. Delinte, Q. Dessain, M. Dausort, C. Vanden Bulcke, and B. Macq, "Tractography of the subcortical U-fibers using a position-dependent maximum angle," *Proceedings of the International Society for Magnetic Resonance in Medicine*, vol. 31, 2023.

[68] K. H. Maier-Hein, P. F. Neher, J.-C. Houde, M.-A. Côté, E. Garyfallidis, J. Zhong, M. Chamberland, F.-C. Yeh, Y.-C. Lin, Q. Ji, W. E. Reddick, J. O. Glass, D. Q. Chen, Y. Feng, C. Gao, Y. Wu, J. Ma, R. He, Q. Li, C.-F. Westin, S. Deslauriers-Gauthier, J. O. O. González, M. Paquette, S. St-Jean, G. Girard, F. Rheault, J. Sidhu, C. M. W. Tax, F. Guo, H. Y. Mesri, S. Dávid, M. Froeling, A. M. Heemskerk, A. Leemans, A. Boré, B. Pinsard, C. Bedetti, M. Desrosiers, S. Brambati, J. Doyon, A. Sarica, R. Vasta, A. Cerasa, A. Quattrone, J. Yeatman, A. R. Khan, W. Hodges, S. Alexander, D. Romascano, M. Barakovic, A. Auría, O. Esteban, A. Lemkaddem, J.-P. Thiran, H. E. Cetingul, B. L. Odry, B. Mailhe, M. S. Nadar, F. Pizzagalli, G. Prasad, J. E. Villalon-Reina, J. Galvis, P. M. Thompson, F. D. S. Requejo, P. L. Laguna, L. M. Lacerda, R. Barrett, F. Dell'Acqua, M. Catani, L. Petit, E. Caruyer, A. Daducci, T. B. Dyrby, T. Holland-Letz, C. C. Hilgetag, B. Stieltjes, and M. Descoteaux, "The challenge of mapping the human connectome based on diffusion tractography," *Nature Communications*, vol. 8, p. 1349, Nov. 2017.

[69] K. G. Schilling, C. M. W. Tax, F. Rheault, B. A. Landman, A. W. Anderson, M. Descoteaux, and L. Petit, "Prevalence of white matter pathways coming into a single white matter voxel orientation: The bottleneck issue in tractography," *Human Brain Mapping*, vol. 43, pp. 1196–1213, Mar. 2022.

[70] F. Pestilli, J. D. Yeatman, A. Rokem, K. N. Kay, and B. A. Wandell, "Evaluation and statistical inference for human connectomes," *Nature Methods*, vol. 11, pp. 1058–1063, Oct. 2014. 10.1038/nmeth.3098.

[71] E. Garyfallidis, M.-A. Côté, F. Rheault, J. Sidhu, J. Hau, L. Petit, D. Fortin, S. Cunanne, and M. Descoteaux, "Recognition of white matter bundles using local and global streamline-based registration and clustering," *NeuroImage*, vol. 170, pp. 283–295, Apr. 2018.

[72] S. Meesters, G. Sanguinetti, E. Garyfallidis, J. Portegies, P. Ossenblok, and R. Duits, "Cleaning output of tractography via fiber to bundle coherence, a new open source implementation," Human Brain Mapping Conference 2016, 2016.

[73] Y. Feng, B. Q. Chandio, J. E. Villalón-Reina, S. I. Thomopoulos, H. Joshi, G. Nair, A. A. Joshi, G. Venkatasubramanian, J. P. John, and P. M. Thompson, "*BundleCleaner* : Unsupervised Denoising and Subsampling of Diffusion MRI-Derived Tractography Data," preprint, Neuroscience, Aug. 2023.

[74] N. Delinte, "DelinteNicolas/UNRAVEL: v1.4.0," Sept. 2023. 10.5281/ZENODO.7753501.

[75] N. Otsu, "A threshold selection method from gray-level histograms," *IEEE Transactions on Systems, Man, and Cybernetics*, vol. 9, no. 1, pp. 62–66, 1979.

[76] P. Basser, J. Mattiello, and D. Lebihan, "Estimation of the Effective Self-Diffusion Tensor from the NMR Spin Echo," *Journal of Magnetic Resonance, Series B*, vol. 103, pp. 247–254, Mar. 1994. 10.1006/jmrb.1994.1037.

[77] N. Delinte, L. Dricot, B. Macq, C. Gosse, M. Van Reybroeck, and G. Rensonnet, "Unraveling multi-fixel microstructure with tractography and angular weighting," *Frontiers in Neuroscience*, vol. 17, p. 1199568, June 2023. 10.3389/fnins.2023.1199568.

[78] S. Shailja, V. Bhagavatula, M. Cieslak, J. M. Vettel, S. T. Grafton, and B. S. Manjunath, "ReeBundle: a method for topological modeling of white matter pathways using diffusion MRI," *IEEE Transactions on Medical Imaging*, pp. 1–1, 2023.

[79] E. J. Canales-Rodríguez, J. H. Legarreta, M. Pizzolato, G. Rensonnet, G. Girard, J. R. Patino, M. Barakovic, D. Romascano, Y. Alemán-Gómez, J. Radua, E. Pomarol-Clotet, R. Salvador, J.-P. Thiran, and A. Daducci, "Sparse wars: A survey and comparative study of spherical deconvolution algorithms for diffusion MRI," *NeuroImage*, vol. 184, pp. 140–160, Jan. 2019. 10.1016/j.neuroimage.2018.08.071.

[80] D. C. Alexander, T. B. Dyrby, M. Nilsson, and H. Zhang, "Imaging brain microstructure with diffusion MRI: practicality and applications," *NMR in Biomedicine*, vol. 32, Apr. 2019. 10.1002/nbm.3841.

[81] B. Jeurissen, A. Leemans, J.-D. Tournier, D. K. Jones, and J. Sijbers, "Investigating the prevalence of complex fiber configurations in white

matter tissue with diffusion magnetic resonance imaging," *Human brain mapping*, vol. 34, no. 11, pp. 2747–2766, 2013.

[82] D. A. Raffelt, R. E. Smith, G. R. Ridgway, J.-D. Tournier, D. N. Vaughan, S. Rose, R. Henderson, and A. Connelly, "Connectivity-based fixel enhancement: Whole-brain statistical analysis of diffusion MRI measures in the presence of crossing fibres," *NeuroImage*, vol. 117, pp. 40–55, Aug. 2015. 10.1016/j.neuroimage.2015.05.039.

[83] Y. Assaf, D. C. Alexander, D. K. Jones, A. Bizzi, T. E. Behrens, C. A. Clark, Y. Cohen, T. B. Dyrby, P. S. Huppi, T. R. Knoesche, D. LeBihan, G. J. Parker, and C. Poupon, "The CONNECT project: Combining macro- and micro-structure," *NeuroImage*, vol. 80, pp. 273–282, Oct. 2013. 10.1016/j.neuroimage.2013.05.055.

[84] Y. Rathi, M. Kubicki, S. Bouix, C.-F. Westin, J. Goldstein, L. Seidman, R. Mesholam-Gately, R. W. McCarley, and M. E. Shenton, "Statistical analysis of fiber bundles using multi-tensor tractography: application to first-episode schizophrenia," *Magnetic Resonance Imaging*, vol. 29, pp. 507–515, May 2011. 10.1016/j.mri.2010.10.005.

[85] J. D. Yeatman, R. F. Dougherty, N. J. Myall, B. A. Wandell, and H. M. Feldman, "Tract Profiles of White Matter Properties: Automating Fiber-Tract Quantification," *PLoS ONE*, vol. 7, p. e49790, Nov. 2012. 10.1371/journal.pone.0049790.

[86] T. Dhollander, A. Clemente, M. Singh, F. Boonstra, O. Civier, J. D. Duque, N. Egorova, P. Enticott, I. Fuelscher, S. Gajamange, S. Genc, E. Gottlieb, C. Hyde, P. Imms, C. Kelly, M. Kirkovski, S. Kolbe, X. Liang, A. Malhotra, R. Mito, G. Poudel, T. J. Silk, D. N. Vaughan, J. Zanin, D. Raffelt, and K. Caeyenberghs, "Fixel-based Analysis of Diffusion MRI: Methods, Applications, Challenges and Opportunities," *NeuroImage*, vol. 241, p. 118417, Nov. 2021. 10.1016/j.neuroimage.2021.118417.

[87] S. Jbabdi, T. E. Behrens, and S. M. Smith, "Crossing fibres in tract-based spatial statistics," *NeuroImage*, vol. 49, pp. 249–256, Jan. 2010. 10.1016/j.neuroimage.2009.08.039.

[88] K. Schilling, Y. Gao, V. Janve, I. Stepniewska, B. A. Landman, and A. W. Anderson, "Can increased spatial resolution solve the crossing fiber problem for diffusion MRI?," *NMR in Biomedicine*, vol. 30, p. e3787, Dec. 2017. 10.1002/nbm.3787.

[89] R. H. J. Fick, D. Wassermann, and R. Deriche, "The Dmipy Toolbox: Diffusion MRI Multi-Compartment Modeling and Microstructure Re-

covery Made Easy," *Frontiers in Neuroinformatics*, vol. 13, p. 64, Oct. 2019. 10.3389/fninf.2019.00064.

[90] D. A. Raffelt, J.-D. Tournier, R. E. Smith, D. N. Vaughan, G. Jackson, G. R. Ridgway, and A. Connelly, "Investigating white matter fibre density and morphology using fixel-based analysis," *NeuroImage*, vol. 144, pp. 58–73, Jan. 2017. 10.1016/j.neuroimage.2016.09.029.

[91] A. Reymbaut, A. V. Caron, G. Gilbert, F. Szczepankiewicz, M. Nilsson, S. K. Warfield, M. Descoteaux, and B. Scherrer, "Magic DIAMOND: Multi-fascicle diffusion compartment imaging with tensor distribution modeling and tensor-valued diffusion encoding," *Medical Image Analysis*, vol. 70, p. 101988, May 2021. 10.1016/j.media.2021.101988.

[92] D. Hutchison, T. Kanade, J. Kittler, J. M. Kleinberg, F. Mattern, J. C. Mitchell, M. Naor, O. Nierstrasz, C. Pandu Rangan, B. Steffen, M. Sudan, D. Terzopoulos, D. Tygar, M. Y. Vardi, G. Weikum, A. J. Sherbondy, M. C. Rowe, and D. C. Alexander, "MicroTrack: An Algorithm for Concurrent Projectome and Microstructure Estimation," in *Medical Image Computing and Computer-Assisted Intervention – MICCAI 2010* (T. Jiang, N. Navab, J. P. W. Pluim, and M. A. Viergever, eds.), vol. 6361, pp. 183–190, Berlin, Heidelberg: Springer Berlin Heidelberg, 2010. 10.1007/978-3-642-15705-9_23.

[93] M. Barakovic, C. M. Tax, U. Rudrapatna, M. Chamberland, J. Rafael-Patino, C. Granziera, J.-P. Thiran, A. Daducci, E. J. Canales-Rodríguez, and D. K. Jones, "Resolving bundle-specific intra-axonal T2 values within a voxel using diffusion-relaxation tract-based estimation," *NeuroImage*, vol. 227, p. 117617, Feb. 2021. 10.1016/j.neuroimage.2020.117617.

[94] M. Ocampo-Pineda, S. Schiavi, F. Rheault, G. Girard, L. Petit, M. Descoteaux, and A. Daducci, "Hierarchical Microstructure Informed Tractography," *Brain Connectivity*, vol. 11, pp. 75–88, Mar. 2021. 10.1089/brain.2020.0907.

[95] M. Reisert, V. G. Kiselev, B. Dihtal, E. Kellner, and D. S. Novikov, "MesoFT: Unifying Diffusion Modelling and Fiber Tracking," in *Medical Image Computing and Computer-Assisted Intervention – MICCAI 2014* (P. Golland, N. Hata, C. Barillot, J. Hornegger, and R. Howe, eds.), vol. 8675, pp. 201–208, Cham: Springer International Publishing, 2014. 10.1007/978-3-319-10443-0_26.

[96] G. Girard, A. Daducci, L. Petit, J.-P. Thiran, K. Whittingstall, R. Deriche, D. Wassermann, and M. Descoteaux, "AxTract: Toward microstruc-

ture informed tractography: AxTract," *Human Brain Mapping*, vol. 38, pp. 5485–5500, Nov. 2017. 10.1002/hbm.23741.

[97] S. Schiavi, P.-J. Lu, M. Weigel, A. Lutti, D. K. Jones, L. Kappos, C. Granziera, and A. Daducci, "Bundle myelin fraction (BMF) mapping of different white matter connections using microstructure informed tractography," *NeuroImage*, vol. 249, p. 118922, Apr. 2022. 10.1016/j.neuroimage.2022.118922.

[98] F. Ahmed Sid, K. Abed-Meraim, R. Harba, and F. Oulebsir-Boumghar, "Analytical performance bounds for multi-tensor diffusion-MRI," *Magnetic Resonance Imaging*, vol. 36, pp. 146–158, Feb. 2017. 10.1016/j.mri.2016.10.014.

[99] M. Nilsson, J. Lätt, F. Ståhlberg, D. van Westen, and H. Hagslätt, "The importance of axonal undulation in diffusion MR measurements: a Monte Carlo simulation study: THE IMPORTANCE OF AXONAL UNDULATION IN DIFFUSION MR MEASUREMENTS," *NMR in Biomedicine*, vol. 25, pp. 795–805, May 2012. 10.1002/nbm.1795.

[100] J. Mollink, M. Kleinnijenhuis, A.-M. v. Cappellen van Walsum, S. N. Sotiropoulos, M. Cottaar, C. Mirfin, M. P. Heinrich, M. Jenkinson, M. Pallebage-Gamarallage, O. Ansorge, S. Jbabdi, and K. L. Miller, "Evaluating fibre orientation dispersion in white matter: Comparison of diffusion MRI, histology and polarized light imaging," *NeuroImage*, vol. 157, pp. 561–574, Aug. 2017. 10.1016/j.neuroimage.2017.06.001.

[101] M. Hall and D. Alexander, "Convergence and Parameter Choice for Monte-Carlo Simulations of Diffusion MRI," *IEEE Transactions on Medical Imaging*, vol. 28, pp. 1354–1364, Sept. 2009. 10.1109/TMI.2009.2015756.

[102] G. Rensonnet, D. Jacobs, B. Macq, and M. Taquet, "A hybrid method for efficient and accurate simulations of diffusion compartment imaging signals," (Cuenca, Ecuador), p. 968107, Dec. 2015. 10.1117/12.2207890.

[103] G. Rensonnet, B. Scherrer, S. K. Warfield, B. Macq, and M. Taquet, "Assessing the validity of the approximation of diffusion-weighted-MRI signals from crossing fascicles by sums of signals from single fascicles," *Magnetic Resonance in Medicine*, vol. 79, pp. 2332–2345, Apr. 2018. 10.1002/mrm.26832.

[104] B. Dhital, M. Reisert, E. Kellner, and V. G. Kiselev, "Intra-axonal diffusivity in brain white matter," *NeuroImage*, vol. 189, pp. 543–550, Apr. 2019. 10.1016/j.neuroimage.2019.01.015.

[105] M. Bastiani, M. Cottaar, S. P. Fitzgibbon, S. Suri, F. Alfaro-Almagro, S. N. Sotiropoulos, S. Jbabdi, and J. L. Andersson, "Automated quality control for within and between studies diffusion MRI data using a non-parametric framework for movement and distortion correction," *NeuroImage*, vol. 184, pp. 801–812, Jan. 2019. 10.1016/j.neuroimage.2018.09.073.

[106] M. Vandermosten, B. Boets, J. Wouters, and P. Ghesquière, "A qualitative and quantitative review of diffusion tensor imaging studies in reading and dyslexia," *Neuroscience & Biobehavioral Reviews*, vol. 36, pp. 1532–1552, July 2012. 10.1016/j.neubiorev.2012.04.002.

[107] M. Vandermosten, B. Boets, H. Poelmans, S. Sunaert, J. Wouters, and P. Ghesquiere, "A tractography study in dyslexia: neuroanatomic correlates of orthographic, phonological and speech processing," *Brain*, vol. 135, pp. 935–948, Mar. 2012. 10.1093/brain/awr363.

[108] C. Banfi, K. Koschutnig, K. Moll, G. Schulte-Körne, A. Fink, and K. Landerl, "White matter alterations and tract lateralization in children with dyslexia and isolated spelling deficits," *Human Brain Mapping*, vol. 40, pp. 765–776, Feb. 2019. 10.1002/hbm.24410.

[109] C. Vander Stappen, L. Dricot, and M. Van Reybroeck, "RAN training in dyslexia: Behavioral and brain correlates," *Neuropsychologia*, vol. 146, p. 107566, Sept. 2020. 10.1016/j.neuropsychologia.2020.107566.

[110] S. Warrington, K. L. Bryant, A. A. Khrapitchev, J. Sallet, M. Charquero-Ballester, G. Douaud, S. Jbabdi, R. B. Mars, and S. N. Sotiropoulos, "XTRACT - Standardised protocols for automated tractography in the human and macaque brain," *NeuroImage*, vol. 217, p. 116923, Aug. 2020. 10.1016/j.neuroimage.2020.116923.

[111] K. S. Button, J. P. A. Ioannidis, C. Mokrysz, B. A. Nosek, J. Flint, E. S. J. Robinson, and M. R. Munafò, "Power failure: why small sample size undermines the reliability of neuroscience," *Nature Reviews Neuroscience*, vol. 14, pp. 365–376, May 2013. 10.1038/nrn3475.

[112] for the ENIGMA Consortium, P. M. Thompson, N. Jahanshad, C. R. K. Ching, and et al., "ENIGMA and global neuroscience: A decade of large-scale studies of the brain in health and disease across more than 40 countries," *Translational Psychiatry*, vol. 10, p. 100, Dec. 2020. 10.1038/s41398-020-0705-1.

[113] M. Dedry, L. Dricot, V. Van Parys, D. Boucquey, N. Delinte, J. Van Lith-Bijl, A. Szmalec, Y. Maryn, and G. Desuter, "Brain adaptation following

various unilateral vocal fold paralysis treatments: A magnetic resonance imaging based longitudinal case series," *Frontiers in Neuroscience*, vol. 16, p. 947390, Oct. 2022.

[114] A. Berger, E. Beckers, V. Joris, G. Duchêne, V. Danthine, N. Delinte, I. Cakiroglu, S. Sherif, E. I. G. Morrison, A. T. Sánchez, B. Macq, L. Dricot, G. Vandewalle, and R. El Tahry, "Locus coeruleus features are linked to vagus nerve stimulation response in drug-resistant epilepsy," *Frontiers in Neuroscience*, vol. 18, p. 1296161, Feb. 2024.

[115] M. Domin, B. Hordacre, P. Hok, L. A. Boyd, A. B. Conforto, J. W. Andrushko, M. R. Borich, R. C. Craddock, M. R. Donnelly, A. N. Dula, S. J. Warach, S. A. Kautz, B. P. Lo, C. Schranz, N. J. Seo, S. Srivastava, K. A. Wong, A. Zavaliangos-Petropulu, P. M. Thompson, S.-L. Liew, and M. Lotze, "White Matter Integrity and Chronic Poststroke Upper Limb Function: An ENIGMA Stroke Recovery Analysis," *Stroke*, p. STROKEAHA.123.043713, July 2023.

[116] D. B. Archer, C. Patten, and S. A. Coombes, "Free-water and free-water corrected fractional anisotropy in primary and premotor corticospinal tracts in chronic stroke: Corticospinal Tract Microstructure in Chronic Stroke," *Human Brain Mapping*, vol. 38, pp. 4546–4562, Sept. 2017.

[117] O. G. Filatova, L. J. Van Vliet, A. C. Schouten, G. Kwakkel, F. C. T. Van Der Helm, and F. M. Vos, "Comparison of Multi-Tensor Diffusion Models' Performance for White Matter Integrity Estimation in Chronic Stroke," *Frontiers in Neuroscience*, vol. 12, p. 247, Apr. 2018.

[118] I. Boscolo Galazzo, L. Brusini, S. Obertino, M. Zucchelli, C. Granziera, and G. Menegaz, "On the Viability of Diffusion MRI-Based Microstructural Biomarkers in Ischemic Stroke," *Frontiers in Neuroscience*, vol. 12, p. 92, Feb. 2018.

[119] A. Auriat, M. Borich, N. Snow, K. Wadden, and L. Boyd, "Comparing a diffusion tensor and non-tensor approach to white matter fiber tractography in chronic stroke," *NeuroImage: Clinical*, vol. 7, pp. 771–781, 2015.

[120] Y. Bleyenheuft and A. M. Gordon, "Hand-Arm Bimanual Intensive Therapy Including Lower Extremities (HABIT-ILE) for Children with Cerebral Palsy," *Physical & Occupational Therapy In Pediatrics*, vol. 34, pp. 390–403, Nov. 2014.

[121] A. Carton De Tournai, E. Herman, E. Gathy, D. Ebner-Karestinos, R. Araneda, L. Dricot, B. Macq, Y. Vandermeeren, and Y. Bleyenheuft,

"Baby HABIT-ILE intervention: study protocol of a randomised controlled trial in infants aged 6–18 months with unilateral cerebral palsy," *BMJ Open*, vol. 14, p. e078383, Feb. 2024.

[122] D. Ebner-Karestinos, E. Gathy, A. Carton De Tournai, E. Herman, R. Araneda, L. Dricot, B. Macq, Y. Vandermeeren, and Y. Bleyenheuft, "Hand-Arm Bimanual Intensive Therapy Including Lower Extremities (HABIT-ILE) in adults with chronic stroke: protocol of a randomised controlled trial," *BMJ Open*, vol. 13, p. e070642, Apr. 2023.

[123] Q. Dessain, M. Simon, and N. Delinte, "Hyedryn/elikopy: v0.4.4," Apr. 2024.

[124] A. Hoopes, J. S. Mora, A. V. Dalca, B. Fischl, and M. Hoffmann, "SynthStrip: skull-stripping for any brain image," *NeuroImage*, vol. 260, p. 119474, Oct. 2022.

[125] S. Forkel, C. Bortolami, L. Dulyan, R. L. Barrett, and A. Beyh, "Dissecting white matter pathways: A neuroanatomical approach," preprint, PsyArXiv, Aug. 2023.

[126] J.-D. Tournier, R. Smith, D. Raffelt, R. Tabbara, T. Dhollander, M. Pietsch, D. Christiaens, B. Jeurissen, C.-H. Yeh, and A. Connelly, "MRtrix3: A fast, flexible and open software framework for medical image processing and visualisation," *NeuroImage*, vol. 202, p. 116137, Nov. 2019.

[127] R. H. Tijssen, J. F. Jansen, and W. H. Backes, "Assessing and minimizing the effects of noise and motion in clinical DTI at 3 T," *Human Brain Mapping*, vol. 30, pp. 2641–2655, Aug. 2009.

[128] G. L. Baum, D. R. Roalf, P. A. Cook, R. Ciric, A. F. Rosen, C. Xia, M. A. Elliott, K. Ruparel, R. Verma, B. Tunç, R. C. Gur, R. E. Gur, D. S. Bassett, and T. D. Satterthwaite, "The impact of in-scanner head motion on structural connectivity derived from diffusion MRI," *NeuroImage*, vol. 173, pp. 275–286, June 2018.

[129] P. J. Winklewski, A. Sabisz, P. Naumczyk, K. Jodzio, E. Szurowska, and A. Szarmach, "Understanding the Physiopathology Behind Axial and Radial Diffusivity Changes—What Do We Know?," *Frontiers in Neurology*, vol. 9, p. 92, Feb. 2018.

[130] National Institute on Alcohol Abuse and Alcoholism, "Understanding alcohol use disorder," *NIAAA*, 2023.

[131] American Psychiatric Association, *Diagnostic and Statistical Manual of Mental Disorders*. American Psychiatric Association, fifth edition ed., May 2013.

[132] S. Donato and L. Ray, "Neurobiology and the Treatment of Alcohol Use Disorder: A Review of the Evidence Base," *Substance Abuse and Rehabilitation*, vol. Volume 14, pp. 157–166, Nov. 2023.

[133] L. Orio, F. Alen, F. J. Pavón, A. Serrano, and B. García-Bueno, "Oleoylethanolamide, Neuroinflammation, and Alcohol Abuse," *Frontiers in Molecular Neuroscience*, vol. 11, p. 490, Jan. 2019.

[134] S. M. De La Monte and J. J. Kril, "Human alcohol-related neuropathology," *Acta Neuropathologica*, vol. 127, pp. 71–90, Jan. 2014.

[135] A. Pfefferbaum, M. J. Rosenbloom, W. Chu, S. A. Sassoon, T. Rohlfing, K. M. Pohl, and E. V. Sullivan, "White matter microstructural recovery with abstinence and decline with relapse in alcohol dependence interacts with normal ageing: a controlled longitudinal DTI study," *The Lancet Psychiatry*, vol. 1, no. 3, pp. 202–212, 2014.

[136] P. Xiao, Z. Dai, J. Zhong, Y. Zhu, H. Shi, and P. Pan, "Regional gray matter deficits in alcohol dependence: A meta-analysis of voxel-based morphometry studies," *Drug and Alcohol Dependence*, vol. 153, pp. 22–28, Aug. 2015.

[137] C. Spindler, S. Trautmann, N. Alexander, S. Bröning, S. Bartscher, M. Stuppe, and M. Muehlhan, "Meta-analysis of grey matter changes and their behavioral characterization in patients with alcohol use disorder," *Scientific Reports*, vol. 11, p. 5238, Mar. 2021.

[138] "Mega-Analysis of Gray Matter Volume in Substance Dependence: General and Substance-Specific Regional Effects," *American Journal of Psychiatry*, vol. 176, pp. 119–128, Feb. 2019.

[139] D. Nutt, A. Hayes, L. Fonville, R. Zafar, E. O. Palmer, L. Paterson, and A. Lingford-Hughes, "Alcohol and the Brain," *Nutrients*, vol. 13, p. 3938, Nov. 2021.

[140] W. H. Hampton, I. M. Hanik, and I. R. Olson, "Substance abuse and white matter: Findings, limitations, and future of diffusion tensor imaging research," *Drug and Alcohol Dependence*, vol. 197, pp. 288–298, Apr. 2019.

[141] Q. Zhao, E. V. Sullivan, N. Honnorat, E. Adeli, S. Podhajsky, M. D. De Bellis, J. Voyvodic, K. B. Nooner, F. C. Baker, I. M. Colrain, S. F.

Tapert, S. A. Brown, W. K. Thompson, B. J. Nagel, D. B. Clark, A. Pfefferbaum, and K. M. Pohl, "Association of Heavy Drinking With Deviant Fiber Tract Development in Frontal Brain Systems in Adolescents," *JAMA Psychiatry*, vol. 78, p. 407, Apr. 2021.

[142] X. Yang, F. Tian, H. Zhang, J. Zeng, T. Chen, S. Wang, Z. Jia, and Q. Gong, "Cortical and subcortical gray matter shrinkage in alcohol-use disorders: a voxel-based meta-analysis," *Neuroscience & Biobehavioral Reviews*, vol. 66, pp. 92–103, July 2016.

[143] L. Li, H. Yu, Y. Liu, Y.-j. Meng, X.-j. Li, C. Zhang, S. Liang, M.-l. Li, W. Guo, QiangWang, W. Deng, X. Ma, J. Coid, and T. Li, "Lower regional grey matter in alcohol use disorders: evidence from a voxel-based meta-analysis," *BMC Psychiatry*, vol. 21, p. 247, Dec. 2021.

[144] C. Spindler, L. Mallien, S. Trautmann, N. Alexander, and M. Muehlhan, "A coordinate-based meta-analysis of white matter alterations in patients with alcohol use disorder," *Translational Psychiatry*, vol. 12, p. 40, Jan. 2022.

[145] C. Crespi, C. Galandra, N. Canessa, M. Manera, P. Poggi, and G. Basso, "Microstructural damage of white-matter tracts connecting large-scale networks is related to impaired executive profile in alcohol use disorder," *NeuroImage: Clinical*, vol. 25, p. 102141, 2020.

[146] P.-H. Yeh, K. Simpson, T. C. Durazzo, S. Gazdzinski, and D. J. Meyerhoff, "Tract-based spatial statistics (TBSS) of diffusion tensor imaging data in alcohol dependence: Abnormalities of the motivational neurocircuitry," *Psychiatry Research: Neuroimaging*, vol. 173, pp. 22–30, July 2009.

[147] E. V. Sullivan and A. Pfefferbaum, "Alcohol use disorder: Neuroimaging evidence for accelerated aging of brain morphology and hypothesized contribution to age-related dementia," *Alcohol*, vol. 107, pp. 44–55, Mar. 2023.

[148] L. Pérez-Cervera, S. De Santis, E. Marcos, Z. Ghorbanzad-Ghaziany, A. Trouvé-Carpena, M. K. Selim, U. Pérez-Ramírez, S. Pfarr, P. Bach, P. Halli, F. Kiefer, D. Moratal, P. Kirsch, W. H. Sommer, and S. Canals, "Alcohol-induced damage to the fimbria/fornix reduces hippocampal-prefrontal cortex connection during early abstinence," *Acta Neuropathologica Communications*, vol. 11, p. 101, June 2023.

[149] Y. Zou, D. E. Murray, T. C. Durazzo, T. P. Schmidt, T. A. Murray, and D. J. Meyerhoff, "White matter microstructural correlates of relapse in alcohol dependence," *Psychiatry Research: Neuroimaging*, vol. 281, pp. 92–100, Nov. 2018.

[150] B. Kim, W.-S. Shin, M.-K. Kim, and S.-H. Lee, "White matter microstructural changes are associated with alcohol use in patients with panic disorder," *Journal of Affective Disorders*, vol. 199, pp. 65–72, July 2016.

[151] S. M. Smith, M. Jenkinson, H. Johansen-Berg, D. Rueckert, T. E. Nichols, C. E. Mackay, K. E. Watkins, O. Ciccarelli, M. Z. Cader, P. M. Matthews, and T. E. J. Behrens, "Tract-based spatial statistics: voxelwise analysis of multi-subject diffusion data," *NeuroImage*, vol. 31, pp. 1487–1505, July 2006. 10.1016/j.neuroimage.2006.02.024.

[152] J. Ashburner and K. J. Friston, "Voxel-Based Morphometry—The Methods," *NeuroImage*, vol. 11, pp. 805–821, June 2000.

[153] B. Avants, C. Epstein, M. Grossman, and J. Gee, "Symmetric diffeomorphic image registration with cross-correlation: Evaluating automated labeling of elderly and neurodegenerative brain," *Medical Image Analysis*, vol. 12, pp. 26–41, Feb. 2008.

[154] S. L. Benear, C. T. Ngo, and I. R. Olson, "Dissecting the Fornix in Basic Memory Processes and Neuropsychiatric Disease: A Review," *Brain Connectivity*, vol. 10, pp. 331–354, Sept. 2020.

[155] E. J. Bubb, C. Metzler-Baddeley, and J. P. Aggleton, "The cingulum bundle: Anatomy, function, and dysfunction," *Neuroscience & Biobehavioral Reviews*, vol. 92, pp. 104–127, Sept. 2018.

[156] S. Hofer and J. Frahm, "Topography of the human corpus callosum revisited—Comprehensive fiber tractography using diffusion tensor magnetic resonance imaging," *NeuroImage*, vol. 32, pp. 989–994, Sept. 2006.

[157] A. K. Conner, R. G. Briggs, G. Sali, M. Rahimi, C. M. Baker, J. D. Burks, C. A. Glenn, J. D. Battiste, and M. E. Sughrue, "A Connectomic Atlas of the Human Cerebrum—Chapter 13: Tractographic Description of the Inferior Fronto-Occipital Fasciculus," *Operative Neurosurgery*, vol. 15, pp. S436–S443, Dec. 2018.

[158] A. Kamali, A. E. Flanders, J. Brody, J. V. Hunter, and K. M. Hasan, "Tracing superior longitudinal fasciculus connectivity in the human brain using high resolution diffusion tensor tractography," *Brain Structure and Function*, vol. 219, pp. 269–281, Jan. 2014.

[159] G. Sammer, E. Neumann, C. Blecker, and B. Pedraz-Petrozzi, "Fractional anisotropy and peripheral cytokine concentrations in outpatients with depressive episode: a diffusion tensor imaging observational study," *Scientific Reports*, vol. 12, p. 17450, Oct. 2022.

[160] D. K. Jones, T. R. Knösche, and R. Turner, "White matter integrity, fiber count, and other fallacies: The do's and don'ts of diffusion MRI," *NeuroImage*, vol. 73, pp. 239–254, June 2013.

[161] M. Porcu, L. Cocco, R. Cau, J. S. Suri, L. Mannelli, M. Manchia, J. Puig, Y. Qi, and L. Saba, "Correlation of Cognitive Reappraisal and the Microstructural Properties of the Forceps Minor: A Deductive Exploratory Diffusion Tensor Imaging Study," *Brain Topography*, vol. 37, pp. 63–74, Jan. 2024.

[162] F. A. Mansouri, E. Koechlin, M. G. P. Rosa, and M. J. Buckley, "Managing competing goals — a key role for the frontopolar cortex," *Nature Reviews Neuroscience*, vol. 18, pp. 645–657, Nov. 2017.

[163] S. De Santis, P. Bach, L. Pérez-Cervera, A. Cosa-Linan, G. Weil, S. Vollstädt-Klein, D. Hermann, F. Kiefer, P. Kirsch, R. Ciccocioppo, W. H. Sommer, and S. Canals, "Microstructural White Matter Alterations in Men With Alcohol Use Disorder and Rats With Excessive Alcohol Consumption During Early Abstinence," *JAMA Psychiatry*, vol. 76, p. 749, July 2019.

[164] Y. Wu, D. Sun, Y. Wang, Y. Wang, and S. Ou, "Segmentation of the Cingulum Bundle in the Human Brain: A New Perspective Based on DSI Tractography and Fiber Dissection Study," *Frontiers in Neuroanatomy*, vol. 10, Sept. 2016.

[165] J. Wasserthal, P. Neher, and K. H. Maier-Hein, "TractSeg - Fast and accurate white matter tract segmentation," *NeuroImage*, vol. 183, pp. 239–253, Dec. 2018.

[166] R. Vink, A. Vilanova, and M. Chamberland, "Multi-dimensional Parameter Space Exploration for Streamline-specific Tractography," Aug. 2024. arXiv:2408.05056 [cs, eess].

[167] K. G. Schilling, J. Blaber, C. Hansen, L. Cai, B. Rogers, A. W. Anderson, S. Smith, P. Kanakaraj, T. Rex, S. M. Resnick, A. T. Shafer, L. E. Cutting, N. Woodward, D. Zald, and B. A. Landman, "Distortion correction of diffusion weighted MRI without reverse phase-encoding scans or fieldmaps," *PLOS ONE*, vol. 15, p. e0236418, July 2020.

[168] N. J. Tustison, P. A. Cook, A. J. Holbrook, H. J. Johnson, J. Muschelli, G. A. Devenyi, J. T. Duda, S. R. Das, N. C. Cullen, D. L. Gillen, M. A. Yassa, J. R. Stone, J. C. Gee, and B. B. Avants, "The ANTsX ecosystem for quantitative biological and medical imaging," *Scientific Reports*, vol. 11, p. 9068, Apr. 2021.

[169] W. Y. Aung, S. Mar, and T. L. Benzinger, "Diffusion tensor MRI as a biomarker in axonal and myelin damage," *Imaging in Medicine*, vol. 5, pp. 427–440, Oct. 2013.

[170] C. L. Tardif, C. J. Gauthier, C. J. Steele, P.-L. Bazin, A. Schäfer, A. Schaefer, R. Turner, and A. Villringer, "Advanced MRI techniques to improve our understanding of experience-induced neuroplasticity," *NeuroImage*, vol. 131, pp. 55–72, May 2016.

[171] B. L. Geeraert, R. M. Lebel, A. C. Mah, S. C. Deoni, D. C. Alsop, G. Varma, and C. Lebel, "A comparison of inhomogeneous magnetization transfer, myelin volume fraction, and diffusion tensor imaging measures in healthy children," *NeuroImage*, vol. 182, pp. 343–350, Nov. 2018.

[172] J. S. Campbell, I. R. Leppert, S. Narayanan, M. Boudreau, T. Duval, J. Cohen-Adad, G. B. Pike, and N. Stikov, "Promise and pitfalls of g-ratio estimation with MRI," *NeuroImage*, vol. 182, pp. 80–96, Nov. 2018.

[173] M. Li, K. G. Schilling, Z. Ding, and J. C. Gore, "Assessing White Matter Engagement in Brain Networks through Functional and Structural Connectivity Mapping," preprint, Neuroscience, Jan. 2024.

[174] Y. Wang, H. Wang, S. Hu, B. A. Nguchu, D. Zhang, S. Chen, Y. Ji, B. Qiu, and X. Wang, "Sub-bundle based analysis reveals the role of human optic radiation in visual working memory," *Human Brain Mapping*, vol. 45, p. e26800, Aug. 2024.

[175] B. Q. Chandio, J. E. Villalon-Reina, T. M. Nir, S. I. Thomopoulos, Y. Feng, S. Benavidez, N. Jahanshad, J. Harezlak, E. Garyfallidis, P. M. Thompson, and the Alzheimer's Disease Neuroimaging Initiative, "Amyloid, Tau, and APOE in Alzheimer's Disease: Impact on White Matter Tracts," Aug. 2024.

Appendix A

Complimentary background information

A.1 Bloch equations

In a state of equilibrium between the nuclear moments and the surrounding atoms, the net equilibrium magnetization M_0 is defined as

$$\begin{aligned} M_0 &= \chi B_0 \\ M_0 &= \frac{N\gamma^2 h^2 I_z(I_z+1)}{3kT} B_0 \end{aligned}$$

where N is the spin density, h is Planck's constant, λ is the gyromagnetic ratio, B_0 is the magnetic field, I_z is the spin number, k is Boltzmann's constant, and T is the temperature. For hydrogen atoms, $I_z = 1/2$, the equation becomes

$$M_0 = \frac{N\gamma^2 h^2}{4kT} B_0$$

Similarly to Rabi, Bloch investigated the behavior of nuclei contained in a macroscopic sample of matter and acted upon by two external fields: a strong constant field and at right angles to it, a comparatively weak radio-frequency field [2]. The Bloch equation has two main components: one for the precession and the other for the relaxation after a RF pulse. Bloch introduces the two relaxation time constants: the spin-lattice relaxation $T1$ and the spin-spin relaxation $T2$. In a simplified form, the equation reads as

$$\frac{d\vec{M}(t)}{dt} = \gamma \vec{M}(t) \times B_0 + \begin{pmatrix} -1/T2 & 0 & 0 \\ 0 & -1/T2 & 0 \\ 0 & 0 & -1/T1 \end{pmatrix} \vec{M}(t) + \begin{pmatrix} 0 \\ 0 \\ M_0/T1 \end{pmatrix}$$

In a rotating frame (to negate the effects of the precession) the part of the equation describing the relaxation after and RF pulse has the following solutions

$$\vec{M}(t) = \begin{pmatrix} e^{-1/T2} & 0 & 0 \\ 0 & e^{-1/T2} & 0 \\ 0 & 0 & e^{-1/T1} \end{pmatrix} \vec{M}(0) + \begin{pmatrix} 0 \\ 0 \\ M_0(1 - e^{-1/T1}) \end{pmatrix}$$

A.2 RF pulses & flip angles

As mentioned in the previous section (Appendix A.1), radio frequency (RF) pulses cause spinning protons to be deflected from their equilibrium state. Immediately after an RF pulse, protons begin to return to equilibrium by two separate processes: T1 and T2 relaxation. The flip angle is equal to the integral of the RF pulse shape b_1,

$$\theta = \gamma \int_0^t b_1(\tau) d\tau,$$

which, for an RF pulse of constant amplitude B_1 and duration t, can be approximated as

$$\theta = \gamma \cdot B_1 \cdot t,$$

where γ is the gyromagnetic ratio.
To go from an RF pulse of 90° to 180°, either the duration of the amplitude has to be doubled.

A.3 The link between diffusivity and b-value

For a specific diffusivity D, the b-value with the highest discerning power is the one with the highest slope, since a small variation in diffusivity will greatly affect the signal received. To find the corresponding b-value, Equation (3) can be derived with respect to D

$$S/S_0' = -b\, e^{-bD}. \tag{A.1}$$

The minimum of this equation will correspond to the value with the greatest negative slope. We derive Equation (A.1) with respect to b

$$\begin{aligned} 0 &= -e^{-bD} + bDe^{-bD} \\ b &= 1/D. \end{aligned}$$

When inserted back into Equation (3), we find that the b-value with the highest slope (Figure A.1B) is the one for which the signal ratio is closest to

$$S/S_0 = e^{-1},$$

which is verified when the number of b-values tends to infinity (see Figure A.1A) .

Another interesting aspect is the point of highest curvature, which is obtained with the maximum of the second derivative of Equation (3). By deriving Equation (A.1) with respect to D

$$S/S_0'' = b^2 e^{-bD},$$

and looking for its maximum among each b-value by deriving with respect to b

$$\begin{aligned} 0 &= 2be^{-bD} - b^2 De^{-bD} \\ b &= 2/D, \end{aligned}$$

we get the point of highest curvature (Figure A.1D) . Across all b-values, the one with the maximal curvature (Figure A.1C) is the one for which the signal ratio is closest to

$$S/S_0 = e^{-2}.$$

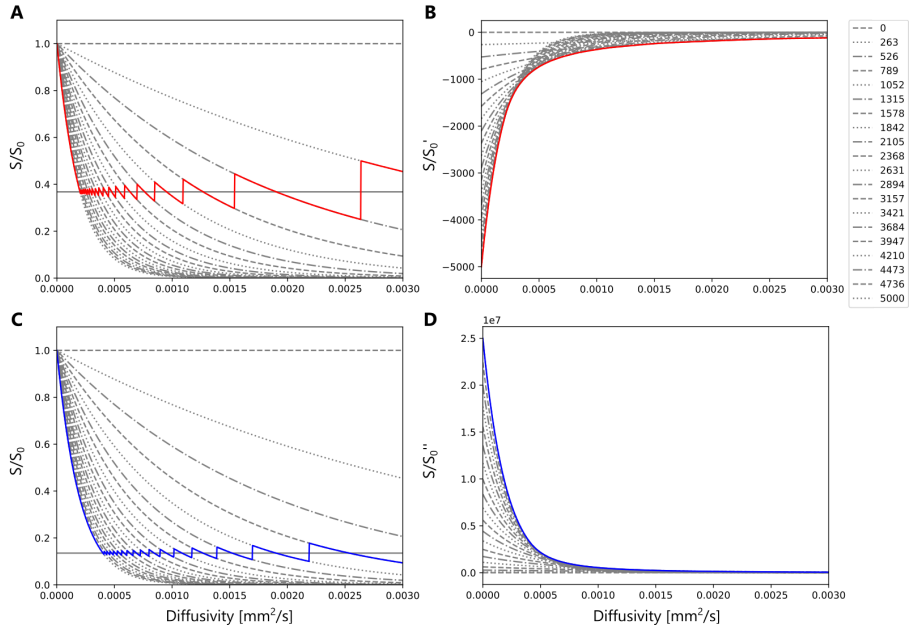

Figure A.1: Evolution of the diffusion signal ratio depending on the diffusivity (**A,C**) and its first (**B**) and second (**D**) derivatives. The b-value presenting the highest slope (red) and curvature (blue) are also displayed.

A.4 Diffusion tensors

The diffusion tensor is symmetric, a minimum of 6 orientations are thus required to estimate its coefficients

$$\mathbf{D} = \begin{pmatrix} D_{xx} & D_{xy} & D_{xz} \\ D_{yx} & D_{yy} & D_{yz} \\ D_{zx} & D_{zy} & D_{zz} \end{pmatrix}.$$

The elements of $\mathbf{D}$ on its diagonal represent the diffusion coefficients along the three principal directions. Once the diffusion tensor is obtained, it becomes possible to use the eigenvalues of the tensor to represent interesting properties of cerebral tissues. The eigenvalues are defined by the Λ matrix

$$\mathbf{D} = \mathbf{E} \cdot \Lambda \cdot \mathbf{E}^{-1},$$

with E the eigenvectors matrix and Λ the eigenvalues matrix

$$\mathbf{E} = \begin{pmatrix} e_{1x} & e_{2x} & e_{3x} \\ e_{1y} & e_{2y} & e_{3y} \\ e_{1z} & e_{2z} & e_{3z} \end{pmatrix}, \Lambda = \begin{pmatrix} \lambda_1 & 0 & 0 \\ 0 & \lambda_2 & 0 \\ 0 & 0 & \lambda_3 \end{pmatrix}.$$

A.4.1 Common metrics

The mean diffusivity (MD) can be computed from the mean of the eigenvalues of the diffusion tensor

$$MD = \frac{\lambda_1 + \lambda_2 + \lambda_3}{3} = \frac{D_{xx} + D_{yy} + D_{zz}}{3}.$$

The diffusivity can also be separated into an axial component (AD) and a radial component (RD)

$$AD = \lambda_1,$$

$$RD = \frac{\lambda_2 + \lambda_3}{2}.$$

The fractional anisotropy (FA) is computed with the formula

$$FA = \sqrt{\frac{3}{2}} \frac{\sqrt{(\lambda_1 - MD)^2 + (\lambda_2 - MD)^2 + (\lambda_3 - MD)^2}}{\sqrt{\lambda_1^2 + \lambda_2^2 + \lambda_3^2}}.$$

Or, equivalently

$$FA = \sqrt{\frac{1}{2}} \frac{(\lambda_1 - \lambda_2)^2 + (\lambda_2 - \lambda_3)^2 + (\lambda_3 - \lambda_1)^2}{\lambda_1^2 + \lambda_2^2 + \lambda_3^2}.$$

A.4.2 Main direction to tensor

For visualization purposes, it is possible to obtain a diffusion tensor D from a direction vector $\mathbf{d}$. Considering d_x, d_y and d_z to be the change of coordinates in the voxel space between to tractography steps, the vector

$$\mathbf{d} = \begin{pmatrix} d_x \\ d_y \\ d_z \end{pmatrix},$$

contains information about the main direction of propagation. By assuring that the dot product between $\mathbf{d}$ and another is 0, a second perpendicular

vector $\mathbf{d}_{\perp,1}$ can be obtained. The cross product between $\mathbf{v}$ and $\mathbf{d}_{\perp,1}$ gives the third vector $\mathbf{d}_{\perp,2}$, perpendicular to the other two. These three vectors can be considered to be the eigenvectors of the eigenvalues $(1, 0, 0)$. For example,

$$\mathbf{E} = \begin{pmatrix} d_x & -d_z - d_y & d_y d_x - d_x d_z \\ d_y & dx & -d_x^2 - (d_z + d_y) d_z \\ d_z & dx & d_x^2 + (d_y + d_z) d_y \end{pmatrix}.$$

A.5 Spherical harmonics

Spherical harmonics have two special properties: completeness and orthogonality. Orthogonality refers to the property of functions being independent of each other. Completeness implies that a linear combination converges to an exact result for a sufficient number of terms. Any function on the surface of a sphere can thus be approximated using spherical harmonics.

$$S(\theta, \phi) = \sum_{l=0} \sum_{m=-l}^{l} \hat{s}_l^m Y_l^m(\theta, \phi),$$

where s_l^m are the expansion coefficients.

In diffusion MRI, several hypotheses can be placed to simplify the number of SH used in the entire set.

- Only even degrees l are considered. Since the diffusion process is symmetric with respect to the origin, all odd order components must be zero. [22]
- The response functions are axially symmetric, and therefore constrained to the spherical harmonics of order m=0. [27]

A.6 Response function

The signal $S(\theta, \phi)$ measured from a voxel containing several fiber populations is given by the sum of the response functions $R(\theta)$ of each population, weighted by their respective volume fractions f, and rotated such that they are aligned along their respective orientations

$$S(\theta, \phi) = \sum_i f_i \hat{A}_i R(\theta),$$

with $\hat{A}$ representing the rotation operation aligning the response function to the fixel orientation. This equation can also be expressed as

$$S(\theta, \phi) = F(\theta, \phi) \otimes R(\theta),$$

with $F(\theta, \phi)$ being the fODF. Due to the properties of the SH (see Appendix A.5), the spherical convolution operation can be formulated as an ensemble of rotations of the convolution kernel on a function defined over a sphere. This form reduces the spherical convolution operation to a set of matrix multiplications.
In this example, the fODF will be defined as

$$F(\theta, \phi) = f_1 \delta(90^\circ, 0^\circ) + f_2 \delta(30^\circ, 0^\circ),$$

where θ is the polar angle, ϕ the azimuthal angle, f_k the volume fractions and δ a Dirac delta function on the sphere.
The response function used in this example is the response of a tensor model, with $\lambda_1 > \lambda_2 = \lambda_3$, as in [23]. The diffusivity along a specific direction (θ, ϕ) is

$$\begin{aligned} D(\theta, \phi) &= \begin{pmatrix} \sin\theta\cos\phi \\ \sin\theta\sin\phi \\ \cos\theta \end{pmatrix}^T \begin{pmatrix} \lambda_3 & 0 & 0 \\ 0 & \lambda_2 & 0 \\ 0 & 0 & \lambda_1 \end{pmatrix} \begin{pmatrix} \sin\theta\cos\phi \\ \sin\theta\sin\phi \\ \cos\theta \end{pmatrix} \\ &= \lambda_2 \sin^2\theta + \lambda_1 \cos^2\theta \end{aligned}$$

This equation was simplified by aligning the main diffusion direction with the z axis, which renders D only dependent of θ. The profiles of a single response function and a mix of two response functions are presented in Fig. A.2 It should be noted that although the diffusion tensor model can be used to estimate the response function, one advantage of CSD is that it does not rely on any model of diffusion.

Two observations can be made from the graphs shown in Fig. A.2: i) the signal response decreases with increasing b-values, and ii) higher b-values exhibit greater discerning power between different fixel orientations. At low b-values fixel with similar orientations are merged into a single lobe.

For more information about the response function, see [22, 23].

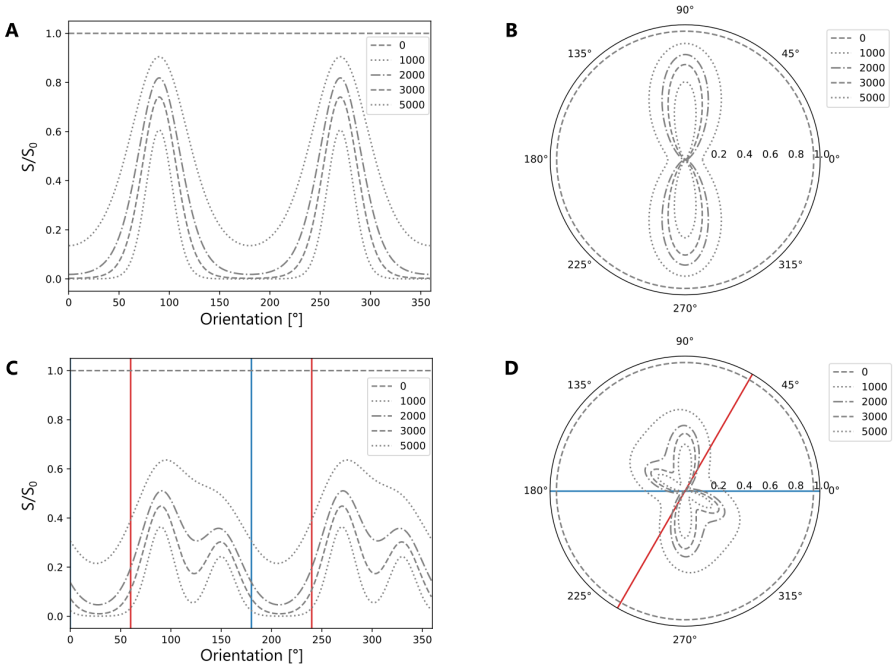

Figure A.2: Graph of the response function across different b-values for a single fixel of orientation 90° and f=1 in **A** Cartesian and **B** polar coordinates. In a similar fashion, the **C** and **D** plots represent the same response function with the addition of a second fixel of orientation 30° (red) and with both f at 0.6 and 0.4 for the first and second fiber population, respectively.

Appendix B

Interpretation at the segment level

This section provides another perspective on the microstructure maps (Eq. (3.10)) and the mean tract microstructural metric (Eq. (3.11)), interpreted at the level of individual streamline segments.

Equation (3.10) can be rewritten as follows

$$
\begin{aligned}
M_v^{\mathcal{T}} &= \frac{\sum_{k=1}^{K} w_{vk}^{\mathcal{T}} M_{vk}^{\mu}}{\sum_{k=1}^{K} w_{vk}^{\mathcal{T}}} \\
&= \frac{\sum_{k=1}^{K} \sum_s \alpha_{vsk} l_{vs} M_{vk}^{\mu}}{\sum_{k=1}^{K} \sum_s \alpha_{vsk} l_{vs}} \quad (*) \\
&= \frac{\sum_s l_{vs} \sum_{k=1}^{K} \alpha_{vsk} M_{vk}^{\mu}}{\sum_s l_{vs} \sum_{k=1}^{K} \alpha_{vsk}} \quad (**) \\
&= \frac{\sum_s l_{vs} \sum_{k=1}^{K} \alpha_{vsk} M_{vk}^{\mu}}{\sum_s l_{vs}} \quad (***) \\
&= \frac{\sum_s l_{vs} M_{vs}}{\sum_s l_{vs}}, \quad (****)
\end{aligned}
$$

where $(*)$ uses Eq. (3.8), $(**)$ switches the order of summation, $(***)$ uses Eq. (3.1) and $(****)$ uses Eq. (3.7). The last equality states that the tract-specific map in a voxel v results from the contributions of all streamline segments in that voxel. Each segment contributes its segment-specific microstructural metric defined in Eq. (3.7), weighted by its intra-voxel length l_{vs}. The quantity is normalized by the total segment length in that voxel.

Similarly, Eq. (3.11) using Eq. (3.12) can be rewritten as

$$\begin{aligned}
\bar{M}^{\mathcal{T}} &= \frac{\sum_v \gamma_v^{\mathcal{T}} M_v^{\mathcal{T}}}{\sum_v \gamma_v^{\mathcal{T}}} \\
&= \frac{\sum_v \gamma_v^{\mathcal{T}} \frac{\sum_s l_{vs} M_{vs}}{\sum_s l_{vs}}}{\sum_v \gamma_v^{\mathcal{T}}} \quad (*) \\
&= \frac{\sum_v \sum_s l_{vs} \frac{\sum_s l_{vs} M_{vs}}{\sum_s l_{vs}}}{\sum_v \sum_s l_{vs}} \quad (**) \\
&= \frac{\sum_v \sum_s l_{vs} M_{vs}}{\sum_v \sum_s l_{vs}},
\end{aligned}$$

where $(*)$ uses Eq. (3.14) and $(**)$ uses Eq. (3.9) and Eq. (3.12). The interpretation is similar to the tract-specific microstructure map $M_v^{\mathcal{T}}$ above, except for the contributions, which are from all segments s over all the voxels containing streamlines of tract $\mathcal{T}$.

Appendix C

Additional graphs

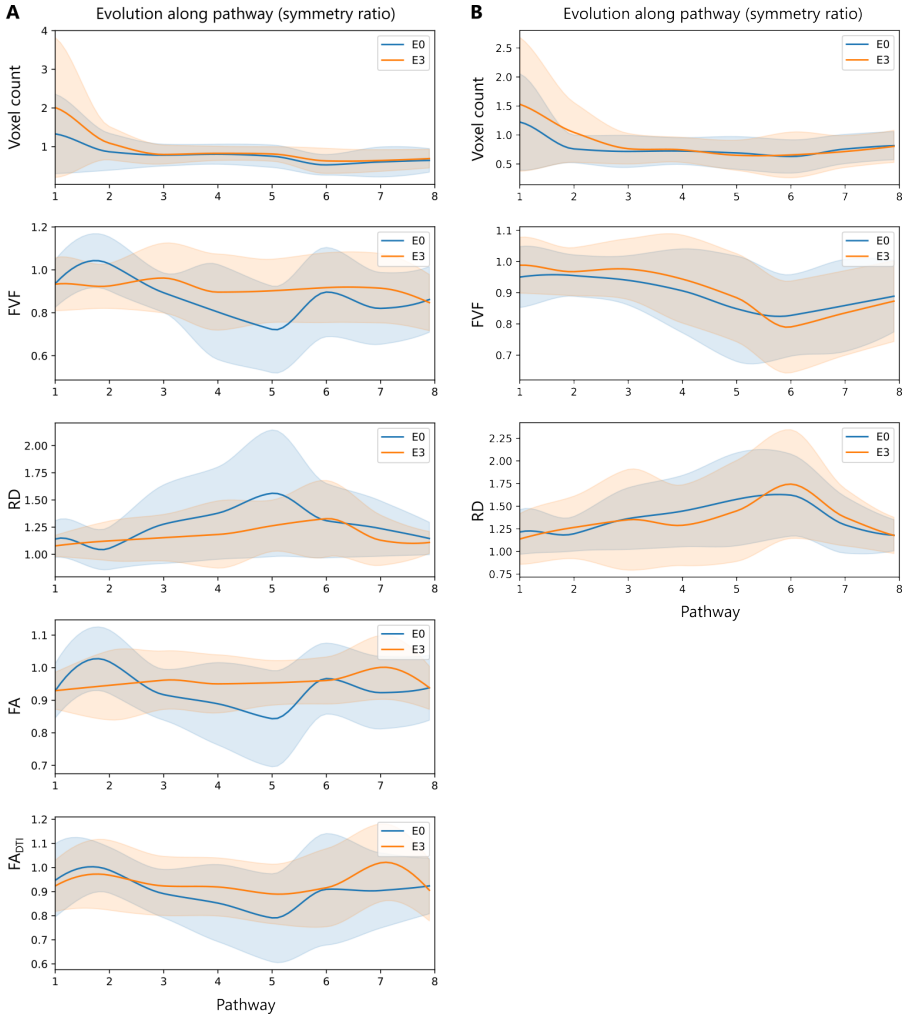

Figure C.1: Evolution of the symmetry ratio for different metrics (voxel_count: tract volume, FVF: fiber volume fraction, RD: radial diffusivity, FA: fractional anisotropy) along the pathway of the CST in **A** CP children and **B** adults with stroke before (E0, blue) and after (E3, orange) neurorehabilitation.

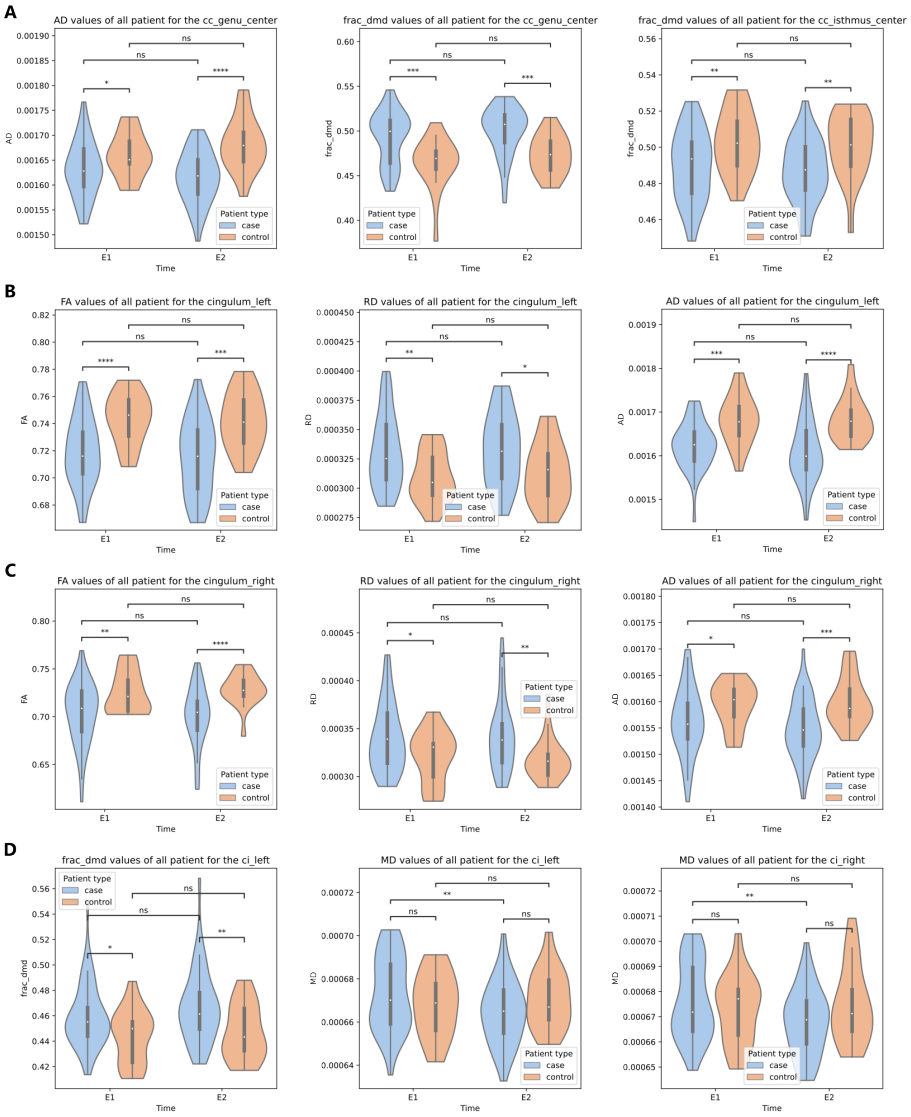

Figure C.2: Additional violin plots of the distribution of the microstructural metrics of the **A** corpus callosum, **B** left cingulum, **C** right cingulum and **D** left internal capsule for the AUD (blue) and control (orange) population, before (E1) and after (E2) an 18-day period.

Thank you for reading